PREDICTIVE RESERVOIR MODELING FOR CO_2 SEQUESTRATION IN KIZILDERE RESERVOIR USING MULTIPLE INTER-WELL TRACER TESTS

A THESIS SUBMITTED TO
THE GRADUATE SCHOOL OF NATURAL AND APPLIED SCIENCES
OF
MIDDLE EAST TECHNICAL UNIVERSITY

BY

DOĞUHAN BARLAS SEVİNDİK

IN PARTIAL FULFILLMENT OF THE REQUIREMENTS
FOR
THE DEGREE OF MASTER OF SCIENCE
IN
PETROLEUM AND NATURAL GAS ENGINEERING

SEPTEMBER 2023

Approval of the thesis:

PREDICTIVE RESERVOIR MODELING FOR CO_2 SEQUESTRATION IN KIZILDERE RESERVOIR USING MULTIPLE INTER-WELL TRACER TESTS

submitted by **DOĞUHAN BARLAS SEVİNDİK** in partial fulfillment of the requirements for the degree of **Master of Science** i**n Petroleum and Natural Gas Engineering, Middle East Technical University** by,

Prof. Dr. Halil Kalıpçılar
Dean, Graduate School of **Natural and Applied Sciences** _____

Assist. Prof. Dr. İsmail Durgut
Head of the Department, **Petroleum and Natural Gas Engineering, METU** _____

Prof. Dr. Serhat Akın
Supervisor, **Petroleum and Natural Gas Engineering, METU** _____

Assist. Prof. Dr. Selçuk Erol
Co-Supervisor, **Energy Systems Engineering, İzmir Institute of Technology** _____

Examining Committee Members:

Assist. Prof. Dr. İsmail Durgut
Petroleum and Natural Gas Engineering, METU _____

Prof. Dr. Serhat Akın
Petroleum and Natural Gas Engineering, METU _____

Assist. Prof. Dr. Yıldıray Palabıyık
Petroleum and Natural Gas Engineering, ITU _____

Date: 08.09.2023

I hereby declare that all information in this document has been obtained and presented in accordance with academic rules and ethical conduct. I also declare that, as required by these rules and conduct, I have fully cited and referenced all material and results that are not original to this work.

Name Last name : Doğuhan Barlas Sevindik

Signature :

ABSTRACT

PREDICTIVE RESERVOIR MODELING FOR CO_2 SEQUESTRATION IN KIZILDERE RESERVOIR USING MULTIPLE INTER-WELL TRACER TESTS

Sevindik, Doğuhan Barlas
Master of Science, Petroleum and Natural Gas Engineering
Supervisor : Prof. Dr. Serhat Akın
Co-Supervisor: Assist. Prof. Dr. Selçuk Erol

September 2023, 174 pages

Geothermal energy is generally considered a clean and sustainable energy source compared to fossil fuels. However, there exist geothermal fields in Turkey where a high amount of non-condensable gas (NCG) with 98% CO_2 composition is co-produced with reservoir fluids. Thus, it is crucial to mitigate the co-produced NCG by re-injecting the captured gas back into the reservoir. In that regard, numerical reservoir models are significant tools for understanding the subsurface flow process and predicting the possible outcomes of the re-injection in the long term. In this study, a localized numerical reservoir model is developed centered across the pilot brine-CO_2 injection well to characterize the flow paths of the Kızıldere geothermal reservoir to predict the impact of the injection. The natural state model of the field has been calibrated to obtain the initial conditions of the reservoir model with less than a 10 % error tolerance for the PT observations. To characterize the flow characteristics in the reservoir, chloride is assumed to be a conservative species for which the gradual enrichment of the chloride concentrations is matched across the observation wells. Furthermore, two slug tracer tests have been performed from the pilot injection well and from the northernmost injection well by using naphthalene-

sulphonates for which the calibration across the possible flow paths in the Kızıldere reservoir is achieved accordingly. Consequently, a high degree of quantitative and qualitative characterization of the flow paths in the Kızıldere geothermal reservoir has been achieved. Based on the calibrated model, the impact of CO_2-brine injection has been predicted under different injection scenarios which consist of varying injection rates and durations, and constant and varying pressure conditions. The results of the CO_2-brine injection showed that approximately 20% of the injected CO_2 reaches back into the production wells until 2030 ensuring a safe CO_2 sequestration in the Kızıldere geothermal reservoir. Furthermore, under certain conditions, it has been estimated that a total of 200 Mt of CO_2 can be stored in the Kızıldere reservoir by commencing all of the re-injection wells.

Keywords: Tracers, TOUGH2, CO_2 Sequestration, Geothermal, Kızıldere

ÖZ

KIZILDERE REZERVUARINDA KUYULAR ARASI ÇOKLU İZLEYİCİ TESTLERİ KULLANARAK CO_2 SEKESTRASYONU İÇİN TAHMİNSEL REZERVUAR MODELLEMESİ

Sevindik, Doğuhan Barlas
Yüksek Lisans, Petrol ve Doğal gaz Mühendisliği
Tez Yöneticisi: Prof. Dr. Serhat Akın
Ortak Tez Yöneticisi: Dr. Selçuk Erol

Eylül 2023, 174 sayfa

Jeotermal enerji genellikle fosil yakıtlara kıyasla temiz ve sürdürülebilir bir enerji kaynağı olarak kabul edilir. Ancak, Türkiye'de, rezervuar akışkanları ile birlikte %98 CO_2 bileşimine sahip büyük miktarda yoğuşmayan gaz (NCG) üretilen jeotermal sahalar bulunmaktadır. Bu nedenle, yakalanan gazın rezervuara yeniden enjekte edilerek üretilen NCG'nin azaltılması önemlidir. Bu bağlamda, sayısal rezervuar modelleri, yer altı akış sürecini anlamak ve enjeksiyonun uzun vadeli olası sonuçlarını tahmin etmek için önemli araçlardır. Bu çalışmada, Kızıldere jeotermal rezervuarının akış yollarını karakterize etmek ve enjeksiyonun etkisini tahmin etmek için TOUGH2 rezervuar simulatorü kullanılarak enjeksiyon kuyusu etrafında merkezlenmiş yerel bir sayısal rezervuar modeli geliştirilmiştir. Sahanın doğal durum modeli, rezervuar modelinin başlangıç koşullarını elde etmek için 10 % hata toleransıyla basınç ve sıcaklık gözlemlerini kullanarak kalibre edilmiştir. Rezervuardaki akış karakteristiklerini tanımlamak için klorür, konservatif bir tür olarak kabul edilmiştir ve klorür konsantrasyonlarının artışı gözlem kuyuları boyunca eşleştirilmiştir. Ayrıca, Kızıldere rezervuarında olası akış yolları boyunca kalibrasyon sağlamak için pilot enjeksiyon kuyusundan ve en kuzeydeki enjeksiyon

kuyusundan iki adet izleyici testi naftalen-sülfonatlar kullanarak gerçekleştirilmiştir. Sonuç olarak, Kızıldere jeotermal rezervuarının akış yollarının yüksek derecede karakterizasyonu sağlanmıştır. Kalibre edilen modele dayanarak, CO_2-tuzlu su enjeksiyonunun farklı enjeksiyon senaryoları altında (değişen enjeksiyon hızları, süreler, sabit ve farklı basınç koşullarında) etkisi tahmin edilmiştir. CO_2-tuzlu su enjeksiyonunun sonuçları, enjekte edilen CO_2'nin yaklaşık %20'sinin 2030 yılına kadar üretim kuyularına geri ulaştığını ve Kızıldere jeotermal rezervuarında güvenli bir CO_2 sekestrasyonu sağlandığını göstermiştir. Ayrıca, belirli koşullar altında tüm enjeksiyon kuyularının devreye alınmasıyla, Kızıldere rezervuarında toplam 200 Mt CO_2 depolanabileceği tahmin edilmektedir.

Anahtar Kelimeler: İzleyiciler, TOUGH2, CO_2 Sekestrasyonu, Jeotermal, Kızıldere

To my beloved mother and sister

ACKNOWLEDGMENTS

First and foremost, I extend my deepest gratitude to my supervisor, Prof. Dr. Serhat Akın, for his continuous support and invaluable guidance throughout the completion of this dissertation. Without his empathy, patience, and encouragement, this study could not have been completed.

I am deeply indebted to my co-supervisor, Asst. Prof. Dr. Selçuk Erol, for his unwavering support and guidance throughout my graduate studies. His patience, even during the most challenging times, has been instrumental in pushing my boundaries and improving my knowledge.

I am also grateful to Dr. Taylan Akın for his contributions to this study. His insightful guidance and constant encouragement to think outside of the box have helped shape the creative ideas behind this research.

My sincere thanks go to my dear friends, Aykut Bakan, Deniz Yılmaz, and Emirhan İnanç, for their unrequited support during my studies. Their unwavering motivation has been a constant source of strength, helping me navigate the difficulties I faced. I am equally grateful to my friend and colleague, Ali Berkay Tokel, for supporting me throughout this journey. I would like to express my heartfelt gratitude to my math teacher, Fuat Kürklü, who instilled in me a love for mathematics and science.

Finally, my greatest thanks go to my beloved family, whose support, sacrifices, and unconditional love made it possible for me to complete this study.

This research has been funded by the European Union's Horizon 2020 research and innovation program under Grant Agreement No. 818169-GECO. Additionally, I extend my thanks to the Zorlu Energy staff for providing the necessary data used in this study.

TABLE OF CONTENTS

LIST OF TABLES

TABLES

LIST OF FIGURES

FIGURES

NOMENCLATURE

C_T produced concentration from a well

C_i produced concentration from a grid block intersected by a production well

C_t transfer function (multi-fracture model)

D_l longitidunal dispersion coefficient

D_{tr} Taylor dispersion

$D_{x,y,z}$ hydrodynamic dispersion coefficient

F_β mass flux for the phase β

M_{CO_2} total amount of CO_2 that can be stored within the reservoir

Pe Peclet number

S_β saturation of the fluid phase β

X_β^κ mass fraction of component κ present in phase β

$k_{r\beta}$ relative permeability of the phase β

$\bar{q}$, average injection mass flow rate and injection duration

q_T mass flow rate of a production well

q_i mass flow rate from a grid block intersected by a production well

q_n^κ sink/source term for the n^{th} volume element and the mass component κ

t_b response start time

t_i injection duration

t_m mean arrival time

$u_{x,y,z}$ Darcy velocities

u_β internal energy of fluid phase β

$\hat{y}$ predicted value.

μ_β viscosity of the phase β

ρ_β density of phase β

ρ_β density of the phase β respectively

$C_{background}$ average background concentration of DIC/DS before the first arrival of the injected gas

$C_{initial}$ average initial concentration value

$C_{measured}$ sampled concentration of CO_2/H_2S in the produced fluid

$C_{normalized,\,i}$ normalized concentration value

$C_{reservoir}$ initial concentration observation

$C_{reservoir,\,i}$ concentration observation adjusted to the reservoir condition

$C_{simulated}$ simulated concentration of CO_2/H_2S in the reservoir fluid

k absolute permeability

L model parameter in analytical models

$C(y, \hat{y})$ Cauchy loss function.

Q volume production rate

R distance between the injector and producer

R retardation factor

SF safety factor

U Heaviside step distribution

c hyperparameter of the Cauchy loss function

c solute/tracer concentration

m mass of tracer entering the stream tube

t time

w ratio of transport along the fracture to transport out of the fracture

y model value.

α mechanical dispersivity

ϕ porosity

CHAPTER 1

INTRODUCTION

Among all other greenhouse gasses present in the atmosphere such as methane (CH_4), nitrous oxide (N_2O), and other industrial gases, carbon dioxide (CO_2) is the dominating component when compared to the others. According to Caesar et al. (2021), CO_2 accounts for nearly 66% of the total greenhouse gas emissions with the highest recorded concentration of 413.2 ppm in 2020 (Ciavarella et al., 2021) which is approximately 50% larger when compared to the pre-industrial levels, which are around 278 ppm (Meure et. al. 2006). Furthermore, the findings of Caesar et al. (2021) from 139 monitoring stations between the years 1985 and 2020 indicate a continuous upward trend in atmospheric CO_2 concentrations without any observed regression during that period (Figure 1-1).

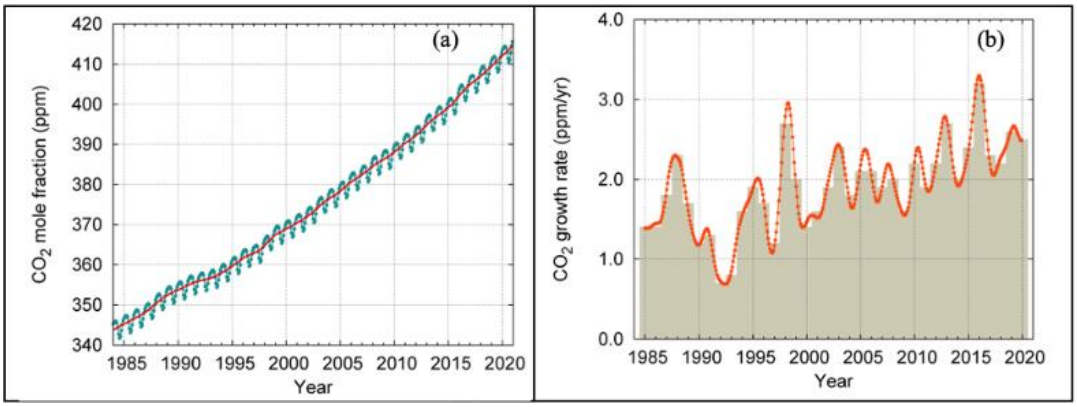

Figure 1-1 Globally averaged CO_2 mole fraction (a) and its growth rate (b) from 1984 to 2020 (WMO, 2021).

Although numerous factors contribute to the continuous increase in the abundance of CO_2 in the atmosphere, an important contributing factor is the increase in the demand for fossil fuels. According to the IPCC (2014), 78% of the total greenhouse gas emissions have been directly linked with fossil fuel combustion and industrial processes, making fossil fuel usage the leading cause of greenhouse gas emissions followed by agriculture, deforestation, and other land-use changes.

The increase in CO_2 emissions to the atmosphere comes with severe consequences, including the rise in the planet's average temperature. According to the IPCC (2021), the increase in the atmospheric temperature has reached nearly 1.1 °C since pre-industrial times and it is expected to reach 1.5 °C within the next few decades. Therefore, it is imperative to take measures to mitigate CO_2 emissions in today's world.

Mainly, two ways stand out to reduce CO_2 emissions first of which is the source-oriented options, which indicate the energy transition from the primary energy sources mainly the fossil fuels to the low-carbon alternatives. Among those alternatives geothermal energy is considered a renewable and low-carbon energy source, offering a promising solution.

Geothermal energy is the extraction of heat that is generated by the continuous radioactive decay of potassium, uranium, and thorium in Earth's crust and mantle, as well as the friction generated by the movement along the margins of the continental plates. In areas with tectonic or volcanic activity, magmatic intrusions generate high geothermal gradients. If there exists an extraction fluid mainly water and steam, with a sufficient amount of permeability and pore space, the extraction of geothermal energy is possible. Figure 1-2 provides a hypothetical representation of a geothermal system. The extracted heat can be utilized in numerous ways depending on the temperature of the produced fluid. Those utilizations can mainly be divided

into two categories first of which is the direct-use applications such as district heating which takes advantage of low-temperature geothermal resources ranging from 50 to 150 °C. On the other hand, electricity generation is the most significant and economically viable type of utilization for geothermal resources in high enthalpy reservoirs (> 150 °C). As reported by IRENA and IGA (2023), the total installed capacity has reached 15.96 GW_e as of 2021 worldwide.

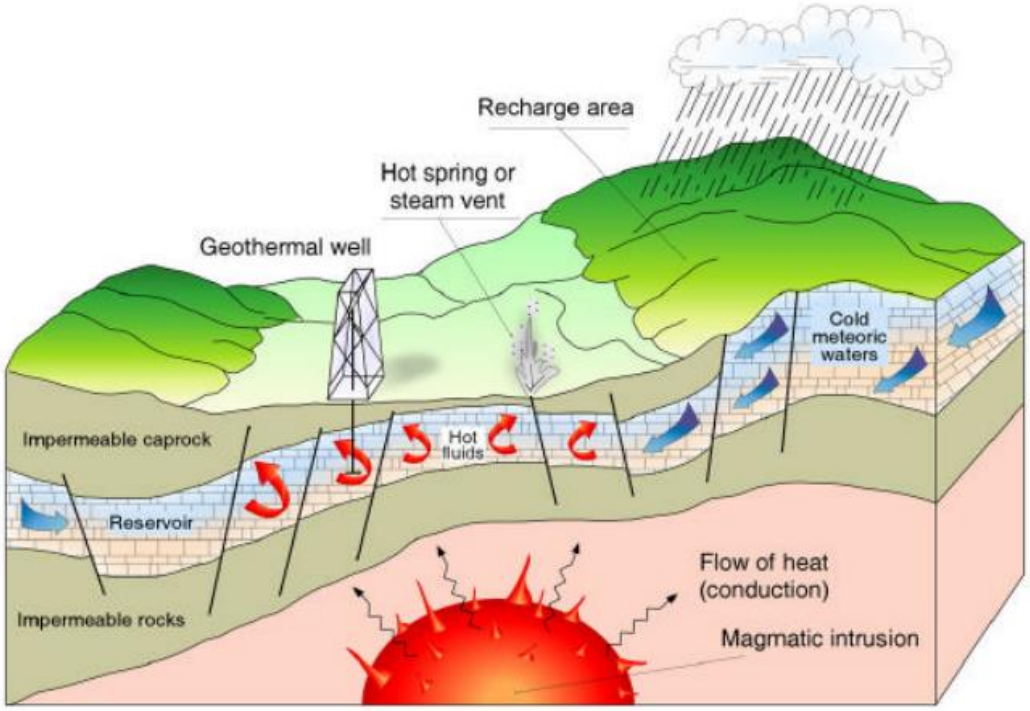

Figure 1-2 Schematic representation of a hypothetical geothermal system (Dickson and Fanelli, 1995)

Despite geothermal energy being regarded as a clean energy source that produces approximately one-sixth of greenhouse gases when compared to natural gas; however, it is important to acknowledge that certain regions experience relatively high concentrations of CO_2 and H_2S emissions from geothermal power plants. Bertani and Thain (2002) reported CO_2 emissions and power production information

from 85 geothermal power plants in 11 countries with a combined capacity of 6,648 MW in 2001, corresponding to 85% of the total installed geothermal power capacity globally. The study revealed a wide range of CO_2 emissions, varying from 4 to 740 g/kWh, with a weighted average of 122 g/kWh. Notably, certain geothermal systems such as the Büyük Menderes Graben and Gediz Graben in Turkey, and Mount Amiata in Italy, exhibited exceptionally high CO_2 emissions. In Turkey, Martinez et al.(2016) gathered data from 12 geothermal power plants located in the Büyük Menderes and Gediz Graben and reported the average CO_2 emissions as 887 g/kWh which is comparable to emissions from coal-fired electricity generation (≈900 g/kWh) which brings us to the second way of reducing the CO_2 emissions that is the sink-oriented options, which indicate the storage of CO_2 in minerals and geological formations involving depleted gas and oil reservoirs, deep saline aquifers or injection of CO_2 into basalt formations for mineral carbonation.

In recent years, the attention to carbon storage through mineralization in basaltic geothermal reservoirs has risen from the demonstrated outcomes of the Carbfix-1 and Carbfix-2 projects to reduce the emissions resulting from the co-produced CO_2 and H_2S. The method that has been used in both projects consists of re-injecting the effluent fluid by mixing it with the captured CO_2 from the geothermal power plants. Notably, the Carbfix-2 project achieved rapid mineralization of CO_2 at the Hellisheiði geothermal power plant in SW Iceland, where the reservoir temperature is approximately 260 °C. (Gunnarsson et al. 2018, Clark et al. 2020, Ratouis et al. 2022).

Building upon the experiences of the Carbfix-1 and Carbfix-2 projects, Geothermal Emission Control (GECO) H2020 project has been initialized to assess the applicability of the Carbfix method in different geological formations across four geothermal power plants for which the Kızıldere geothermal site in Turkey was one

of the demonstration sites to observe the outcomes of the method in metamorphic schist and marble host rocks at a temperature of 220 °C.

The injection of the CO_2-water mixture into the geothermal reservoirs, in its nature, is a coupled process for which the re-injection and production of reservoir fluids alter the temperature and pressure of the reservoir. Additionally, interactions between the injection fluid and the surrounding host rock lead to precipitation-dissolution reactions. Therefore, accurate numerical models are essential for monitoring and forecasting the behavior of the geothermal system. These models should accurately model thermo-hydro-chemical alterations while incorporating various monitoring data, such as static and dynamic pressure and temperature observations, as well as multi-well tracer tests.

In the case of the Kızıldere field, previous modeling experiences indicate limited mineral carbonation due to low concentrations of cations such as Ca^{+2}, $Fe^{+2,}$ and Mg^{+2} in the reservoir for which those cations are the most suitable to form carbonate minerals thus, solubility trapping and structural trapping are the primary trapping mechanisms for the sequestration of the CO_2 (Erol et al. 2022, GECO 2023). Consequently, a non-isothermal hydrodynamic transport simulation is more feasible than computationally demanding reactive transport simulations for monitoring and forecasting the impact of CO_2-water mixture injection.

Based on those findings, this study presents an extensive numerical model for the Kızıldere geothermal site, employing a transient fully coupled thermo-hydrodynamical transport simulation using the TOUGH2 simulator. The model incorporates the geological characteristics of the Kızıldere field, including faults and formation boundaries. The modeling procedure involves the natural state simulation for calibration of the static pressure and temperature measurements of the observation wells by using the equivalent porous medium approach. In the dynamic

calibration process, the hydraulic parameters and flow paths between injection and production wells are determined by treating the chloride contents of the wells as a conservative tracer. Additionally two different slug tracer injection tests by matching the first arrival and mean arrival times, peak concentrations, and the total recovery of the tracers. Subsequently, long-term forecasting has been conducted by examining various injection scenarios with different durations and re-injection rates, including the current field strategy, under constant rates and different sets of constant pressure conditions for the production wells.

CHAPTER 2

LITERATURE REVIEW

Developing a comprehensive numerical model for CO_2 sequestration applications is a complex endeavor, primarily due to the inherent uncertainties in the system and the coupled nature of the physics involved. Therefore, it is crucial to evaluate significant previous studies in this field.

The first part of this chapter will delve into the fundamental mechanisms responsible for trapping CO_2, including structural and stratigraphic trapping, residual trapping, solubility trapping, and mineral trapping. Subsequently, an examination of major projects will be conducted to assess their feasibility and safety aspects in the context of the sequestration process.

The third section will focus on modeling studies that encompass both CO_2 sequestration investigations and model calibration studies, utilizing similar data sources as our system. Finally, the mathematical foundations of the TOUGH2 simulator will be elucidated in the last section.

2.1 CO_2 Trapping Mechanisms

Sequestration of CO_2 in the geological media depends on physical and chemical mechanisms to safely store the injected CO_2 in the porous medium. Although minor trapping mechanisms are also involved in the process, there are four major trapping mechanisms: structural trapping, residual trapping, solubility trapping, and mineral trapping.

2.1.1 Structural Trapping

Firstly, structural trapping of CO_2 refers to the immobilization of either the injected CO_2-fluid mixture or supercritical CO_2 beneath a low permeable caprock with a sufficient amount of pore space in the injected media. This type of trapping occurs in structural or stratigraphic features with vertical and lateral seals, preventing CO_2 leakage through the caprock while allowing for accumulation. It is an essential trapping mechanism for any storage site since it occurs during the injection immediately, allowing time for another trapping mechanism to come into play (Bachu et al. 1994).

2.1.2 Residual Trapping

The residual trapping of CO_2 occurs due to the capillary pressure and relative permeability characteristics. At the beginning of CO_2 injection into the formation, gas saturation in the reservoir increases in a drainage process. Under the same thermodynamic conditions, since the density of the gas phase is smaller than the existing reservoir fluids, the gas phase migrates upward and laterally from the injection wells forming a plume of gas.

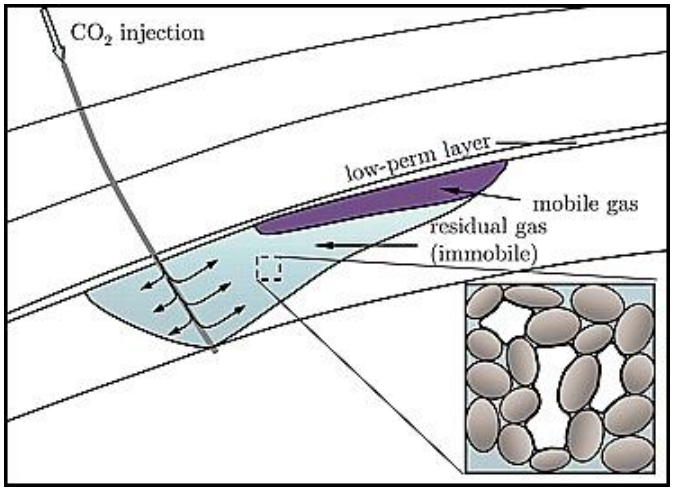

Figure 2-1 Schematic of the trail of residual CO_2 that is left behind because of snap-off as the plume migrates upward during the postinjection period (Juanes et al. 2006).

After the injection stops, the transport of the gas plume continues to displace the water resulting in a higher gas saturation at the leading end of the gas plume; however, at the trailing end of the plume, water displaces the gas phase as an imbibition process causing a snap-off in the gas plume (Fig 2-1) consequently, immobilization of CO_2 (Flett et al. 2004, Krevor et al. 2015, Juanes et al. 2006).

2.1.3 Solubility Trapping

The solubility trapping mechanism refers to the dissolution of the injected CO_2 with the formation water in the reservoir. The degree of dissolution is affected by various factors such as pressure, temperature, and salinity of the formation water. Whether the water keeps its position or flows through the porous media, the CO_2 will remain in the aqueous state as long as the physical conditions remain constant. Furthermore, convection currents in the reservoir beneath the gas plume resulting from the density difference between the CO_2-rich water and reservoir fluids, enhance the dissolution of CO_2 in the formation water (Ennis-King and Paterson, 2005, Holtz, 2002).

2.1.4 Mineral Trapping

Mineral trapping also referred to as carbon mineralization is the trapping mechanism that involves the formation of carbonate minerals (calcite, magnesite, dolomite, siderite) through the geochemical reactions between the injected CO_2 and the surrounding host rock preferably rich in calcium and magnesium (Gunter et al., 1993, Oelkers et al. 2008). It stands out as a privileged trapping mechanism as not only it allows the immobilization of CO_2 for a much greater period but also the formation of solid carbonate minerals ensures the safety aspect of the sequestration process.

Snæbjörnsdóttir et al. (2020) described the occurrence of some chemical reactions altered by the CO_2 injection process. First of all, CO_2 dissolves in the formation water forming weak carbonic acid followed by the dissociation of carbonic acid resulting in the formation of the bicarbonate ion:

$$CO_{2(g)} + H_2O = H_2CO_3 \quad (1)$$

$$H_2CO_3 = H^+ + HCO_3^- \quad (2)$$

The resulting increased concentration of hydrogen cations causes the pH to decrease which triggers the dissolution of the primary minerals. Consequently, the complexing of dissolved cations with the bicarbonate ion occurs such as

$$Ca^{+2} + HCO_3^- = CaHCO_3^- \quad (3)$$

The reaction of the divalent cations which are the positively charged ions having $^{+2}$ valency, with the dissolved bicarbonate species results in the formation of Ca^{+2}, Mg^{+2}, and Fe^{+2} carbonates for which the CO_2 mineralization has reached.

$$HCO_3^- + Ca^{+2} = CaCO_{3(s)} + H^+ \quad (4)$$

$$HCO_3^- + Mg^{+2} = MgCO_{3(s)} + H^+ \quad (5)$$

$$HCO_3^- + Fe^{+2} = FeCO_{3(s)} + H^+ \quad (6)$$

The extent, relative contribution, and storage security of the aforementioned trapping mechanisms are highly site-specific and vary over the timescale. Figure 2-2 shows the relative contribution of the respective trapping mechanisms for both the sedimentary formations and mafic or ultra-mafic formations over time. Regardless of the main contributing trapping mechanism, structural trapping plays the initial role, which immediately takes place during the injection process; however, the structurally trapped CO_2 becomes residual and dissolves into water over time. On the other hand, the mineral trapping mechanism is heavily dependent on the composition of the host rock. In sedimentary basins (Figure 2-2, left panel), both the rate and the amount of CO_2 that can be trapped in the reservoir are limited and the injected CO_2 may remain mobile for long periods where the trapping is governed by the structural and solubility trapping. However, rapid mineralization of CO_2 can

occur in mafic and ultramafic rocks due to the high abundance of cations such as Mg^{+2} and Ca^{+2}, thus, the mineral trapping mechanism may take over as the dominating trapping mechanism in shorter timescales (Figure 2-2, right panel).

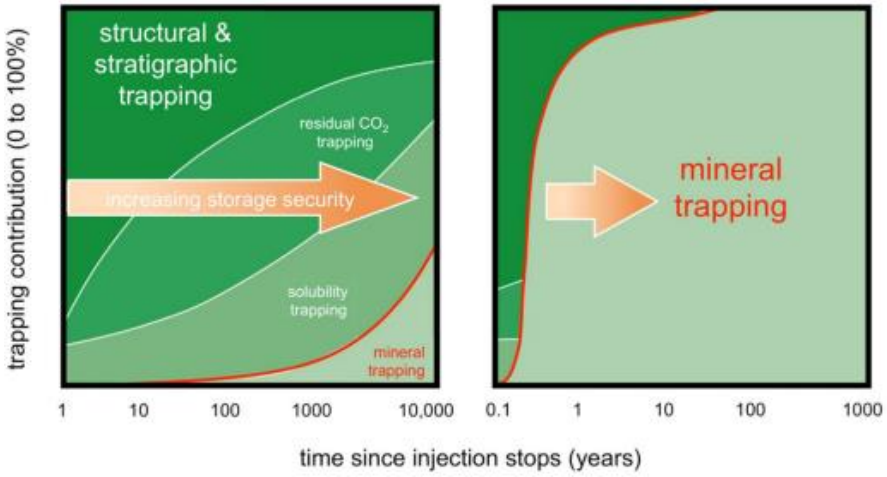

Figure 2-2 The relative contribution of trapping mechanisms. The left panel corresponds to the sedimentary formations and the right panel corresponds to the mafic/ultramafic formations. (Kelemen et al., 2019)

2.2 CO_2 Sequestration Projects in Geothermal Reservoirs

Since the initial implementation of commercial-scale CO_2 sequestration in Sleipner, Norway (Torp and Gale, 2004), numerous projects have been initiated to sequester CO_2. These projects involve the injection of CO_2 into depleted oil and gas reservoirs, deep saline aquifers, and coal seams. On the other hand, geothermal reservoirs are a relatively new target of CO_2 sequestration applications. In this section, the primary focus is the projects and related works on the sequestration of CO_2 in geothermal reservoirs.

2.2.1 The Carbfix Pilot Project, Iceland

The Carbfix Pilot Project also known as the Carbfix-1 project was initialized in 2007 to observe the impact of the injection of CO_2-charged water into the basaltic

formations in field-scale applications (Gislason et al 2010). The subjected pilot injection field is the Hellisheiði field where a geothermal power plant is situated in SW Iceland. The injection method applied in the project requires the mixing of the captured CO_2 with the effluent fluid for reinjecting it back into the reservoir as a single-phase mixture. The injected CO_2 in the aqueous phase in the formation fluid transports in the basaltic rocks transforming into bicarbonate and carbonic acid. The dissociation of the bicarbonate and carbonic acid ions increases the acidity of the brine triggering a series of complex chemical reactions that lead to the immobilization of the CO_2 in the form of carbonate minerals.

Through the Carbfix project, various modeling studies have been conducted including reactive and non-reactive transport models for describing both flow and transport mechanics, and reaction kinetics of the injection site.

Khalilabad et al.(2008) conducted a preliminary aquifer characterization by modeling the tracer recovery using the TRINV simulator for a slug Na-fluorescein injection conducted from the well HN-02 at the CO_2 injection target zone in the Hellisheiði-Threngsli field. The tracer sampled from the well HN-04 indicated a total mass recovery of 50% in 125 days. The developed model yielded the best results with the multi-channel approach with three flow channels. The modeled channels indicated that the majority of the transported volume is through a homogeneous thick layer with a uniform network of interconnected porosity resulting in high tortuosity and a large cumulative reactive surface area between the injected CO_2 and the hosting basalt rock.

The first 3D field-scale simulation work for the injection process has been conducted by Aradóttir et al.(2009). The developed model consisted of all wells in the target injection zone except wells HK-13 and HK-07B. The modeling aimed to calibrate the flow paths between the target injection well HN-02 and HN-04 based on the tracer test conducted by Khalilabad et al.(2008) subsequently setting a basis for the reactive transport simulation of the injection zone. The results of the model calibration presented by the authors showed that the horizontal permeability in the

Carbfix re-injection zone is approximately 500 mD whereas, the vertical permeability is 300 mD. Furthermore, the obtained porosity value is 4% which is a significantly lower value compared to the Icelandic basalts.

A more comprehensive, multidimensional reactive transport model was constructed by Aradottir et al. (2012) based on the previous calibration studies (Khalilabad et al. (2008), Aradottir et al. (2010), Aradottir et al. (2011)). The study covered 5 distinct transport models, which couple 2D and 3D models, reactive and non-reactive transport, and thermal and isothermal processes for the pilot CO_2 injection scenario which was 1,200 tons/year, and a full-scale 400,000 tons CO_2 injection scenario. The findings of the study revealed that 100% of mineralization of the injected CO_2 occurs in 3D reactive transport simulations in the pilot injection scenario whereas, 2D reactive transport simulations predicted 80% mineral capture within 100 years for the full-scale injection case. Furthermore, significantly lower predictive values were obtained from the non-reactive mass transport simulations compared to the reactive transport simulations in the respective injection scenarios, because reactive transport simulations showed that the injected CO_2 is retained by solid phases. Overall, high mineralization values were observed during the reactive transport modeling thus, it was concluded from this study that fresh basalts may comprise ideal geological CO_2 storage formations as in the case of the Hellisheidi geothermal field.

The demonstration of the Carbfix method during the Carbfix-1 project successfully resulted in the mineralization of 200 tons of injected CO_2 as carbonate minerals during 2012 and 2013 (Gíslason et al., 2018). The pilot injection study demonstrated that 95% of the injected CO_2 was precipitated as calcite minerals in the lower section of the Hellisheidi reservoir with temperatures ranging between 20 to 50 °C. (Snæbjörnsdóttir et al. (2017), Matter et al. (2016), Pogge von Strandmann et al. (2019)).

2.2.2 Carbfix-2 Project, Iceland

On top of the demonstration of successful outcomes in terms of rapid mineralization of the injected CO_2 into basaltic rocks in the Carbfix-1 project (Snæbjörnsdóttir et al. (2017), Matter et al. (2016)), the Carbfix-2 project was initialized for the upscaling of the Carbfix method with more ambitious injection goals at the Hellisheiði geothermal power plant into geothermally altered basalts at temperatures of 260 ℃ (Gunnarsson et al., 2018).

The initial work was carried out by Gunnarsson et al. (2018) on the capture and injection of the CO_2/H_2S charged fluid into the reservoir, sampling of dissolved CO_2, H_2S, sulfate, and 1-naphthalene-sulfonate tracer injected into the reservoir from the pilot injection well HN-16. Based on the approach proposed by Matter et al. (2016), a simple equation was proposed for the calculation of the fraction of gases mineralized in the subsurface.

$$Fraction\ Mineralized = \frac{C_{simulated} - C_{measured}}{C_{simulated} - C_{background}} \quad (7)$$

where,

$C_{simulated}$ is the simulated concentration of CO_2/H_2S in the reservoir fluid

$C_{measured}$ is the sampled concentration of CO_2/H_2S in the produced fluid

$C_{background}$ is the average background concentration of CO_2/H_2S before the first arrival of the injected gas

In their modeling study, the simulated concentrations of the CO_2/H_2S values were calculated by the dilution and mixing affected the fluid compositions and the measured values of 1-naphthalene-sulfonate. Those calculated values are higher when compared to the monitoring values indicating a loss of CO_2 and H_2S in the subsurface. According to the authors, the only possible reason for this loss is the carbon- and sulfur-bearing mineralization where over 50% of the injected CO_2 and

76% of the injected H_2S were mineralized between the first arrival of 1-naphthalene-sulfonate and the end of the monitoring period.

Snæbjörnsdóttir et al. (2018) developed a reservoir model for modeling a tracer test injected from the well HN-17 based on a simplified version of the Husmuli injection site using the TOUGH2 simulator for characterizing the possible flow paths in the reservoir. Three approaches for the calibration of the flow paths were implemented. The first approach that has been used was constructing a homogeneous model, which assumed that the fluid flow occurs only because of the fluctuations in the pressure resulting from the continuous fluid injection and withdrawal. The second approach was to extend high permeable single channels from the main feed zones between the injection and the production wells. The final approach was the multi-channel approach similar to the single-channel approach but it included the combination of high permeable channels along the same feed zones of the wells. The modeling study concluded that due to fast tracer arrival times, a homogenous approach was not appropriate as the tracer recovery was both limited and late. On the other hand, single-channel and multi-channel approaches resulted in more realistic tracer recoveries in terms of arrival times and peak concentrations.

Further advancements in terms of hydraulic transport in the Husmuli injection site were conducted by Ratouis et al. (2019) by constructing a TOUGH2 model apart from the previous modeling studies (Snæbjörnsdóttir et al., 2018, Kristjánsson et al., 2016) for calibrating the tracer recovery conducted from the HN-17. Both the single porosity approach and the method of Multiple Interacting Continua (MINC) for the dual porosity approach were used. Significantly better results were obtained by the dual porosity approach with a high degree of anisotropy compared to the single porosity approach in which no tracer returns were observed. Furthermore, the modeling results also indicated that the flow is driven by the difference in buoyancy between the cool injected fluid and the surrounding formation which is a preferential mechanism in terms of the storage capacity due to a greater rock surface area would be in contact with the CO_2-charged injection fluid.

Extensive sampling, geochemical analysis, and mass balance calculations were conducted by Clark et al.(2020) to assess the 3.5 years of continuous injection in the Carbfix reservoir. The results of the study showed that after the injection capacity of the Carbfix condensate doubled in July 2016, an increase in the mineralization rate has been observed. Over 60% of CO_2 and 85% of H_2S were mineralized when compared to the first phase of the injection (Gunnarsson et al. 2018). The possible underlying reason for the increased mineralization stated by the authors is a greater degree of dissolution near the injection well due to the increased acidity in the injection water resulting from the dissolved gas concentration. Furthermore, the primary carbonate minerals precipitated in the reservoir were calcite and dolomite according to the saturation indices and predominance diagrams.

A more recent 3D non-reactive numerical model for characterizing the Carbifx re-injection site was developed by Ratouis et al. (2022) with a dual porosity approach to estimate the fraction of dissolved gas mineralization between the injection well and monitoring wells. Hydraulic parameters of the flow paths have been calibrated both by a slug tracer test and a continuous tracer test by matching the residence times, and total recovery of the tracer. Furthermore, the thermal response of the reservoir was validated by matching the enthalpy from the monitoring wells. The prediction of the fraction of dissolved gas mineralization was performed by the comparison of the monitored and modeled CO_2 using the approach proposed by Matter et al. (2016). The model results showed that the degree of mineralization is 70% for the well closest to the injection and 95% for the furthest well which were similar compared to the findings of Clark et al.(2020). Thus, the developed numerical model suggested that non-reactive simulation procedures can be deployed for monitoring the mineralization process. Finally, a theoretical maximum estimate of the mineralization process was estimated considering the thermal stability of the carbonates (290 °C for the hydrothermally altered basaltic rocks in Iceland, Franzson, 2000) and the available pore space in the re-injection zone. It has been concluded that in the Carbfix re-injection zone, approximately 300 Mt of CO_2 can be mineralized even if only 10% of the pore space is available to be filled.

Since the method's first demonstration campaign in 2014 through the Carbfix-1 project and the first initiation of the field scale injection through the Carbfix-2 project, over 92,000 tonnes of CO_2 have been injected into the Carbfix re-injection reservoir (carbfix.com).

2.2.3 GECO Project

Building upon the completion of the successful and safe injection of the CO_2-charged re-injection of brine into basaltic, high-temperature reservoirs in the Carbfix-2 project, the Geothermal Emission Control (GECO) H2020 project has been established in 2018 to lower the emissions related to the geothermal electricity production by capturing the non-condensable gases for geological storage. Those goals were aimed to be reached by:

1. Further optimization of the capture and injection infrastructure at the Hellisheidi.
2. Observing the impact of the re-injection of the Carbfix condensate in different demonstration sites with different reservoir rocks.
3. Integrating the success of the Carbfix method with complementary techniques for gas re-utilization.

Under the GECO project, 4 demonstration sites located in Iceland, Italy, Turkey, and Germany have been selected for which each demonstration site has distinctive geological features.

2.2.3.1 Kızıldere Geothermal Power Plant (Turkey)

Kızıldere geothermal field is located in the Denizli Province, southwestern Turkey. Currently, it is the largest geothermal field composed of three power plants with a combined 240 MW of installed capacity. The Kızıldere geothermal field is characterized by its close association with a significant fault along the northern

boundary of the Büyük Menderes graben. This geothermal reservoir is situated within the Menderes massif, recognized as one of Turkey's oldest basement massifs. It is composed of distinct geological components, including a gneiss-core, a less metamorphosed cover series, and a deformed volcano-sedimentary sequence. Within the Kızıldere geothermal system, two separate reservoirs exist. The first reservoir is located at a relatively shallow depth and is hosted by Miocene limestones. It exhibits temperatures ranging from 196 to 200°C. The second reservoir is found at greater depths within Paleozoic marbles and is characterized by temperatures ranging from 200 to 212°C.

The initial studies have been conducted in GECO (2020) in terms of conceptual modeling, natural state modeling, and reactive transport modeling of the injection site for the Kızıldere field. The 3D geological model has been constructed in terms of fault and horizon modeling and structural griding based on the conceptual of the Kızıldere geothermal field and two sets of slickenlines measured from the Gebeler fault (Aksu, 2019). Furthermore, a sector model methodology has been adopted for modeling a narrower area around the injection well KD-50A to handle the computational demand of reactive transport modeling. During the natural state modeling, the fracture properties of the Kızıldere field were estimated using the mud-loss data subsequently, a range of permeability values of the reservoir section were calculated with the fractal approach. Furthermore, with those values, a sensitivity analysis was performed for the calibration of the model in terms of static pressure and temperature measurements. Ahead of 1D and 3D reactive transport models, a geochemical mixing model was developed to demonstrate the chemical composition of the CO_2-charged water in reservoir conditions in the vicinity of the injection well as well as the reaction path modeling to investigate the reaction paths of CO_2-water-rock interactions in a batch system, analyzing thermodynamic properties, chemical equilibrium, and kinetic reactions, and assessing the impact of parameters such as grain size, specific surface area, and volume fractions of minerals. In reactive transport modeling, both 1D transport models were used with the average distances between the pilot injection well and each observation well and the 3D reactive

transport model covering the boundaries of the localized model around the injection well (Erol et al. 2022). For each modeling approach, different rates of injection scenarios coupled with different rock compositions including schist, schist-marble, and marble host rocks. The findings of the transport models indicate that the dissolved CO_2 reacts faster through carbonate rock minerals such as calcite and iron carbonate and become neutralized forming bicarbonate or other carbonate ions, especially in marble formations. The CO_2-charged brine acts as a weak acid and reacts with feldspar and clay minerals where the reaction kinetics can be considered to be slow when compared to the carbonate minerals. Furthermore, being the more permeable medium, the fractured marble and quartzite formations host the majority of the fluid flow whereas the schist-bearing formations have low permeability values indicating that carbonate precipitation may occur through the fractures due to the dissociated ions from the schist minerals such as Mg^{+2}, K^{+} and Fe^{+2} according to the 1D reactive transport simulations.

A 3D reactive transport model was developed by Erol et al.(2022) which followed a localized model approach including 9 nearby wells and the pilot injection well with TOUGHREACT to predict the effects of the fluid- CO_2 injection into the Kızıldere field. The model has been calibrated by the pressure and temperature measurements taken from the observation wells as well as the dynamic pressure history of the pilot injection well. The impact of the fluid- CO_2 injection was examined by three annual injection rates which include 500, 2000, and 4000 tons of CO_2 per year for ten years of continuous injection with different rock types abundant in the reinjection zone consisting of marble, quartzite, and schist. According to the study, the mineralization of CO_2 is limited in the Kızıldere reservoir due to high prior concentrations of CO_2 in the reservoir (~ 3%, Haizlip et al., 2013). Furthermore, the formation of secondary minerals such as hematite decreases the abundance of divalent cations, which are favorable for carbonization. In addition, the authors proposed that although the Kızıldere field does not exhibit a similar impact for fluid-CO_2 injection to Carbfix projects, the injection still aligns to mitigate the CO_2 emissions as long as the CO_2 remains dissolved in the reservoir fluid.

Prior to the injection of CO_2-charged brine from the pilot injection well, KD-50A, to understand the flow paths and predict the impact of the CO_2-charged brine injection in the injection site, Sevindik et al.(2023) developed a transport model by assuming chloride as a conservative tracer using TOUGH2. In the model calibration, the model parameters were calibrated by utilizing static pressure and temperature data, as well as time-dependent chloride concentration data obtained from the production wells and dynamic pressure observations of the pilot injection well. Prior to injection, the developed model is subsequently employed to make predictions regarding the distribution of CO_2 within the reservoir and the CO_2 content of the produced brine at the production wells. The results of the model indicated that although there exists a sufficient amount of hydraulic connectivity between the injection and the production wells, due to the limited amount of CO_2 injection, no alterations were observed in the production wells in terms of CO_2 concentration thus, the authors concluded that to observe an appreciable alteration in CO_2 content, higher amounts should be injected.

After the injection of CO_2-charged brine was implemented in the Kızıldere field, an updated mass and heat transport model was constructed in GECO (2023) through the calibration of the model with static PT observations, dynamic pressure history, chloride concentrations from production wells, and two slug tracer injection tests. The natural state modeling has been achieved by fitting the static observations through the production casing setting depths with less than 3% error. During the dynamic transport modeling, chloride concentrations have been used as a natural tracer and matched through the production wells. Furthermore, two separate slug tracer injection tests have been calibrated for inverting the hydraulic parameters between the injection and observation wells including the pilot injection well. The calibrated transport model was used for tracking the CO_2-charged brine in a non-reactive fashion. The modeling results indicated that the wells KD-23D, KD-83, and KD-2A experienced the most significant alterations in terms of CO_2 content in the produced fluid respectively. Furthermore, a reactive transport model was constructed based on the updated field evaluations in terms of the mineralogy of the rocks, the

anisotropic permeability, and the connectivity between the wells with the planned injection strategy of 2,000 tons/year of CO_2 injection at 105 °C. The results of the reactive transport model revealed that the mineralization process of CO_2 is limited in the Kızıldere reservoir. Cations such as Ca^{+2}, Fe^{+2}, and Mg^{+2}, which are more suitable for forming carbonate minerals with CO_2, are low in the system. During modeling studies, it has been observed that they react with minerals containing K-Al-Si such as mica and clay, forming some end-members including Montmorillonte-Mg. Furthermore, the high amount of CO_2 content in the reservoir, the low pH, and the present water-rock-CO_2 interactions can be considered minor effects that affect the carbonization process. Although the study showed that the mineralization of CO_2 is limited in the reservoir, solubility trapping in the Kızıldere reservoir is a dominant mechanism that may aid the mitigation process of CO_2 emissions. Based on the injection of 2,000 tons of CO_2 in a year, the authors concluded that through 10 existing injection wells in the Kızıldere geothermal field, 200,000 tons of CO_2 can safely be injected into the reservoir for 10 years of continuous injection.

2.3 Numerical Modeling of Subsurface Mass and Heat Transport and TOUGH2

Numerical modeling of subsurface mass and heat transport involves using mathematical equations and computer simulations to characterize, predict, and optimize subsurface systems of increasing complexity. The formulation of a precise numerical model that accurately simulates the mass and heat transport necessitates the comprehensive processing of a substantial volume of data regarding the domain area which usually encompasses the implementation of the following steps (Bundschuh, 2010).

- Setting the objectives of the model
- Development of a conceptual model for the subsurface system regarding the geology of the reservoir alongside the physical and chemical properties of the system relevant to the mass and heat transport.

- The establishment of a mathematical model that includes the governing equations that describe the information regarding both the conceptual model and the physical phenomenon.
- Numerical discretization of the governing equations into a numerical grid system which involves dividing the subsurface domain into a series of grid cells or elements. The governing equations are approximated using numerical methods such as finite difference, finite element, or finite volume methods.
- Assignment of the boundary conditions.
- Numerical solution of the discretized equations along with the initial and boundary conditions which involves solving a system of algebraic equations at each time step to update the numerical values throughout the domain.
- Calibration of the numerical model to optimize the model parameters by populating the model with the measurements taken from the field until a satisfactory agreement is reached between the measurements and the numerical solution.
- Validating the numerical model to assess the extent to which the model accurately represents the real-world phenomenon by utilizing field data that have not been employed in the calibration process of the model. From the comparison of the model prediction with the independent field data, the reliability and fidelity of the model can be ascertained.
- Conduction of sensitivity analysis to determine the relative impact of model parameters on the numerical solution.
- Scenario simulations, which involve the evaluation of different scenarios to assess the potential outcomes under different conditions or management strategies.

Numerous commercial and non-commercial software packages have been developed to effectively model heat and mass transport within porous and fractured media. Notable examples include COMSOL Multiphysics®, FEFLOW (Diersch, 2014), CMG STARS (Computer Modeling Group, 2007), and TOUGH2 (Pruess et al., 1999). These simulators have gained significant recognition and are esteemed for

their extensive applicability across various domains within the field. This section primarily focuses on the workflow employed by TOUGH2, as it is the chosen modeling tool in this dissertation.

2.3.1 TOUGH2 Simulator (Transport of Unsaturated Groundwater and Heat)

TOUGH2 (Pruess et al., 1999) is a computational tool specifically developed to conduct numerical simulations of multi-dimensional fluid and heat flows involving multiphase, multicomponent fluid mixtures within porous and fractured media. Its versatile applications span various fields, including geothermal reservoir engineering, nuclear waste isolation studies, environmental assessment and remediation, and the analysis of flow and transport in variably saturated media and aquifers.

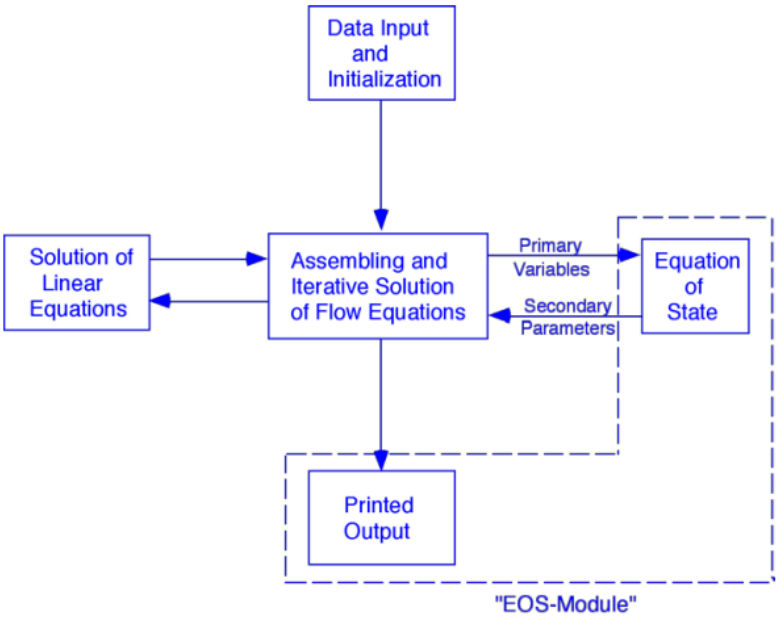

Figure 2-3 Modular architecture of MULKOM and TOUGH2, Pruess et al. 1999

The capabilities of the architecture that TOUGH2 implements (Figure 2-3) stands out from its counterparts because aside from providing iterative solution of fluid flow and heat transfer equations, it couples those solutions with various equation-of-state

modules, which define the components and phases and related thermophysical properties of the fluid mixture being considered.

2.3.1.1 Mass and Energy Balance

According to the Reynolds Transport Theorem, the rate of change of an extensive property of a system with respect to time is equal to the sum of the rate of change of property per unit time for a control volume and the rate of efflux of the property. The general form of the Reynolds Transport Theorem can be written as

$$\frac{d}{dt}\int_{V_n} M^{(\kappa)} dV_n = \int_{\Gamma_n} F^{(\kappa)} \cdot n d\Gamma_n + \int_{V_n} q^{(\kappa)} dV_n \qquad (8)$$

The above equation describes the mass or energy balance equations over an arbitrary subdomain V_n bounded by the close surface Γ_n. The component M in the LHS of the equation denotes the accumulation term for either mass or energy per unit volume whereas F denotes the mass flux component.

The superscript κ ranging from 1 to NK labels the mass components in the system. For each component in a given domain, the individual mass accumulations are described by the summation of the multiplication of the saturation and density for all phases and the mass fraction for each mass component that saturates the system respectively. Thus, the general form of the mass accumulation term in a multiphase system can be formulated as

$$M^{(\kappa)} = \phi \sum_{\beta=1}^{NPH} S_\beta \rho_\beta X_\beta^\kappa \qquad (9)$$

where ϕ denotes the porosity, S_β denotes the saturation of the fluid phase β, ρ_β denotes the density of phase β and X_β^κ is the mass fraction of component κ present in phase β.

Similarly, heat accumulation in a multiphase system is

$$M^{(\kappa+1)} = \phi \sum_{\beta=1}^{NPH} S_\beta \rho_\beta u_\beta + (1-\varphi)\,\rho_R C_R T \qquad (10)$$

where the superscript $\kappa + 1$ labels the heat component, u_β denotes the internal energy of fluid phase β. The second term on the RHS resembles the heat accumulation associated with grain volume.

The mass flux terms are associated with the mass fraction of the phases for each component multiplied by the phase fluxes.

$$F^{(\kappa)} = \sum_{\beta=1}^{NPH} X_\beta^\kappa F_\beta \qquad (11)$$

The individual fluxes for each phase can be calculated by the multiphase version of Darcy's law assuming that the flow regime in the media is laminar.

$$F_\beta = -k \frac{k_{r\beta}}{\mu_\beta} \rho_\beta (\nabla P_\beta - \rho_\beta g) \qquad (12)$$

where F_β is the mass flux for the phase β, k is the absolute permeability, $k_{r\beta}$ is the relative permeability of the phase β, μ_β and ρ_β are the viscosity and density of the phase β respectively and P_β is the phase pressure which is equal to the sum of the pressure P of a reference phase and the capillary pressure of phase β relative to the reference phase. For the calculation of the gas phase permeability, the Klinkenberg relationship has been applied where $k = k_0(1 + \frac{b}{P})$ for which the term k_0 is the absolute permeability at the infinite pressure condition.

Furthermore, the term $F^{(NK+1)}$ denoting the heat flux including the convective and conductive components can be expressed as

$$F^{(NK+1)} = -K\nabla T + \sum_\beta h_\beta F_\beta \qquad (13)$$

where K is the thermal conductivity of the medium and h_β is the specific enthalpy of phase β.

2.3.1.2 Space and Time Discretization

The aforementioned conservation equations for both mass and heat are discretized in space using the integral finite difference method (Narasimhan and Witherspoon, 1976) in TOUGH2 by using an approximate volume average for both the accumulation and the flux terms as follows.

$$\int_{V_n} M dV = V_n M_n \qquad (14)$$

$$\int_{\Gamma_n} F^{(\kappa)} \cdot n d\Gamma = \sum_m A_{nm} F_{nm} \qquad (15)$$

In the RHS of the accumulation volume average, M is a volume-normalized extensive quantity and M_n the average accumulation value of M over the volume element V_n. Furthermore, in the RHS of the flux term, F_{nm} is the average normal flux pointed inwards of F over the area segment A_{nm} between the volume elements V_n and V_m.

Similar to the aforementioned individual phase fluxes, the average normal flux values, F_{nm}, can be calculated by Darcy's law as follows.

$$F_{\beta,nm} = -k_{nm} \left[\frac{k_{r\beta}\rho_\beta}{\mu_\beta}\right]_{nm} \left[\frac{P_{\beta,n} - P_{\beta,m}}{D_{nm}} - \rho_{\beta,nm} g_{nm}\right] \qquad (16)$$

where the subscripts nm denote the average value at the interface between the grid blocks of a particular variable, permeability, gravitational acceleration, distance, and phase fluxes in the equation calculated by suitable averaging methods including interpolation, harmonic weighting, and upstream weighting.

Through the substitution of the accumulation and flux averages into the conservation equation, a set of 1st-order ordinary differential equations concerning time for each volume element can be obtained.

$$\frac{dM_n^{\kappa}}{dt} = \frac{1}{V_n}\sum_m A_{nm}F_{nm}^{\kappa} + q_n^{\kappa} \quad (17)$$

where q_n^{κ} is the sink/source term for the n^{th} volume element and the mass component κ.

To solve the time derivative of the mass accumulation terms for each volume element, TOUGH2 incorporates 1^{st} order finite difference method for time discretization in a fully implicit fashion where all of the flux and the sink/source terms on the RHS of the above equation alongside the thermodynamic properties are expressed in terms of the successive time level t^{k+1}. The discretized equations in time using the finite differences in the fully implicit form accumulated at the same side of the equation yielding a residual for the mass components at each volume element at the time level t^{k+1} resulting in a set of coupled non-linear, algebraic equations as follows.

$$R_n^{\kappa,k+1} = M_n^{\kappa,k+1} - M_n^{\kappa,k} - \frac{\Delta t}{V_n}\left\{\sum_m A_{nm}F_{nm}^{\kappa,k+1} + V_n q_n^{\kappa,k+1}\right\} = 0 \quad (18)$$

the residual term for each volume element and mass component at the t^{k+1} step is denoted by $R_n^{\kappa,k+1}$ where a residual vector can be formed for each volume element in the discretized domain, and the number of equations for the mass and heat components.

$$\begin{bmatrix} R_1^{1,k+1} & \cdots & R_n^{1,k+1} \\ \vdots & \ddots & \vdots \\ R_1^{NK+1,k+1} & \cdots & R_n^{NK+1,k+1} \end{bmatrix} \quad (19)$$

All the elements in the above matrix are non-linear equations that need to be linearized. TOUGH2 employs Newton-Raphson iteration for the linearization process by introducing an iteration index p and expanding the residuals at the iteration step $p + 1$ in a first-order Taylor series. The resulting formulation for the residuals at the above matrix in linearized form is as follows.

$$R_n^{\kappa,k+1}(x_{i,p+1}) = R_n^{\kappa,k+1}(x_{i,p}) + \sum_i \frac{\partial R_n^{\kappa,k+1}}{\partial x_i}(x_{i,p+1} - x_{i,p}) = 0 \quad (20)$$

$$-\sum_i \frac{\partial R_n^{\kappa,k+1}}{\partial x_i}(x_{i,p+1} - x_{i,p}) = R_n^{\kappa,k+1}(x_{i,p}) \quad (21)$$

which resulted in a set of linear equations with the same dimensions. The derivatives in the Jacobian matrix, $\frac{\partial R_n^{\kappa,k+1}}{\partial x_i}$, are calculated by numerical differentiation controlled by the user including the following options.

- Conjugate Gradient Solvers
  - Preconditioned Bi-Conjugate Gradient
  - Bi-Conjugate Gradient
  - Generalized Minimum Residual Conjugate Gradient
  - Stabilized Bi-Conjugate Gradient
- Direct Solvers
  - Sparse Direct Solver
  - Banded Direct Solver

The numerical solver forces the iteration until the relative error criteria are satisfied.

$$\left|\frac{R_{n,p+1}^{\kappa,k+1}}{M_{n,p+1}^{\kappa,k+1}}\right| < Convergence\ Criterion \quad (22)$$

The aforementioned procedure for the numerical solution of mass and heat transport followed by TOUGH2 does not depend on any spatial system in terms of space discretization because the discretization procedure in space only depends on the geometric features/alignment of the volume elements described with the parameters including the grid volumes, interface area and the distance between the nodes. Thus, the procedure allows for simulating irregular discretizations in 3D for both porous and fractured media. However, the thermodynamic properties at the interfaces

appearing in Darcy's equation needed to be in thermodynamic equilibrium which is the most common underlying problem in terms of model convergence.

2.3.1.3 Equation-of-State Modules

The determination of thermophysical properties of fluid mixtures necessary for formulating the governing mass and energy balance equations is facilitated through the utilization of "equation-of-state" (EOS) modules. The flow module of TOUGH2 is designed in a general framework to effectively establish and solve mass balances for a variable number of NK components distributed across NPH phases. The TOUGH2 package includes different equation-of-state (EOS) modules capable of representing various fluid mixtures. The following table is a general scheme of the equation-of-state modules included in the TOUGH2.

Table 2-1 EOS modules included in TOUGH2 (Pruess, 2003)

MODULE	PURPOSE
EOS 1	basic fluid property module for water (liquid, vapor, two-phase), including "two waters" for tracing the fluid movement
EOS 2	water-CO_2 mixtures; originally developed by O'Sullivan et al., (1985)
EOS 3	water-air mixtures; an adaptation of the EOS module of the TOUGH simulator (Pruess, 1987)
EOS 4	water-air mixtures, including vapor pressure lowering according to Kelvin's equation (Edlefsen and Anderson, 1943)
EOS 5	water-hydrogen mixtures
EOS 7	mixtures of water-brine-air
EOS 7R	water-brine-air, plus two volatile and water-soluble radionuclides
EOS 8	fluid property module for the three-phase flow of water, non-condensable gas, and black oil

Table 2.1 (continued)

EOS 9	fluid property module for saturated/unsaturated flow according to Richards' equation (gas phase a passive bystander)
EWASG	fluid property module for three-component two-phase mixtures of water, water-soluble salt, and non-condensable gas; includes salt dissolution and precipitation, and associated porosity and permeability change
T2VOC	The three-phase flow of water, air, and a volatile organic chemical, adapted from Falta et al. (1995)
TMVOC	fluid property module for the three-phase flow of water, non-condensable gas, and non-aqueous phase liquid (NAPL), where the NAPL may consist of a multi-component mixture of volatile organic chemicals

2.4 Analytical Models for Tracer Transport

Analytical models based on the convection-dispersion-diffusion equation play a crucial role in the characterization of subsurface mass transport in porous media, complementing numerical simulation models. Analytical models offer valuable insights into parameters such as the Peclet number and dispersivity, which are essential for understanding subsurface processes. These parameters, which describe the transport behavior, cannot be readily obtained from TOUGH2 alone. By incorporating analytical models alongside numerical simulations, a more comprehensive understanding of subsurface mass transport can be achieved, aiding in improved characterization and analysis.

$$\mathrm{R}\frac{\partial \mathrm{c}}{\partial \mathrm{t}} = \left(D_X \frac{\partial^2 \mathrm{c}}{\partial x^2} + D_y \frac{\partial^2 \mathrm{c}}{\partial y^2} + D_z \frac{\partial^2 \mathrm{c}}{\partial z^2} \right) - u_x \frac{\partial \mathrm{c}}{\partial \mathrm{x}} - u_y \frac{\partial \mathrm{c}}{\partial \mathrm{y}} - u_z \frac{\partial \mathrm{c}}{\partial \mathrm{t}} + \mathrm{s} \qquad (23)$$

where t is time, c is the solute/tracer concentration, R is the retardation factor $D_{x,y,z}$ are hydrodynamic dispersion coefficients, $u_{x,y,z}$ are the Darcy velocities along the respective direction and s is the production term respectively.

Although, based on the convection-dispersion-diffusion equation numerous solutions have been presented (Van Genuchten and Alves 1982, Elsworth and Butters 1993, Cihan and Adrian 2011, Houseworth et al. 2013, Erol et al. 2022a) differ in analyzed geometry, dimensionality, medium properties, and boundary conditions in this dissertation, 4 distinct analytical methods are used to determine transport parameters and to establish a benchmark for the numerical modeling results. Those analytical models include the multi-fracture model (Fossum and Horne, 1982), the fracture-matrix model (Bullivant and O'Sullivan, 1989), and the uniform porous model (Sauty, 1980).

2.4.1 Multi-Fracture Model (Fossum and Horne, 1982)

The multi-fracture model presented by Fossum and Horne, 1982 describes the solute transport between the injection and production well along n number of fractures which can be used for describing transport along a single-fracture or more. The one-dimensional dispersion occurs due to both the high velocity and the presence of molecular diffusion along the fracture.

$$C_t = \sum_{i=1}^{n} e_i C_r \left(\frac{R_i}{u_i}, \ Pe_i\right) \quad (24)$$

$$C_r = J \frac{1}{\sqrt{t}} \frac{2tm}{t} \exp\left(\frac{-Pe \cdot (t - t_m)^2}{4 t_m t}\right) \quad (25)$$

$$J = \left(\frac{m}{4Q}\right)\left(\frac{Pe_{mf}}{\pi t_m}\right)^{\frac{1}{2}} \quad (26)$$

$$\mathrm{D_{tr}} = \left(\frac{R^2}{Pe_{mf} t_m}\right) \quad (27)$$

Where C_t is the transfer function which corresponds to the overall concentration from each fracture, C_r. R_i is the apparent fracture length, u_i is the velocity and Pe_i is the Peclet number for the ith flow channel, Q is the volume production rate, R is the distance between the injector and producer, t_m is the mean arrival time, J is a model parameter, $\mathrm{D_{tr}}$ is the Taylor dispersion and m is the mass of tracer entering the stream tube.

2.4.2 Fracture-Matrix Model (Bullivant and O'Sullivan, 1989)

The fracture-matrix model developed by Bullivant O'Sullivan, 1989, describes the tracer transport along a single fracture including the fracture-matrix interaction. The tracer transfer can occur between the fracture and the matrix in both ways, however, longitudinal transport only occurs along the fracture and not through the matrix. Furthermore, the model ignores the longitudinal dispersion along the fracture channel.

$$C_r = JU(t - t_b)^{-\frac{1}{2}} \exp\left(\frac{-t_b}{w(t - t_b)}\right) \quad (28)$$

$$\mathrm{J} = \left(\frac{\mathrm{m}}{\mathrm{Q}}\right)\left(\frac{\mathrm{t_b}}{\pi w}\right)^{1/2} \quad (29)$$

Where U is the Heaviside step distribution, w is the ratio of transport along the fracture to transport out of the fracture, and t_b is the response start time.

2.4.3 Uniform Porous Model (Sauty 1980)

The uniform porous model, proposed by Sauty in 1980, addresses the hydro-dispersive transport of tracers in one-dimensional and two-dimensional systems, considering both continuous and instantaneous injection schemes. This model describes the mass transport between an injection well and an observation well, with the kinematic dispersion serving as the dominant component. Notably, the models developed for continuous and instantaneous injection schemes exhibit noteworthy differentiation when the Péclet numbers are below 10. The solution for the 1D instantaneous tracer injection is given by the following equations:

$$C_r = \frac{K}{\sqrt{t_r}} exp(\frac{-P_{e_{up}}}{4t_r}(1-t_r)^2) \quad (30)$$

$$K = \sqrt{t_{rm}} \exp\left(\frac{P_{e_{up}}}{4t_{rm}}(1-t_{rm})^2\right) \quad (31)$$

$$t_{rm} = \sqrt{1+{P_{e_{up}}}^{-2}} - {P_{e_{up}}}^{-1} \quad (32)$$

Where $P_{e_{up}}$ is the dimensionless Peclet number, t_r is the mean arrival time. Similarly, this model can be obtained in two-dimensional form as:

$$C_r = \frac{K}{t_r} exp(\frac{-P_{e_{up}}}{4t_r}(1-t_r)^2) \quad (33)$$

$$K = t_{rm} \exp\left(\frac{P_{e_{up}}}{4t_{rm}}(1-t_{rm})^2\right) \quad (34)$$

$$t_{rm} = \sqrt{1+4{P_{e_{up}}}^{-2}} - 2{P_{e_{up}}}^{-1} \quad (35)$$

CHAPTER 3

STATEMENT OF THE PROBLEM

This study aims to develop a thermo-hydrodynamical transport simulation by using the TOUGH2 reservoir simulator where the chemical reactions are neglected. To develop a resembling predictive model for the CO_2-charged brine injection in the Kızıldere field, a natural state simulation is needed to be constructed for obtaining the stabilized initial pressure and temperature values based on the static measurements of the observation wells. Once the initial conditions have been obtained, to understand the subsurface flow behavior, hydraulic parameters that govern the heat and mass transport must be determined by entailing multiple inter-well tracer tests. This goal can be achieved by treating chloride contents as a conservative tracer as well as two slug tracer tests conducted in the model boundary by matching the first arrival times, residence times, peak concentrations, and total recoveries. The subsequent model will be used to predict the long-term impact of the CO_2-charged brine injection whereas, hypothetical strategies needed to be examined under different injection scenarios with different durations and re-injection rates accompanied by constant rate and constant pressure conditions for the production wells to quantify the sequestration potential in the Kızıldere field.

CHAPTER 4

CHARACTERISTICS OF THE KIZILDERE GEOTHERMAL FIELD

4.1.1 General Overview of Kızıldere Geothermal Field

The Kızıldere geothermal field being Turkey's first discovered geothermal energy field, identified by the Directorate of Mineral Research and Exploration (MTA) is situated in the eastern part of the Büyük Menderes Graben, which lies between the Denizli and Aydın provinces (Figure 4-1). It is positioned between the Buldan and Babadağ Horsts and is located in the southern part of the Menderes Massifs, an extensive metamorphic massif in Turkey spanning approximately 300x200 km (Bozkurt and Oberhänsli, 2001). As of 2018, 3 geothermal power plants with more than 60 wells sum up to a total installed capacity of 260 MW, putting the field as one of the most significant geothermal sites in the globe.

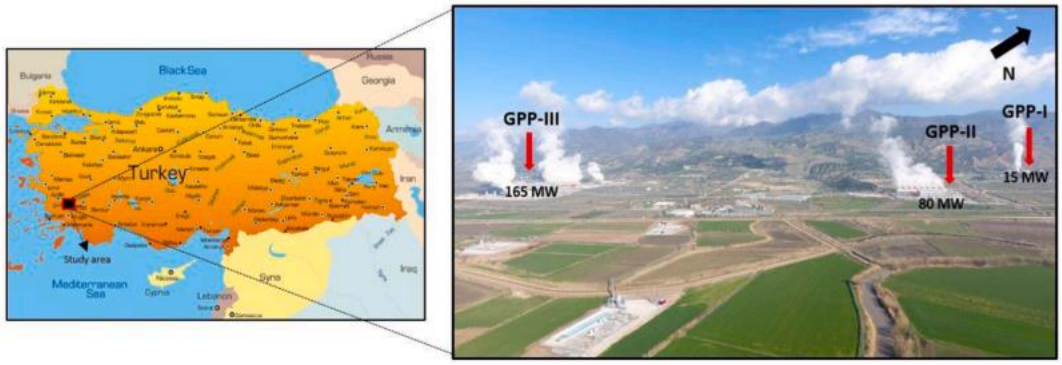

Figure 4-1 Location and operating power plants of Kızıldere geothermal field (Haklıdır et al., 2021)

Regarding the source of heat, no young volcanism was observed since the last volcanic eruption occurred approximately 12,000 years ago (Ercan, 1979). In the northern section of the Gediz Graben, the volcanic formations are relatively young while in the western portion of the Büyük Menderes Graben, the volcanic activity dates back to the Plio-Quaternary period (Şimşek, 1984). It should be noted that both

volcanic formations are closely associated with the rift system (Ercan, 1981). The heat flow map of the area demonstrates the presence of heat anomalies along the graben (Tezcan, 1979), suggesting the existence of a potential magmatic source. Şengör and Yılmaz (1981) proposed that the origin of this magmatic source could potentially be granite intrusions beneath the Menderes Massif. The predominant fault system in the region exhibits an E-W and SE-NW orientation, with some additional N-S trends. The prevailing faults are the E-W-oriented faults connected to the Büyük Menderes Graben (Şimşek, 2005).

4.1.2 Stratigraphy of the Kızıldere Geothermal Field

From the youngest formation to the oldest one, the stratigraphy of the Kızıldere field (Figure 4-2) consists of Pliocene and Quaternary sedimentary rock of the Tosunlar Formation, Kolonkaya Formation, Sazak Formation, Kızılburun Formation and the Paleozoic metamorphics of Menderes Massifs.

At the deepest section of the Pliocene section, the Kızılburun formation lies which consists of well-consolidated brownish conglomerates, sandstones, and claystones with a thickness of 300 meters. Due to its low permeability, it serves as a caprock formation between the Paleozoic metamorphics of the Menderes Massifs and the shallow reservoir section of the field named Sazak Formation consisting of limestone, siltstone, and marl belonging to the Pliocene period. Due to its karstic nature and brittle rheology, this formation serves as an excellent reservoir (Aksu, 2019) however, lateral and vertical gradation into marls and sandstones restricts the continuity of the reservoir (Küçük, 2018). A low permeability, thick formation (≈500m) that overlies the Sazak Formation named as Kolankaya Formation consists of well-consolidated conglomerates, sandstones, and clay stones which serve as a caprock for the shallow reservoir section. The top section of the geothermal system is covered by the Quarternary aged alluvium and alluvial fans overlying the Tosunlar Formation which forms the upper unit of Pliocene and Quarternary sedimentary rock

consisting of poorly consolidated conglomerate, sandstone, and mudstone with fossiliferous clayey limestone (Şimşek, 1985).

Below the Quarternary and Pliocene sedimentary formations, Paleozoic-aged metamorphic rocks form the basement of the Menderes metamorphics appearing at a depth of approximately 1400 meters which is the deeper reservoir section of the Kızıldere field (Şimşek et al., 2009). As the intermediate marble reservoir, the İğdecik Formation forms the upper section of the Menderes metamorphics composed of marble-quartzite-schists. High-temperature values, up to 212 °C, were observed compared to the shallow reservoir section (Şimşek, 1985b). The deep reservoir section in the Menderes metamorphics is composed of metamorphic schist and marble where temperatures as high as 236.5 °C were observed.

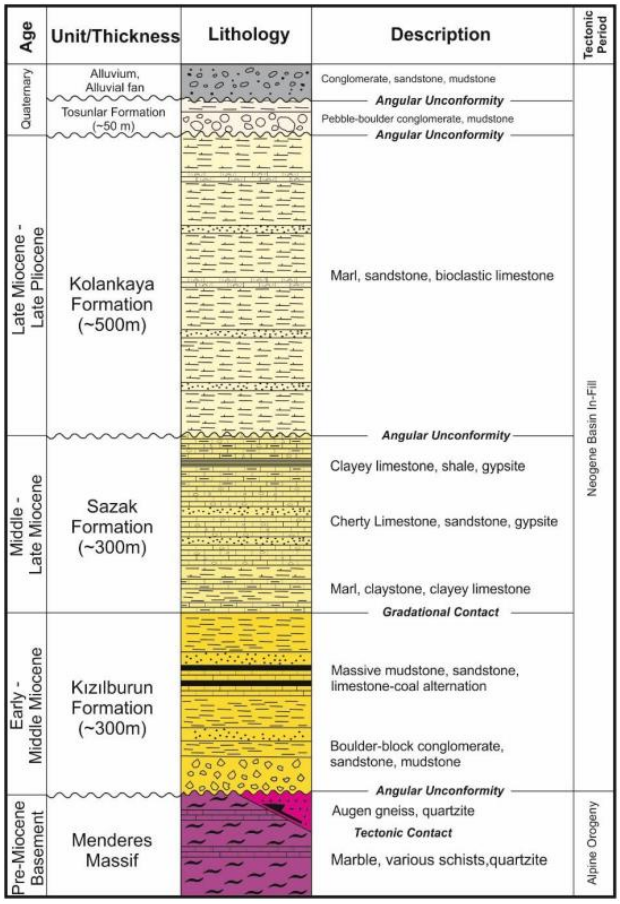

Figure 4-2 Stratigraphy of the Kızıldere geothermal field (Aksu, 2019)

For the overall reservoir comparison between the İğdecik Formation and the deep metamorphic reservoir, Karamenderesi (2013) stated that the deep reservoir section was found to be a good reservoir section but in terms of re-injection implementations, the İğdecik reservoir is much more suitable since it possesses high enough permeability for re-injecting the effluent water.

4.1.3 Conceptual Model of the Kızıldere Geothermal Field

According to the previously conducted gravity, resistivity, seismic, and gradient surveys and surface manifestations such as natural steam vents and several hot springs, Şimşek et al. (2009) developed a conceptual model of the Kızıldere Geothermal Field (Figure 4-3).

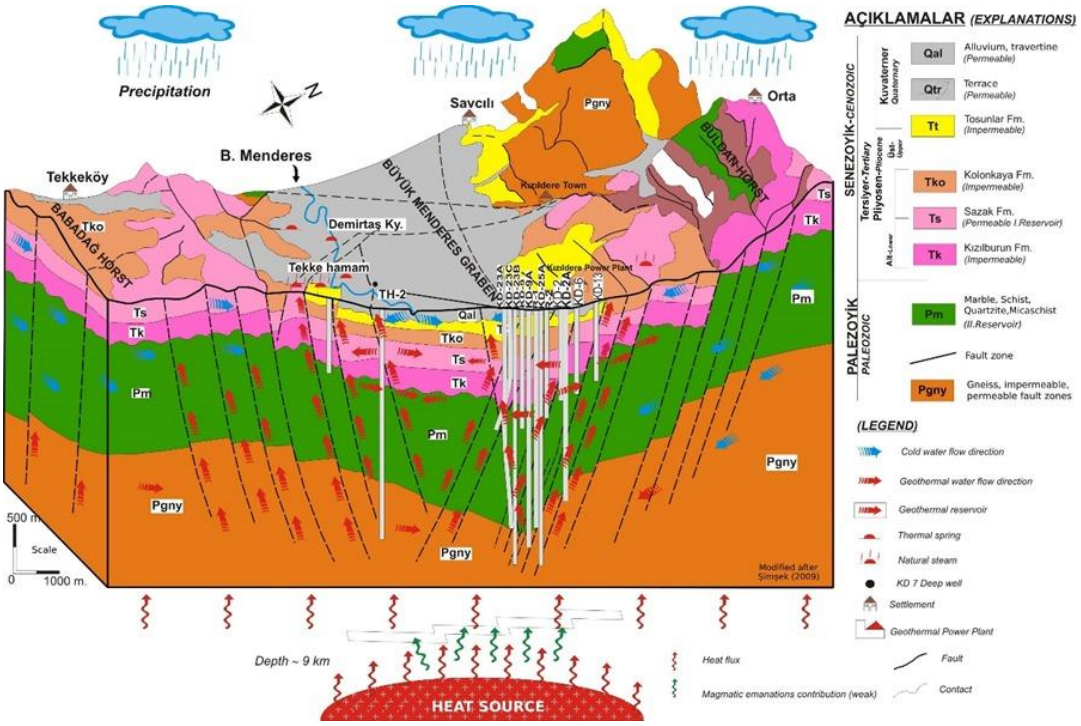

Figure 4-3 Conceptual Model of the Kızıldere Geothermal Field (Şimşek et al., 2009)

According to the conceptual model, the geothermal fluid has a meteoric origin, which is transported into the reservoir through conductive channels formed by the surface

outcrops of the faults. The increase in the temperature of the water due to high temperature with the increasing depth, the precipitated water heats up resulting in a density-driven convective flow due to the alteration in its density. The water rises upwards in the reservoir until it meets with an impermeable formation, however, it finds its way to the surface if the flow direction meets with a thermal spring or a natural steam vent. Furthermore, a heat source due to granitic intrusions has been placed at the lower section of the conceptual model to represent the thermal flux that feeds the geothermal system.

CHAPTER 5

RESERVOIR MODELING

The scope of this study is to develop a 3D sector non-isothermal reservoir model through the vast majority of data sources to predict the impact of the CO_2-charged brine injection from the pilot injection well KD-50A. The development of this model was divided into 4 parts which are demonstrated in a workflow scheme given in Figure 5-1. Firstly, based on the conceptual model provided by Şimşek (2009), a 3D sector model was constructed centering the pilot injection well including the nearby re-injection and observation wells. Furthermore, although the construction of a grid system is an iterative process throughout the study, the finalized version of the grid system will be provided in this stage. Secondly, as the first stage of the model calibration, based on the constructed sector model, a natural state simulation model has been calibrated for the available static measurements both for pressure and temperature taken from the wells within the model boundary. The natural state model has run for some time (eg. 150,000 years) until the convergence for pressure and temperature has been reached for all grid blocks representing the wells. In the third stage, a comprehensive dynamic calibration for the characterization of the injection site through the successive history matching of dynamic observations and inter-well tracer tests, which includes

- Chloride concentration measurements assuming it is a non-reactive, conservative species.
- A slug tracer test of 200 kg 1-naphthalene-sulphonate from KD-93B.
- A slug tracer test of 200 kg 2-6-naphthalene-disulphonate from the pilot injection well, KD-50A.

Finally, the developed model was used to simulate the CO_2-brine injection pilot where 985 tons of CO_2 has been injected over the course of 6 months. Furthermore,

to observe the impact and the storage potential of the Kızıldere field, different injection strategies, which differ in injection rate, injection duration, and different production assumptions including constant rate and constant pressure were analyzed accordingly.

The transport model is constructed in a non-isothermal, non-reactive fashion using the TOUGH2 simulator with the EOS1 equation-of-state module.

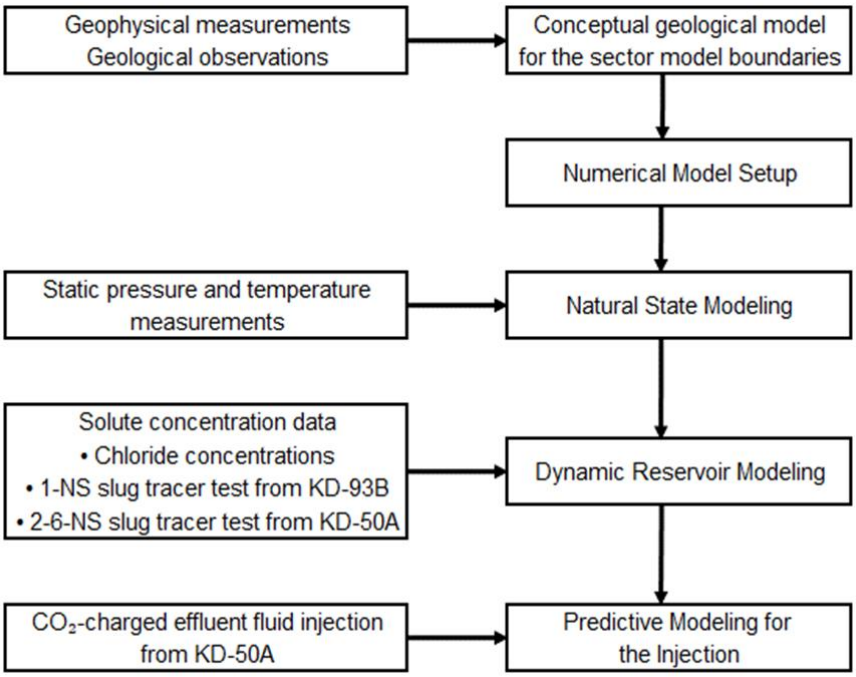

Figure 5-1 Workflow

5.1 Model Development

5.1.1 3D Sector Model

In the Kızıldere geothermal field, a 3D field-scale conceptual model (Figure 5-2) including the stratigraphic horizons and units has been constructed through the seismic data, mud loss data, and the well logs gathered from more than 60 wells (GECO, 2020; Erol et al., 2022).

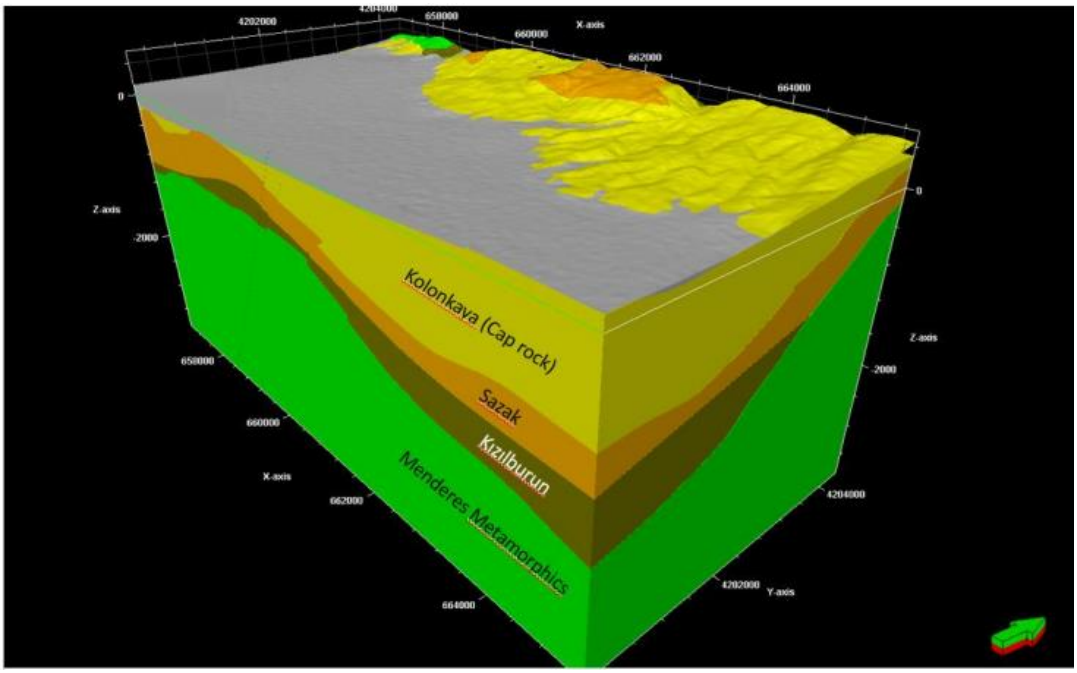

Figure 5-2 3D Geological model of the Kızıldere geothermal field (GECO, 2020).

On the other hand, calibrating multiple inter-well tracer tests demand a high number of simulations to reach a satisfactory match where the large-scale model of the Kızıldere field covers an areal extent of nearly 200 km^2. Thus, it demands a high computational burden, especially with single processor simulators such as TOUGH2 v2.0. Subsequently, a localized sector model strategy centralized around the pilot injection well has been developed (GECO 2020; Erol et al., 2022; Erol et al. 2022; Sevindik et al., 2023; Erol et al., 2023) both for reducing the computational time and obtaining increased accuracy near the pilot injection well.

The model boundaries of the developed sector model (Figure 5-3) cover an area of 5.18 km^2 with a depth of 3850 meters which lies in the central region of the field-scale model roughly. During model construction, the coordinates of the formation boundaries that intersect with the sector model region (Figure 5-4) have been determined as well as the fault zones accordingly.

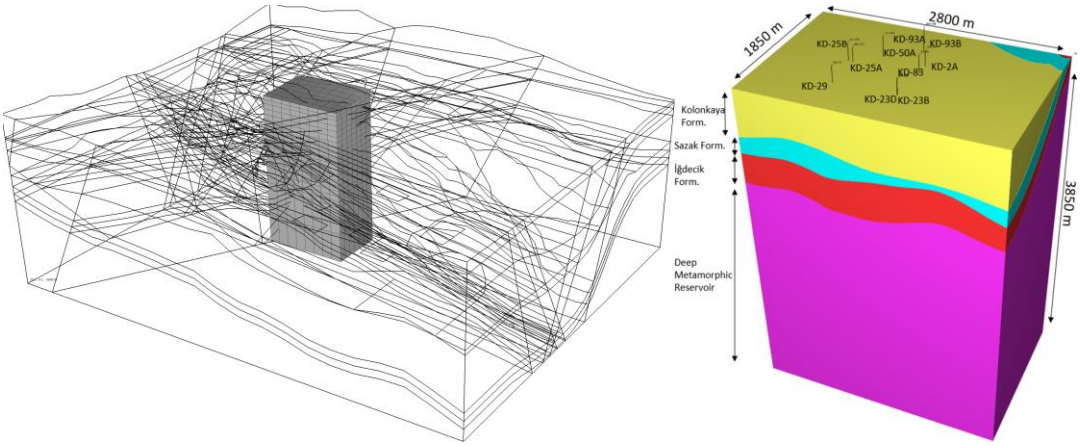

Figure 5-3 Sector model for the re-injection site. On the right view, the field-scale model and the sector model boundaries, and on the left view the geological model of the sector model.

The sector model covers a total of 10 wells. Out of these 10 wells, 6 are used for brine production and 4 are used for effluent fluid re-injection, including the pilot injection well. Note that each well located in the sector model either produces from or injects into the Menderes metamorphics (Figure 5-4). The observed formation thicknesses of the wells as well as the completion intervals included in the sector model are listed in Table 5-1.

Table 5-1 Formation thicknesses of the wells.

Well	Completion, m	Alluvium	Kolankaya	Sazak	Kızılburun	İğdecik	Menderes
KD-2A$_{pro}$	1568-1731	--	545	219	174	330	640
KD-23B$_{pro}$	1571-2525	10	662	240	145	305	1345
KD-23D$_{pro}$	1811-2313	15	654	256	155	390	1030
KD-25A$_{inj}$	1559-2517	10	465	447	148	452	1180
KD-25B$_{pro}$	2379-2844	90	495	320	175	-	2006
KD-29$_{pro}$	1718-2882	160	485	287	243	435	1424
KD-50A$_{inj}$	1615-2392	35	452	405	80	440	1476
KD-83$_{pro}$	1828-1956	25	525	225	225	-	2250
KD-93A$_{inj}$	835-1364	12	377	165	220	-	820
KD-93B$_{inj}$	835-972	14	383	173	109	-	487

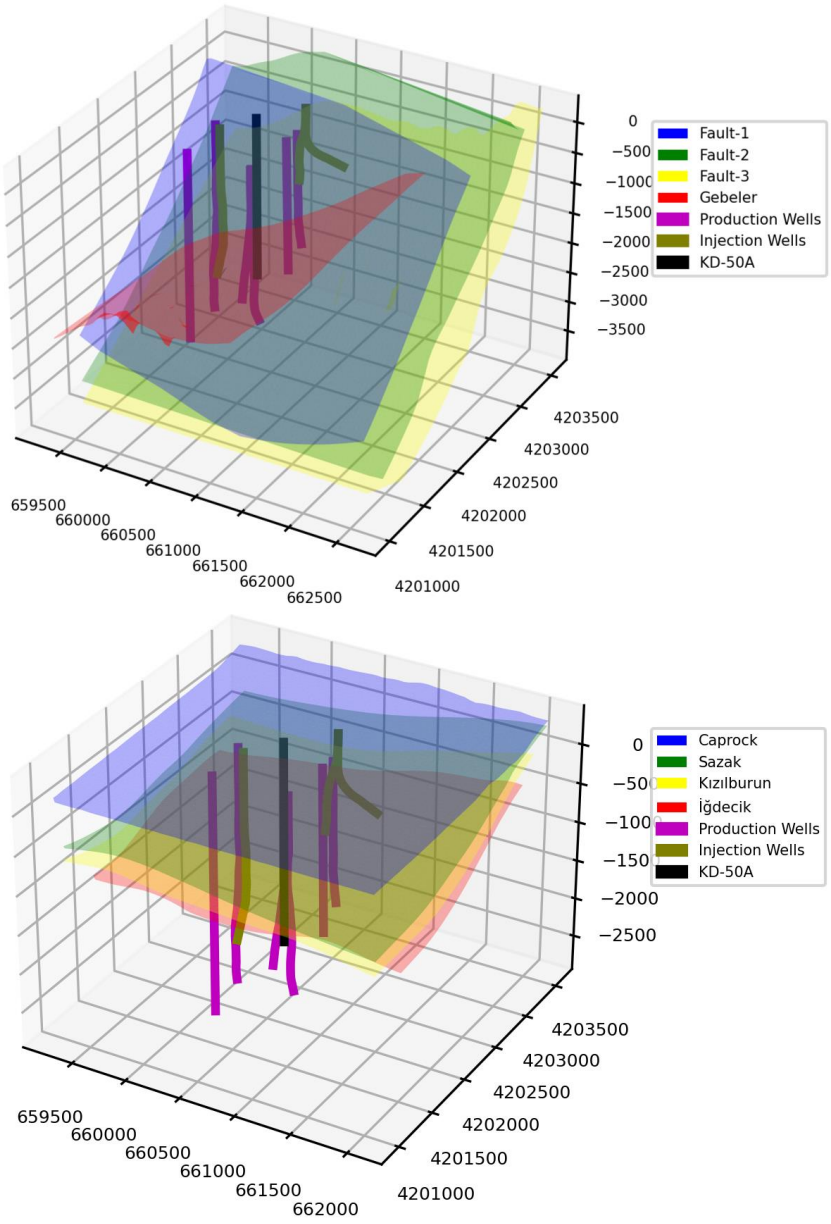

Figure 5-4 Top sections of the formation boundaries in the sector model with the wells (bottom), orientations of the faults in the sector model with the wells (top).

Alongside the major, SE-NW oriented fault called the Gebeler, 3 minor faults have been retrieved with N-S orientation from the field-scale model to the sector model. The majority of the completion intervals of the wells are intersected with the Gebeler fault and the Fault-2 thus, those faults are expected to be the main flow conduits between the injection and the production wells in the sector model. The orientation of those faults alongside the well locations is expressed in Figure 5-4.

Finally, using the aforementioned information regarding the geological settings and well locations, the 3D geological sector model has been constructed via Petrasim. Figure 5-5, represents the geological formation boundaries, regions, and fault orientations within the sector model region alongside the production and re-injection wells.

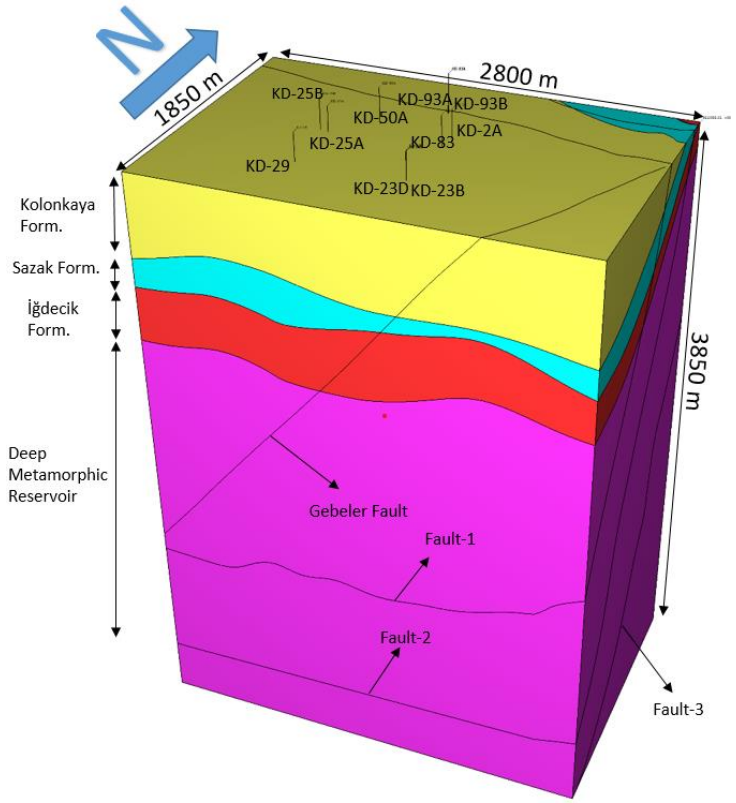

Figure 5-5 Finalized 3D Geological Model of the sector model region with formation boundaries, fault zones, and wells via Petrasim

5.1.2 Gridding of the 3D Sector Model

Prior to assigning initial conditions to the model, it is crucial to establish a suitable grid system by subdividing the geological model into smaller representative elementary volumes, or grid blocks. Determining the grid system of a numerical model is an iterative process that involves capturing not only the spatial variations of pressure, temperature, and species saturations in the geothermal system but also

the spatial dependence of heterogeneous model parameters, such as permeability and porosity. Typically, a more refined model incorporating a larger number of grid blocks allows for a more precise representation of these spatial variations and heterogeneities. Nevertheless, it is important to bear in mind that using a finer model demands greater computational power resulting in higher simulation times which limits the grid size selection.

In TOUGH2 v2.0, the space discretization of the conservation equations using the Integral Finite Difference method enables to construct grid blocks on any spatial system including rectangular, polygonal, and radial grid blocks as long as certain criteria are satisfied as discussed in Chapter 2.3.

During the grid generation for the 3D Sector model (Figure 5-5), the Voronoi tesselation method has been applied to generate polygonal grid blocks. Those polygonal cells which are generated by Petrasim, create the grid blocks in such a way that the interfaces between the adjacent elements are the perpendicular bisectors of the line between two points. The vertices of the elements are formed at the intersections of these bisectors. The shape of each element is determined by the points that are closest to its center point.

The parameters that control the Voronoi mesh are the maximum cell area, minimum refinement angle, and the maximum area near the wells. Furthermore, additional refinements can be made by two-dimensional coordinate input and the cell area of the location that needed to be refined. For the gridding strategy that has been applied to the sector model, it is important to capture the transient responses in the vicinity of the wells whereas, the grid blocks are desired to get larger along the distance between the wells and the model boundary. Additionally, at a particular depth, the intersection of a well with multiple grid blocks can cause convergence problems thus, the mesh parameters should be controlled accordingly. In Table 5-2, the Voronoi mesh parameters that have been taken as inputs for the grid generation are expressed respectively. In terms of the additional refinements that have been implemented, 10 additional two-dimensional coordinates have been used with an

area of 1000 m^2. The need for defining additional points for the polygonal grid arises due to the fact that during dynamic simulations, matching the tracer tests demands high resolution for the calibration of model parameters. The coordinates of those refinements have been determined iteratively during the dynamic simulations and they do help to increase the number of grid blocks along the possible flow paths (Figure 5.-7b) between the re-injection wells and the production wells. Consequently, in a single layer, there are 611 polygonal grid blocks have been generated (Figure 5-6).

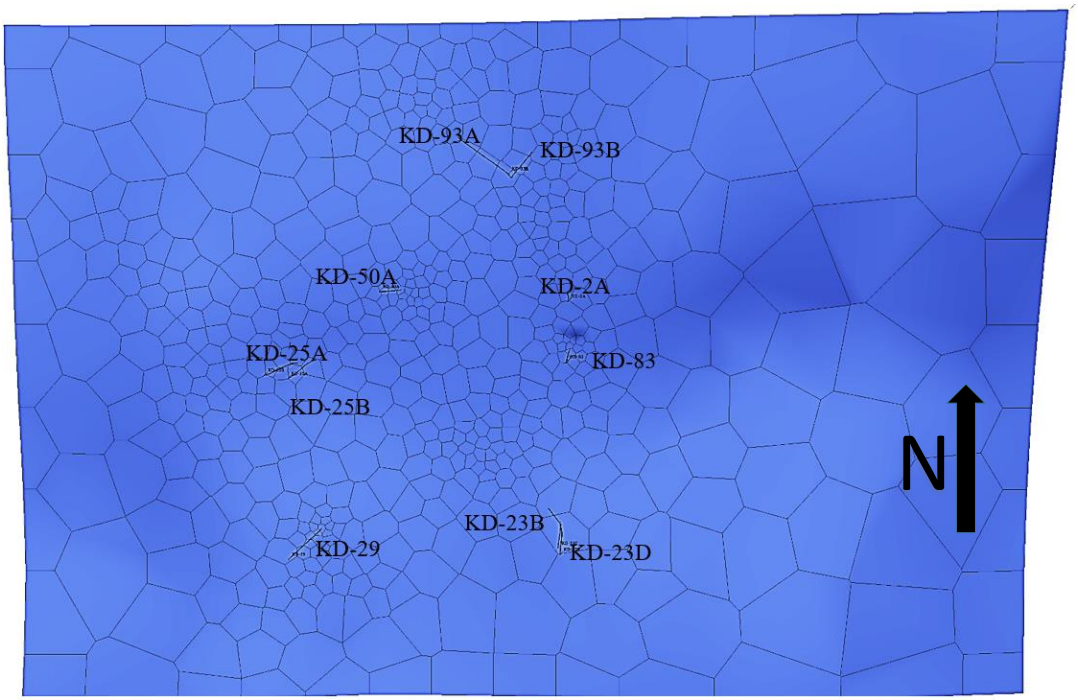

5-6 Distribution of polygonal grid blocks in a single layer

Table 5-2 Parameters used in the Voronoi grid

Maximum Cell Area	50000 m^2
Minimum Refinement Angle	30.0°
Maximum Area near Wells	300 m^2
Additional Refinements	10 points, 1000 m^2

In Voronoi gridding, the vertical alignment of the grid blocks is arranged as the successive grid blocks in the vertical direction have identical top or bottom areas however, depending on the thickness of the layers, the heights of the three-dimensional polygons may vary.

In the 3D sector model, from top to bottom, there are mainly 4 enclosed regions between the geological boundaries. The first enclosed region is between the Kolankaya Formation and the Sazak Formation, the second one is between the Sazak and the Kızılburun Formations. Thirdly, between the Kızılburun Formation and the İğdecik Formation. The last enclosed region is from the İğdecik formation to the bottom boundary of the model.

Table 5-3 Distribution of grid blocks along the vertical section

Region	*Number of Layers*	*Total Fraction that the Grids Cover*
Kolankaya - Sazak	3	1
Sazak – Kızılburun	3	1
Kızılburun - İğdecik	3	1
İğdecik	2	0.08
-	5	0.06
3850 m BSML	28	0.56
(Reservoir Section)	3	0.3
Total	47	

For the regions that overlie the İğdecik Formation, 3 layers have been assigned to each of them since the thickness of those regions is relatively narrow compared to the reservoir section as well as no completions are intersected with those regions. Since, the entry levels of the completions intervals for each well in the sector model are in the deep metamorphic reservoir whereas, the deepest well in the model is KD-29 at a depth of 2882 BSML, this depth interval has been divided into thinner layers with 4 distinct subregions. Table 5-3 summarizes the grid size distribution along the vertical section of the model area.

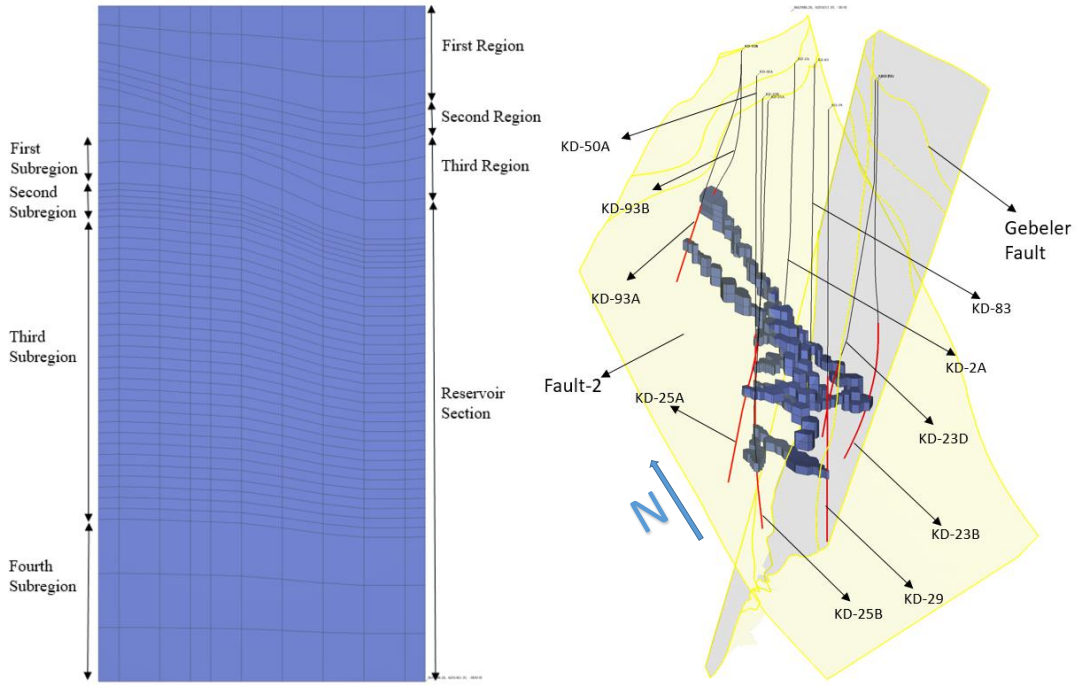

Figure 5-7 Vertical layering of the grid blocks.

In the reservoir section, the first subregion (Figure 5-7, right-panel) which corresponds to the 0.08 of the reservoir section has been divided into 2 layers since the only well intersecting with the deeper interval of this section is KD-93A. The underlying section comprises the thinnest grid blocks, corresponding to the well KD-93B. This particular well, with a narrow completion depth of approximately 140 meters, was utilized for a slug tracer injection test. Therefore, it is essential to maintain a high resolution to accurately capture the detailed characteristics of this narrow interval. From this region to the bottom of the deepest well KD-29 (2882 BSML), 28 layers have been generated covering 56% of the reservoir section. Finally, the last 30% of the reservoir section has been divided into 3 layers as there are no well completions coinciding with this region thus, lower resolution is satisfactory. Figure 5-7 illustrates the vertical distribution of grid blocks based on the aforementioned information. Subsequently, 27495 grid blocks have been generated for the 3D sector model for further numerical simulation purposes.

5.2 Natural State Modeling

In the natural state modeling, the aim is to determine the initial (undisturbed) reservoir conditions in terms of pressure and temperature distributions by calibrating the sensitive model parameters including the initial gradients for pressure and temperature, permeability, porosity, and the specific heat of the formations through matching the available static pressure and temperature measurements taken from the wells until a satisfactory agreement is achieved.

Furthermore, to ensure that the model has reached the natural state conditions, the simulation time must be sufficiently long to achieve the convergence (stabilization) of the model outputs. In this study, the settings for the convergence are 1 °C/10,000 years and 1 bar/10,000 years respectively.

Prior to the beginning of the natural state simulation, the initial distribution of parameters including permeability and porosity for the formations and the rocks, initial gradients for both pressure and temperature across the grid blocks, boundary conditions, and the necessary sources/sinks must be identified. Further in the calibration of the natural state model, those parameters would be iteratively adjusted to reach the agreement between the simulation outputs and the measurements respectively. In this study, the tolerance for the model outputs and the static measurements is matching them in a 10% confidence interval through the completions depths of each observation well respectively. In that manner, the following steps are applied during the natural state modeling.

1. Set the initial rock parameters, gradients, boundary conditions, and the sources/sinks.
2. Run the model for 150,000 years.
3. Check whether the model convergence has been reached, if not, check the model parameters and run the model for a longer duration.

4. Check whether the model outputs have a satisfactory agreement with the measurements. If yes, proceed to the dynamic simulation else, return to the first step.

5.2.1 Initial Rock Properties

The initial permeability and porosity values for the formations and the fault zones have been taken from the existing sensitivity analysis for the rock properties and well tests in the Kızıldere field (Küçük, 2018, GECO, 2020) prior to the calibration.

Initially, 8 distinct rock materials have been introduced to the model representing each formation and fault. The model contains 2 caprock formations including the Kolonkaya formation with the alluvial deposits and the Kızılburun formation thus, relatively low permeability values have been assigned accordingly. For the fault zones, the Gebeler Fault is known to be the major carrier fault compared to the N-S oriented faults hence, the permeability value used for the Gebeler Fault is slightly larger than the other faults in the sector model boundary (Figure 5-8).

Table 5-4 Materials and assigned rock properties.

Material	*Porosity (%)*	*Permeability (m^2)*
Caprock	3	$5* 10^{-17}$ - $1* 10^{-16}$
Alluvial	3	$1* 10^{-16}$
Sazak	4	$7* 10^{-14}$ - $2* 10^{-15}$
Metamorphics	1-4	$1* 10^{-15}$ - $1* 10^{-14}$
Gebeler Fault	1-4	$7* 10^{-14}$
Fault-1	4	$2* 10^{-15}$
Fault-2	1-4	$1* 10^{-15}$- $7* 10^{-14}$
Fault-3	4	$2* 10^{-15}$

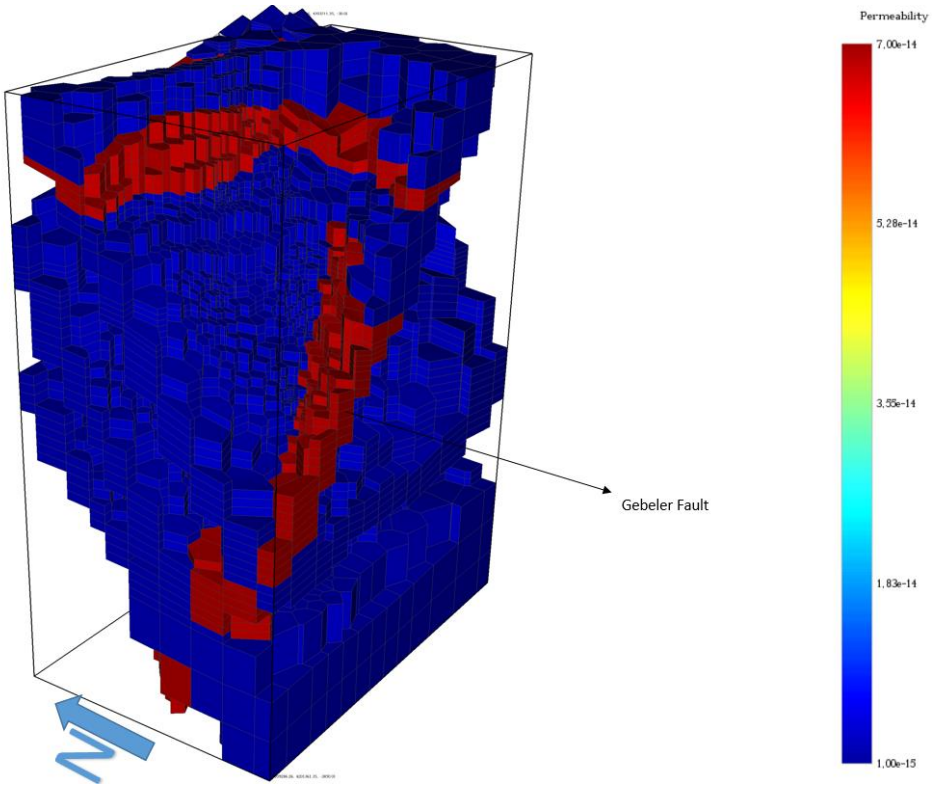

Figure 5-8 Initial permeability distribution along the faults.

Furthermore, porosity values in the model are taken between 1% and 4% for which during natural state simulations, higher porosity values yielded a slight increase in the temperature distribution in some locations. This occurs due to the fact that there exists a reciprocal proportion between the bulk thermal conductivity and porosity. As the porosity values increase, the decreased bulk thermal conductivity results in a lower rate of heat transfer across the deeper section of the reservoir model since the heat source is located at the bottom boundary. In addition, a more remarkable reason is that during dynamic simulations for slug tracer tests (see Chapter 5.3), high porosity values (> 5%) resulted in extremely late arrival times, which cannot be compensated by assigning unrealistically high values of permeability. The only compensation for increased values of porosity is incorporating a much more refined grid system, which would result in a decrease in the volume of each grid block subsequently, an increase in the flow velocity along the flow paths between the wells (Figure 5-7). However, the cost of this refinement would be huge thus, the obtained

results are considered to be representative porosity values for the sector model region. In terms of wet heat conductivity and the specific heat of the materials, 2.0 $W/(m*K)$ and 1000.0 $J/(kg*K)$ have been used respectively. The overall rock properties assigned for each material are summarized in Table 5-4.

5.2.2 Initial Conditions, Boundary Conditions, and Sources/Sinks

The determination of initial conditions for pressure and temperature is an important aspect of natural state modeling. This is because these initial conditions not only affect the final solution of the model (especially for closed systems), acting as calibration parameters but also impact the simulation time based on the accuracy of the initial guesses compared to the actual solution. During the natural state modeling, the following initial conditions have been used.

$$P = 7.515E5\ Pa - 0.08 * z\ bar/m \quad (36)$$

$$T = 5.0\ °C - 0.085 * z\ °C/m \quad (37)$$

Where z is the depth value with respect to the sea level. The following figures (Figure 5-9, Figure 5-10) illustrate the initial pressure and temperature values.

The grid blocks in the top layer of the first region (Figure 5-7) in the model have varying depths of -34 meters to -134 meters. This layer has been set to be a fixed-state boundary (Figure 5-11) for which no changes will occur throughout the simulation in terms of any thermodynamic properties. The aforementioned initial conditions for this layer in terms of temperature are between 27.88 °C and 36.41 °C which provides a cooling effect to the model as it is a similar case in the real systems where it is exerted by the cold rainwater intrusion. Moreover, the initial pressure values for this layer are between 23.7 bars and 31.77 bars. Furthermore, in TOUGH2 v2.0, the outer grid blocks in the model are considered to have no flow boundaries indicating no mass influx/outflux occurs within those cells unless a source or sink is placed.

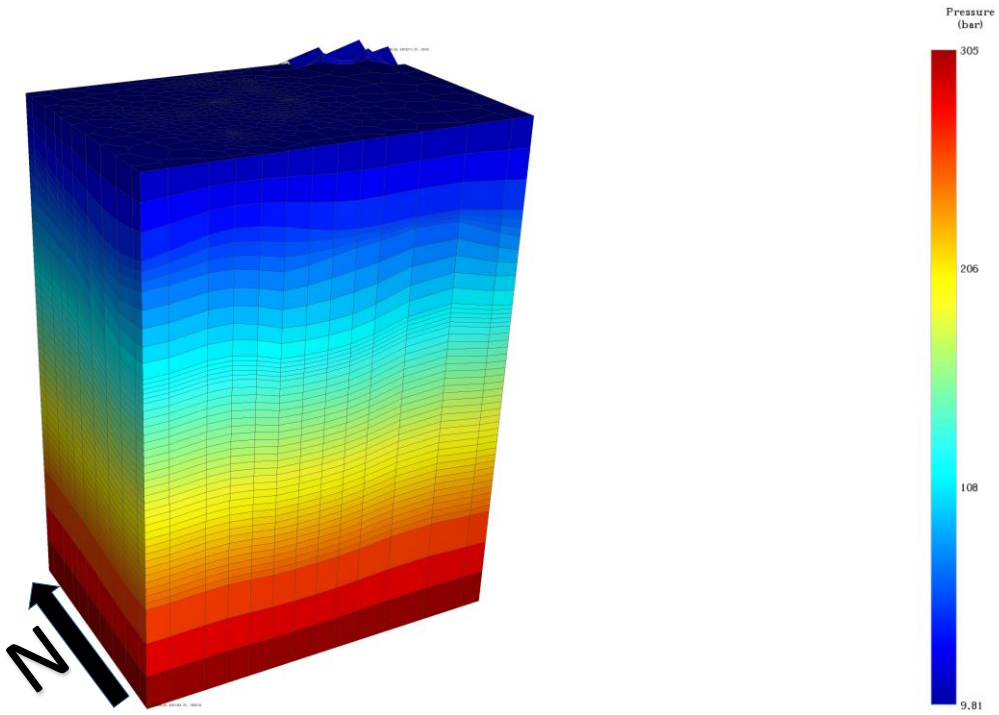

Figure 5-9 Initial pressure distribution.

Lastly, there are two heat sources introduced to the model in order to represent the heat influx and outflux from the system. The first heat source provides a conductive heat flux with a magnitude of 0.2 $J/(s * m^2)$ located at the deepest layer of the fourth sub-region (Figure 5-11), covering an area of 5.18 km^2 to imitate the thermal re-charge of the geothermal system. The second heat source is located in the upper section of the Kızılburun Formation at a depth of approximately 700 meters BSL which covers an area of 5.18 km^2 same as the first heat source (Figure 5-11). This heat source extracts heat from the system with a magnitude of 0.2 $J/(s * m^2)$, not only aiding the model to reach the stabilized conditions but also creating the observed geothermal gradient for the shallower sections of the geothermal system. Another reason why this heat source is placed is that in the Kızıldere geothermal field, although there exist production wells that extract geothermal fluid from the Sazak formation, there are no wells in the sector model boundary as such. Thus, this heat outflux mimics the heat extraction behavior of the surrounding wells outside of the sector model boundary.

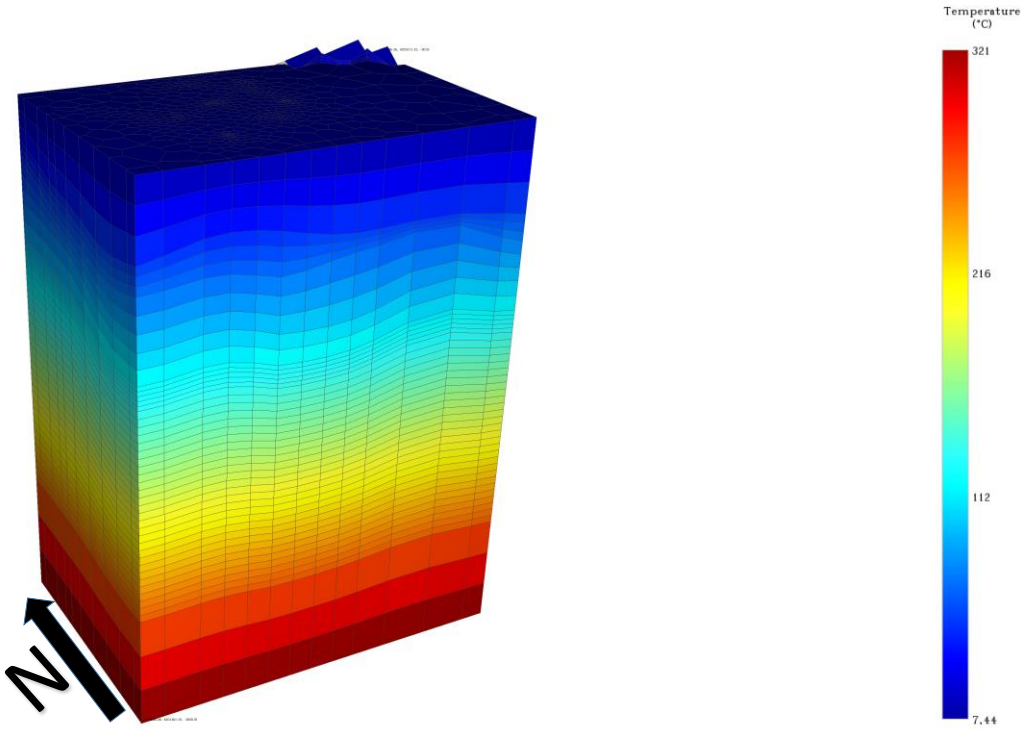

Figure 5-10 Initial temperature distribution.

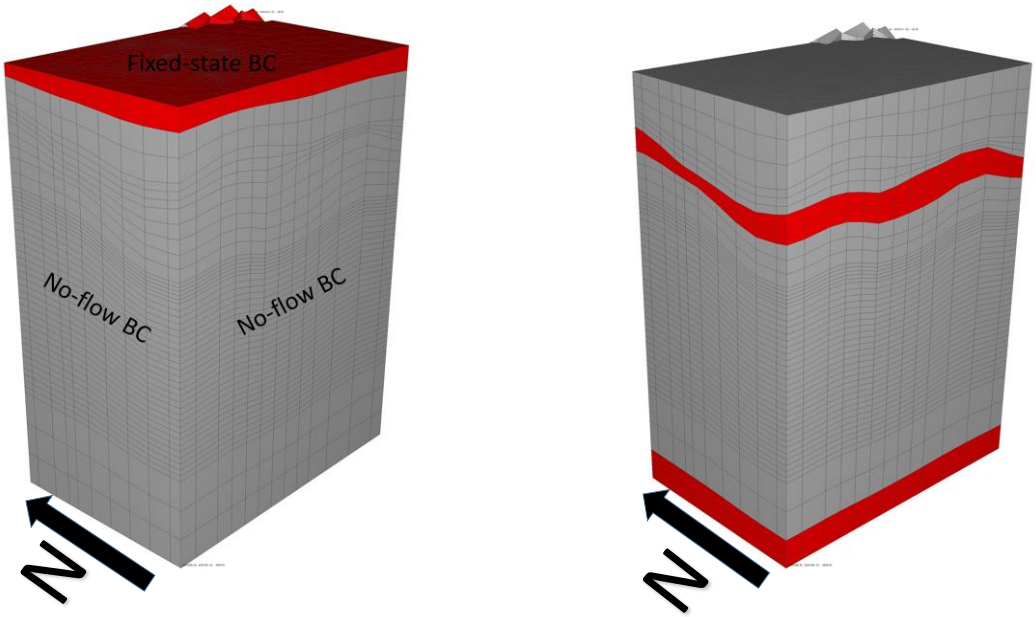

Figure 5-11 Fixed-state and no-flow boundary conditions (right panel), heat sources (left panel)

5.2.3 Results and Discussions of the Natural State Modeling

After the aforementioned parameters had been established, the model was simulated for a duration of 150,000 years, ensuring that the pressure and temperature values had reached a stabilized state. In the sector model region, comprising a total of 10 wells, the temperature has been measured at 6 of these wells, while pressure measurements have been obtained from 5 of them.

The pre-determined target of calibrating the measurements with the model output inside a 10% confidence interval has been mostly achieved along the completion intervals of the wells. Figure 5-12 displays the simulated and the measured pressure, on the other hand, Figure 5-13 presents the simulated and the measured temperature profiles along the completion depths respectively. Furthermore, as another benchmark to justify the goodness of the fit, the simulated and the measured static pressure and temperature values are plotted both at the production casing entry depths and at the bottom-holes of the wells respectively (Figure 5-14a and 5-14b). Lastly, numerical errors for the respective depths are shown in Table 5-5.

In terms of pressure profiles, a good agreement has been achieved between the modeling results and the static measurements. In the wells KD-2A, KD-23D, and KD-25A, a near-perfect match has been achieved. For the well KD-23B, the simulation slightly underestimated the actual pressure values whereas, in KD-50A, the opposite is true for which the model overestimated the actual pressure present in the geothermal system. A possible underlying reason as to why such a phenomenon occurs is that the caprocks including the Kolankaya Formation and Kızılburun Formation tilt upwards along the north of the site (Figure 5-4). As located at the southern and northern locations in the sector model, KD-23B and KD-50A, the tilting of the formations creates slight under-pressure and over-pressure zones due to being low porous and high-density natures.

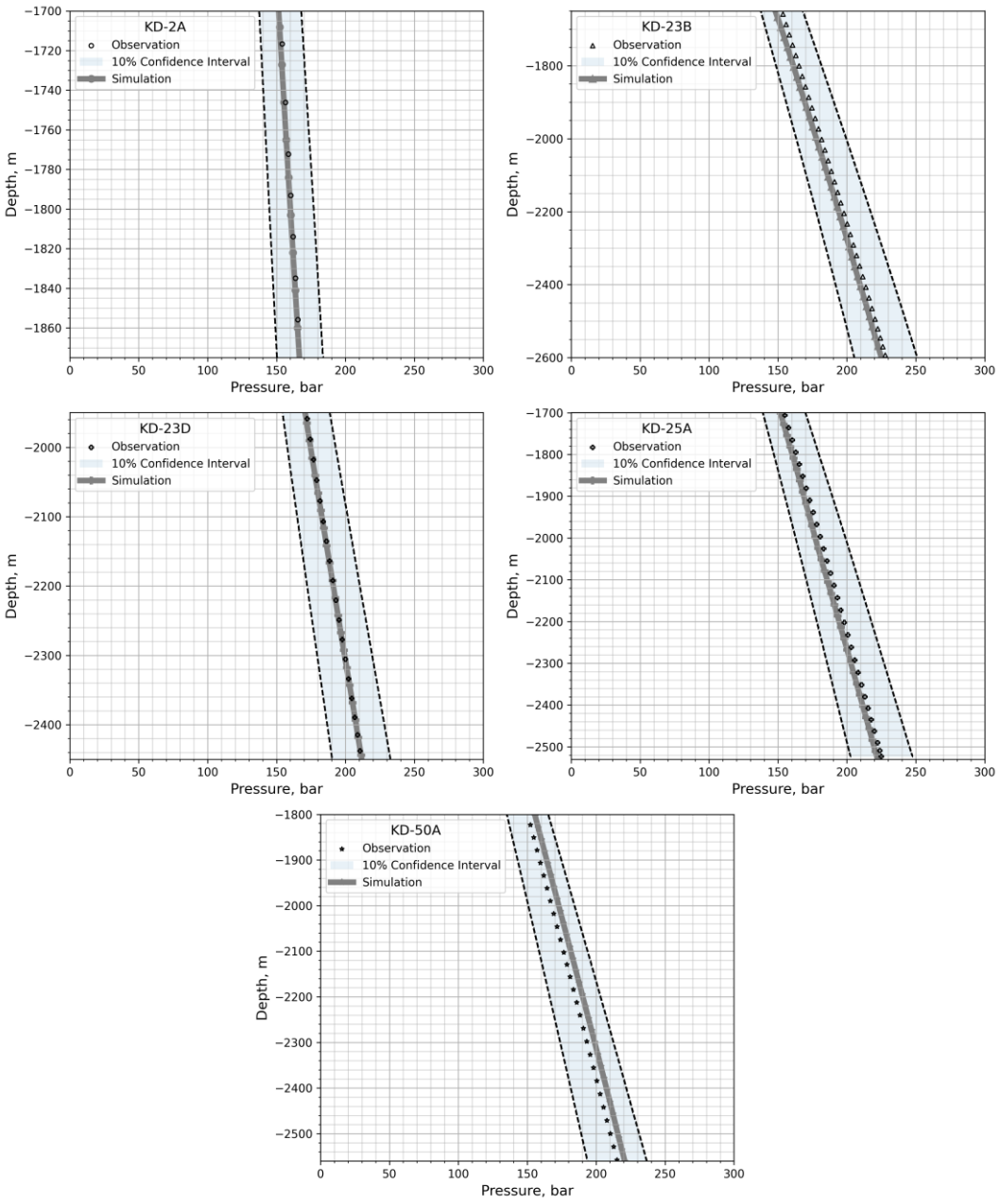

Figure 5-12 Resulting pressure profiles with the 10% confidence intervals.

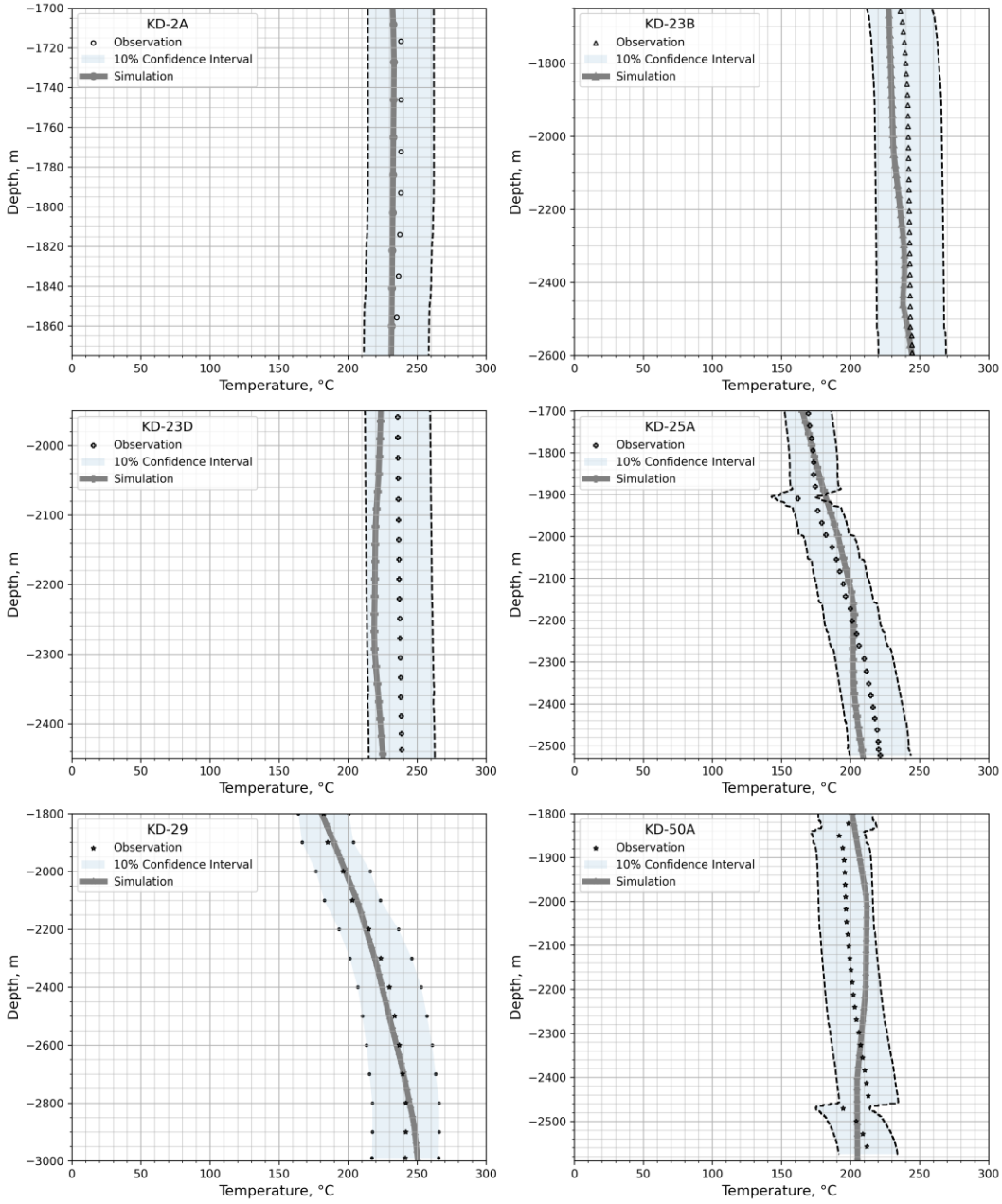

Figure 5-13 Resulting temperature profiles with the 10% confidence intervals.

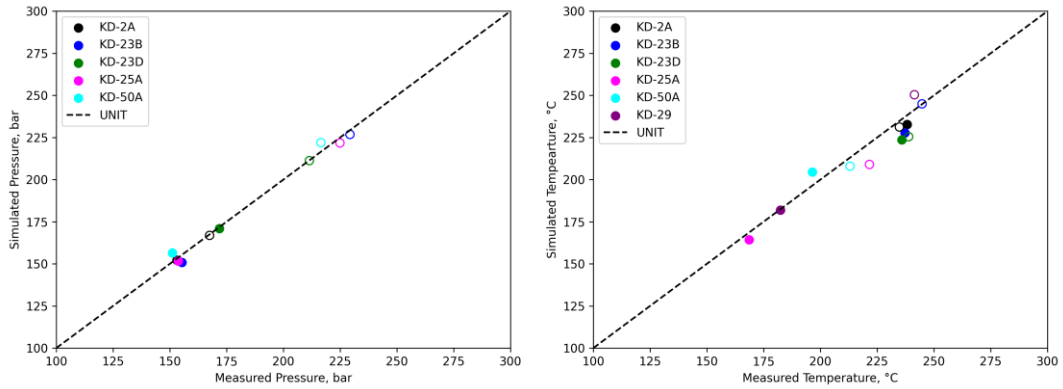

Figure 5-14 Simulated and Observed Pressure Comparison (on the right panel), Simulated and Observed Temperature Comparisons (left panel) at 9 5/8" casing entries and bottom-holes of the wells; Solid points 9 5/8" casing entries and hollow points represent bottom-hole values of the wells respectively.

In terms of temperature profiles (Figure 5-13), a fair agreement along the completion depths has been achieved in the wells KD-2A, KD-23B, KD-29, and the shallow sections of the completion interval of KD-25A. On the other hand, for the wells KD-50A and especially KD-23D, although the temperature profiles are in the range of 10% confidence intervals, the calibration results show comparatively poor results. Numerous factors contribute to the occurrence of these errors, the first among them being the overestimation of permeability values for the overlying sections of KD-23D. During model calibration, better results are obtained for the well by assigning lower permeability values for the overlying layers; however, without incorporating a more refined grid structure for the particular layers, the temperature profiles of the remaining observation wells are disturbed. The second reason is that the measurements taken from the wells do not resemble the undisturbed temperature conditions in the reservoir since, at the time the measurements were taken, some nearby wells were already operational, which can affect the pressure and temperature values. For instance, the static measurements of the KD-50A were taken while the other neighboring wells have been producing for over a year. Despite those reasons, the natural state model has fallen short in terms of matching the temperature profiles of KD-23D and KD-50A.

Table 5-5 Pressure and Temperature Errors, %.

Point Location	*Depths, m*	*Pressure Error, %*	*Temperature Error, %*
KD-2A Casing Entry	1704	0.63%	2.31%
KD-2A Bottomhole	1880	0.37%	1.52%
KD-23B Casing Entry	1679	2.87%	3.97%
KD-23B Bottomhole	2615	1.09%	0.08%
KD-23D Casing Entry	1953	0.48%	5.17%
KD-23D Bottomhole	2450	0.08%	5.61%
KD-25A Casing Entry	1691	1.23%	2.53%
KD-25A Bottomhole	2523	1.41%	5.69%
KD-50A Casing Entry	1810	3.56%	4.15%
KD-50A Bottomhole	2574	2.52%	2.37%
KD-29 Casing Entry	1812	No Measurement	0.20%
KD-29 Bottomhole	2990	No Measurement	3.72%
Average Error %		1.42%	3.11%

5.3 Dynamic Reservoir Modeling

After the natural state simulation has been concluded and consequently, the initial conditions of the model have been determined, the injection and production wells have been introduced to the model with their respective injection and production rates (Figure 5-15).

Although the Kızıldere geothermal field has been operated since 1984, the wells in the sector model region were commenced in late 2013. Thus, the dynamic reservoir simulation starts in February 2013, which is 6 months prior to the first well being commenced.

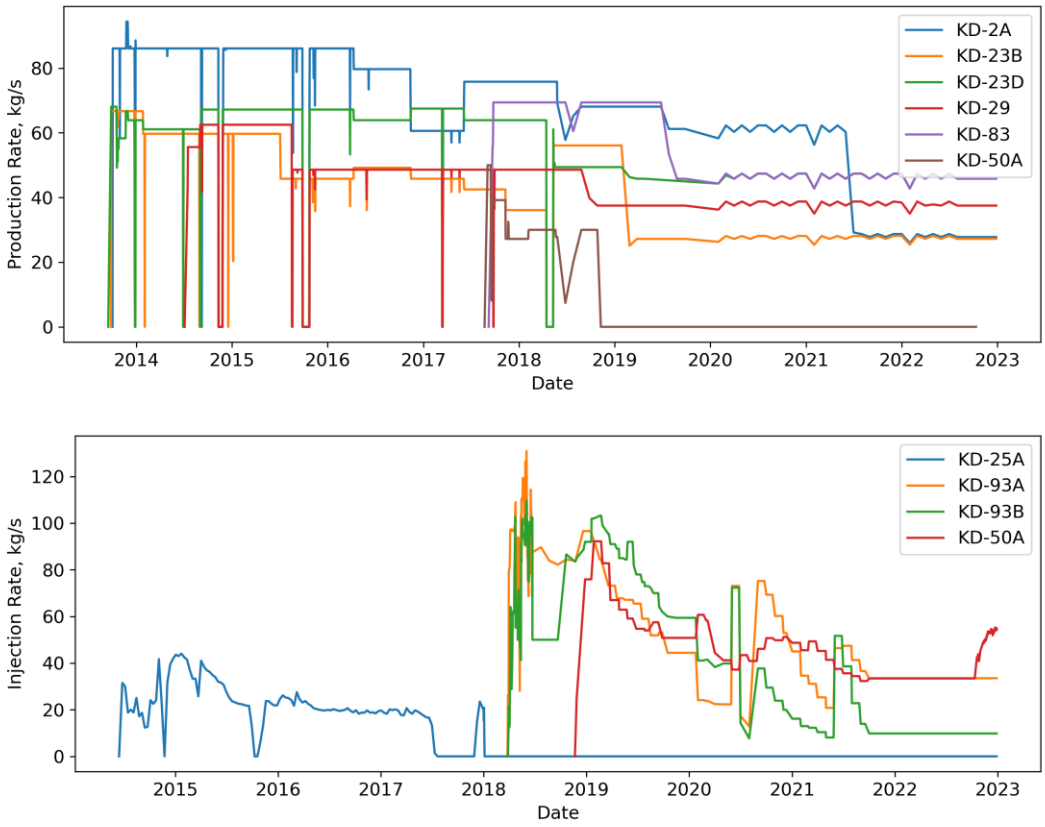

Figure 5-15 Production rates (top), and injection rates (bottom) for the wells in the sector model boundary.

The dynamic calibration of the sector model involves several procedures including the treatment of chloride circulation in the reservoir as a natural tracer, two slug naphthalene sulphonate tracer tests one from KD-93B, and another from KD-50A at different times. The respective calibration for each procedure is carried out by inverting the hydraulic parameters for the grid blocks of the flow paths (Figure 5-7) iteratively.

Furthermore, an important consideration is that the observed data may not resemble the production concentration in terms of tracer and CO_2 at a specific reservoir depth but the whole feed zone thickness of the production wells for which every well in the domain crosses through multiple grid blocks. By using a simple flow-averaging formula (Tomasdottir, 2018), the grid blocks of the production wells are calculated accordingly.

$$C_T = \frac{\sum_1^n C_i q_i}{q_T} \quad (38)$$

where,

C_T is the produced concentration from a well.

C_i is the produced concentration from a grid block intersected by a production well.

q_i is the mass flow rate from a grid block intersected by a production well.

q_T is the mass flow rate of a production well.

Thereafter, the calibrated model will be used to predict the impact of the CO_2 injection from the pilot injection well KD-50A. The timeline for the major tests and injection procedures conducted for the dynamic simulation are presented in Figure 5-16.

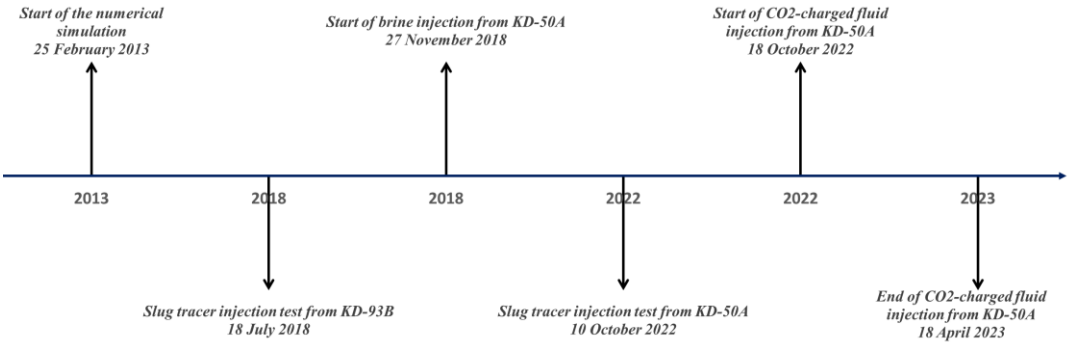

Figure 5-16 Timeline for the Dynamic Model

Aside from the calibration of the numerical model, analytical solutions presented in Chapter 2.4 are incorporated during slug tracer injection tests for determining the parameters including Peclet number and dispersivity which were used as benchmarks for the goodness of the fit of the calibration results.

For each analytical model, either the Nelder-Mead algorithm (Nelder and Mead, 1965) which is an unconstrained, derivative-free optimization algorithm, or SLSQP (Sequential Least SQuares Programming) is used for fitting the analytical models to the observations for determining the desired parameters. The optimized parameters

as well as the determined parameters for each analytical solution are expressed in Table 5-6.

Table 5-6 Optimized and determined parameters during analytical models.

Model	*Optimized Parameters*	*Determined Parameters*
Single Fracture	Pe, J, t_m	m, D_{tr}, u
Multi Fracture	Pe_i, J_i, t_{m_i}, e_i	m_i, D_{tr_i}, u_i
Fracture Matrix	w, t_b, J	m
1D Uniform	Pe, t_r	α, D_l, u

Furthermore, during the optimization of the observed data, a modified Cauchy loss function has been used as the loss function to deal with the outlier values. The Cauchy loss function is presented in the following equation.

$$C(y, \hat{y}) = \log\left(1 + \left(\frac{y - \hat{y}}{c}\right)^2\right) \quad (39)$$

where:

$C(y, \hat{y})$ is the Cauchy loss function.

y is the model value.

$\hat{y}$ is the predicted value.

c is the hyperparameter of the Cauchy loss function that controls the sensitivity to outliers.

The fitting of the analytical solutions is performed through a Python code presented in Appendix A.

5.3.1 Modeling Chloride as a Natural Tracer

Non-volatile chemical components such as chloride do not take part in any precipitation reaction in a geothermal system. This means that the concentration of

chloride in the reservoir fluid will remain constant over time, making it a useful tracer for studying fluid flow and mixing in the reservoir. Several simulation studies where conservative species have been used as tracers were conducted in the past. Kissling et al (1996) constructed a transport model where chloride was treated as a conservative, non-reacting species for the Wairakei geothermal field. Ratouis et al. (2022) used boron as a conservative species in the Husmuli geothermal field.

In Kızıldere Geothermal Field, although the reservoir fluid is water-dominated, a gradual enrichment of the chloride concentration occurs due to the pressure drop along the wellbores and separator units, which results in gas formation with boiling and adiabatic cooling. The enriched fluid is reinjected into the reservoir hence, continuous injection breakthrough curves are formed in the production wells in terms of chloride concentration, which enables us to define the flow path characteristics.

The chloride concentration from the production wells was continuously measured at surface conditions. The surface measured concentration data was then adjusted to the reservoir conditions for model comparison. One major consideration is that the initial distribution of the chloride concentration in the reservoir varies across regions at the reservoir conditions due to density-driven convective flows and the surface manifestations related to the precipitation. Furthermore, another reason for this variation of concentration is that although the dynamic simulation in this study starts nearly 6 months before the first well is taken into operation, there may exist a small degree of connectivity between the older injection or production wells outside of the sector model boundaries, which may dilute or enrich the chloride concentration of the reservoir section in the sector model region. The modeling of regional variations in the initial chloride concentration raises convergence problems in the natural state modeling thus, to simplify this issue, the initial concentration of the chloride has been taken as a constant value for the whole reservoir determined by the average initial concentration of the production wells as 95 ppm and the observation data has been normalized around the initial concentration accordingly.

$$C_{normalized,i} = \frac{C_{reservoir,i} - C_{initial}}{C_{reservoir}} \quad (40)$$

where,

$C_{normalized,\,i}$ is the normalized concentration value used in the calibration.

$C_{reservoir,\,i}$ is the concentration observation adjusted to the reservoir condition.

$C_{reservoir}$ is the initial concentration observation from the production well.

$C_{initial}$ is the average initial concentration value of the production wells.

5.3.1.1 Modeling Results and Discussions

The calibration of the chloride concentration breakthrough curves aims to characterize the flow paths within the model in terms of the anisotropic permeabilities and porosity values beforehand since, characterization of naphthalene sulfonate tracer injection was not done from the pilot injection well, KD-50A, before the CO_2 injection.

Based on the water samplings at the surface conditions, the chloride has been introduced to the model from all of the injection wells as a second water component using the EOS1 module in TOUGH2 v2.0. Figure 5-17 represents the injection rates of chloride from each of the 4 injection wells respectively.

Figure 5-18 displays the calibration results of the chloride breakthrough curves for the 5 production wells in the sector model region. From the figure, it can be stated that the model captures both the magnitude and the behavior of chloride concentration change respectively.

According to the results obtained from the chloride breakthroughs, although it is difficult to detect individual hydraulic connectivities between the injectors and the producers and justify the correct values because the injection is simultaneously carried out from multiple injection wells that affect the total amount of the chloride

concentration measured in the production wells, it is possible to establish total connectivity between the injection and the production wells.

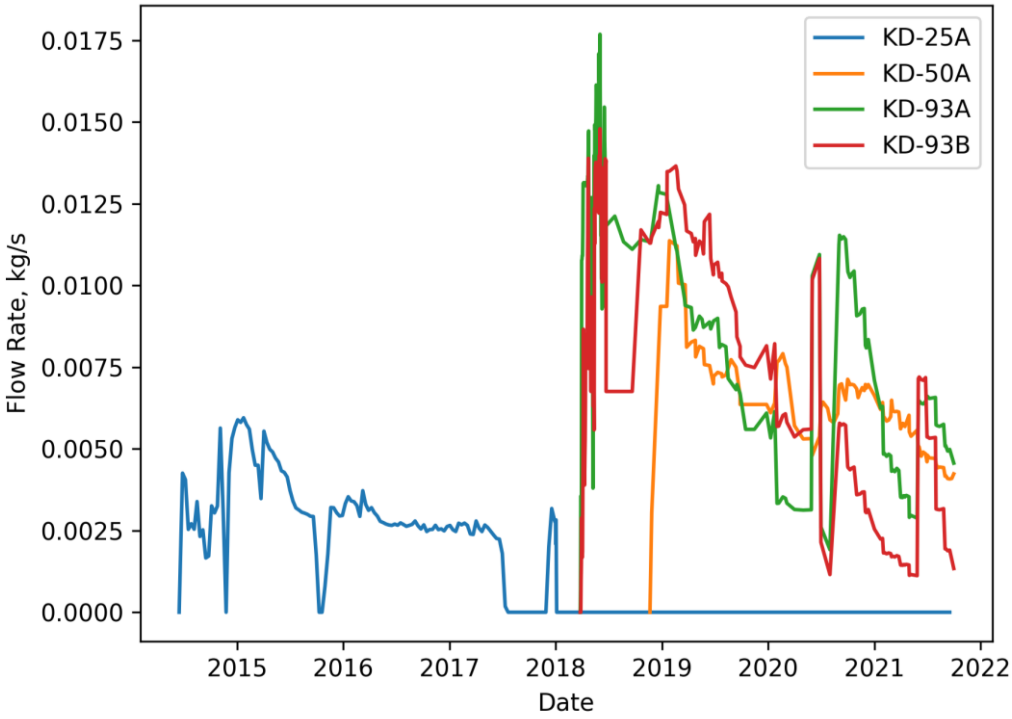

Figure 5-17 Chloride injection rates from the injection wells.

Both the calibrated model results and the observations suggest that the wells KD-2A, KD-23B, and KD-83 have a higher degree of hydraulic connectivity between the injection wells when compared to the remaining observation wells, KD-29 and KD-25B. There are several reasons for each production well to follow the above-mentioned result of having a higher or lower degree of hydraulic connectivity between the injectors. Firstly, a prior slug tracer injection test conducted from the well KD-93B (Erol, 2022, This Study) showed that most of the tracer was recovered from the KD-2A followed by the KD-83 and KD-23B. Thus the hydraulic connectivities would follow the same order. Furthermore, although there is no test conducted from the well KD-93A, it is located near the KD-93B, such that, the chloride present in the effluent fluid injected from KD-93A may follow similar flow paths similar to the KD-93B. Further enrichment of chloride contents in the wells can be explained by the flow paths existing between the well KD-50A and the

producers. During the dates covering the chloride sampling, no slug tracer test was conducted from the KD-50A; however, a later slug tracer injection test (GECO 2023, This Study) from KD-50A showed that the injected tracer has been recovered from all of the production wells resulting in a similar outcome in terms of the chloride concentrations at the production wells.

In terms of the well KD-2A, the observations indicated that the initial chloride concentration was around 94 ppm in 2019 and the concentration reached up to 108 ppm during the early months of 2021. The numerical model captures the concentration history well enough until 2021 when a smooth enrichment has been observed. A small overestimation has been observed by the model in the early 2021 concentration data. The main observed underlying reason for the particular occurrence is that, although the individual connectivity between the KD-93B and KD-2A is well established based on a calibration of a slug tracer injection test (see next chapter), there exists a little overestimation in the hydraulic connectivity of the flow path between KD-93A and KD-2A. Further in the model calibration, this overestimation has tried to be reduced and to be compensated by the other existing flow path between KD-50A and KD-2A; however, due to inherent uncertainties in the flow paths, this small overestimation is considered to be satisfactory.

In terms of the well KD-23B, a near-perfect calibration has been reached in terms of chloride concentrations, when compared to the other observation wells. The only significant connectivity of the KD-23B has been observed between the well KD-93B for which it is easier to set the overall communication between the wells.

In terms of the well KD-29, good calibration results have been observed until early 2021, when a slight underestimation has been reached in the model for the concentration history. It has been known that no hydraulic connectivity exists between the wells KD-29 and the injectors KD-93B and KD-25A according to the conducted slug tracer tests. In this regard, the hydraulic connectivity of the well between the injector KD-93A is uncertain. Although both wells align with each other in the direction of the N-S trending fault (Fault-2) the distance is too large between

the wells for which the model falls short in the later enrichment of the chloride. Perhaps, a small degree of connectivity exists between the well and an injector just outside the sector model boundary since the well KD-29 is just located at the boundary of the model.

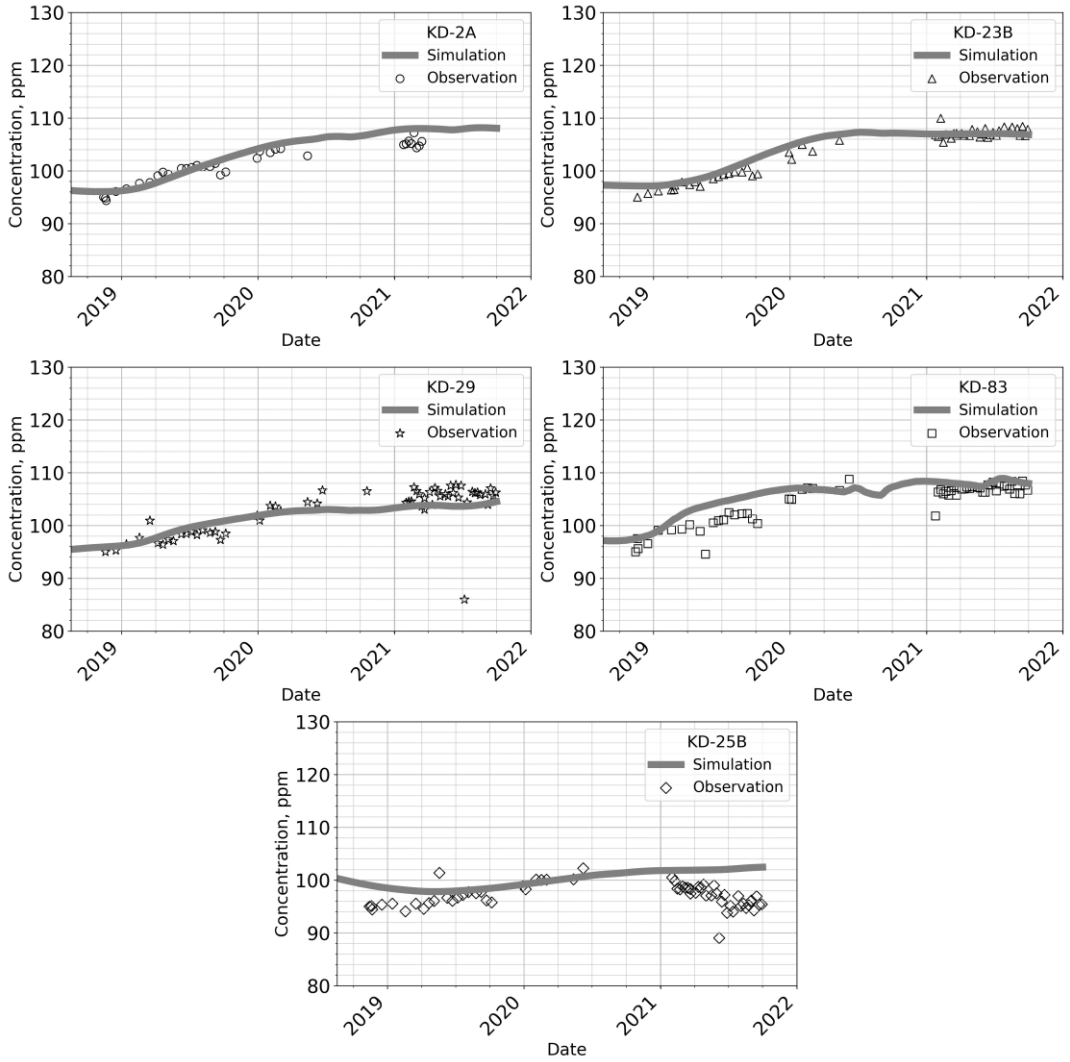

Figure 5-18 Calibration results of the chloride breakthrough curves.

In terms of the well KD-83, besides the little overestimation at the early times of the concentration history, the model captures the chloride concentrations well enough. At the earlier times, it is evident that one of the flow paths has fallen short in terms of the breakthrough time of the chloride species most probably associated with the well KD-93B since there exists a degree of misrepresentation of the breakthrough

time of 1-naphthalene-sulphonate tracer conducted from KD-93B which is depicted later in the dynamic calibration of the model (Figure 5-23).

Lastly, in KD-25B, a relatively poor match has been obtained. An early enrichment in the model has been observed then the concentration declines in the well due to the fact that the injection well KD-25A is near the KD-25B which began brine injection way earlier than other injectors, affecting the chloride concentration. Although a previous tracer test conducted from KD-25A (Akın et al., 2016) showed that there is little hydraulic connectivity exists between those wells, the model fails to capture it subsequently, enrichment occurs. After, a slight enrichment occurs in the chloride, which is mostly attributed to the hydraulic connectivity with the well KD-50A due to not only the well KD-25B being far away from the other injectors but also the slug tracer test from KD-50A (GECO 2023, This Study) showed there is a hydraulic connection exist between those wells.

Furthermore, it can be observed that after the year 2021, there are plateaus in the chloride concentrations in each well respectively where the chloride contents of the production wells do not increase any further. This occurrence can be explained by the decrease in the chloride injection rates after the mid-2020s due to a simultaneous decrease in the injection rates. However, both the dispersive transport and the small amount of chloride injection prevent the dilution of chloride in the reservoir due to brine production thus, the plateaus in the breakthrough curves are observed.

5.3.2 Slug Tracer Tests

In order to examine the hydraulic characteristics of a reservoir, various types of tracer compounds are utilized. These tracers include traditional ones like salts and dyes, reactive tracers, radioactive tracers, microbial tracers, and thermally sensitive tracers. Thermally sensitive tracers, such as naphthalene sulfonates, are frequently employed to assess the thermal condition of a geothermal system (Rose and Clausen, 2017). In the Kızıldere field, the reservoir temperature at a depth of approximately

2000 m reaches as high as 242 °C, thus, two specific naphthalene sulfonate compounds including 1-naphthalene-sulphonate and 2-6-naphthalene-disulphonate from the wells KD-93B and KD-50A respectively are used as tracers, as their thermal decay kinetics are suitable for reservoirs with temperatures of up to 300 °C (Rose et al., 2001, Rose et al. 2002). These naphthalene sulfonate compounds are injected using slugs of 200 kilograms from each well to determine the first arrival time and the mean arrival time in the production wells, as well as the total amount recovered.

In order to analyze the aforementioned individual hydraulic connectivities between the injectors and the producers, slug tracer tests must be modeled accordingly.

5.3.2.1 Slug Tracer Injection Test from KD-93B

A slug tracer test was conducted on 18.07.2018 by injecting 200 kg of a 1-naphthalene-sulphonate compound from a shallow injection well KD-93B located in the northern boundary of the sector model region. In total, the sampling has been done over 350 days, except KD-50A which turned into a re-injection well, from 6 observation wells including the wells KD-2A, KD-23B, KD-23D, KD-83, KD-50A, and KD-9A. The tracer compound arrived in all of the observation wells for which the total recovered amount is approximately 25 kg. The observed tracer breakthrough curves and the total amount of tracer recovered during the sampling period for each well are presented in Figure 5-19 respectively. Apparently, the hydraulic connectivity between well KD-93B and the well KD-2A is significantly greater compared to the other observation wells whereas, a minor amount of tracer has been recovered from wells KD-9A and KD-50A.

The exclusion of wells KD-50A and KD-9A from our numerical model is warranted during model calibration due to the limited quantities of tracer recovered in these wells. The model is considered satisfactorily calibrated when the tracer breakthrough in wells KD-50A and KD-9A is negligible or minimal, indicating that the model output is close to zero or very small.

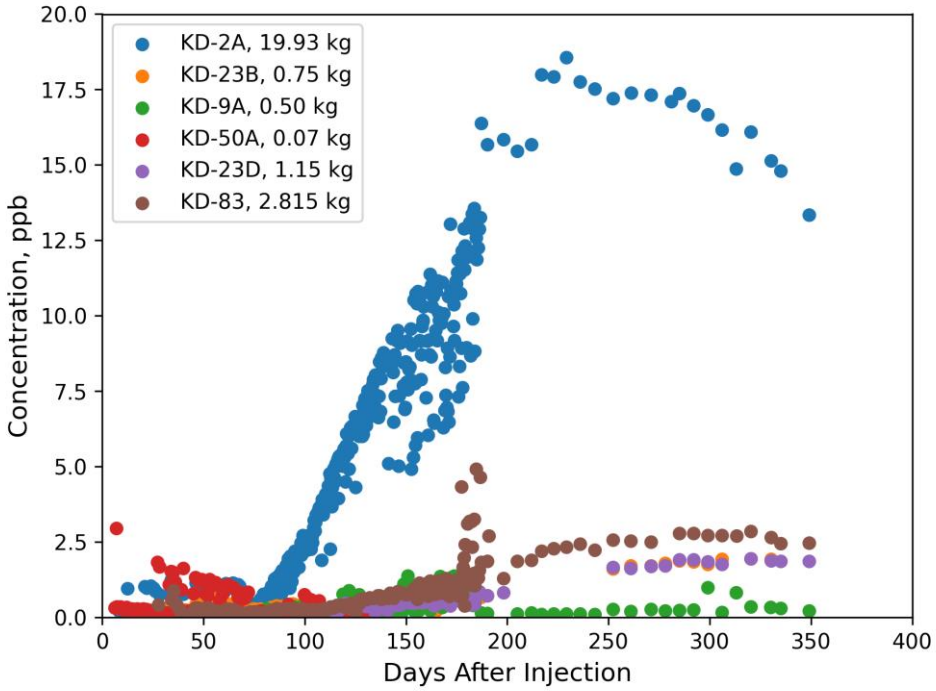

Figure 5-19 Tracer breakthrough curves and the total recovered tracer for each well.

5.3.2.1.1 Modeling Results and Discussions

This section presents the results of the numerical model by calibrating grid blocks along the flow paths in the direction of the N-S trending fault named Fault-2 between the well KD-93B and the wells KD-2A, KD-23B, KD-23D, and KD-83. Furthermore, the results of the analytical models described in Chapter 2.4 are presented and necessary parameters are determined accordingly. Note that from Figure 5-19, the sampling period of 350 days does not cover the tailing section of the breakthrough curves. Both the analytical models and the numerical model cover a period of 1000 days after the injection of the tracer however, the comparison of the models is done between the observations until the date of the last observation was taken for each well respectively.

5.3.2.1.1.1 Analytical Models

The results of the analytical model for the derived parameters as well as the forced parameters depicted in Table 5-7 for the well KD-2A. On the other hand, Figure 5-20 displays the tracer breakthrough curves for the well KD-2A determined from the optimized parameters for each analytical model respectively.

Table 5-7 Results of the analytical models for KD-2A.

Model	*Pe*	*L*	t_m	D_{tr}	*u*	*SSE*
Multi Fracture	13.97	139.74	276.75	244.76	3.25	776.27
Single Fracture	2.80	110.99	794.75	303.12	1.0342	870.03
	w	*L*	t_b			
Fracture Matrix	0.011	459293	5.39			876.84
	Pe	t_r	α	D_l	*u*	
1D Uniform	5.23	366.67	157	351.96	2.24	1076.36

For the other observation wells, KD-23B, KD-23D, and KD-83, the derived parameters, optimized parameters, and breakthrough curves are presented in Appendix B. From the fitting of the analytical models, several inferences can be pointed out.

Firstly, for the well KD-2A, the multi-fracture model including 3 separate fractures best matches the observation values. This is mostly the general case for the comparison of analytical models through all of the wells since the mult-fracture model has significantly more optimized parameters (3 optimized parameters for every fracture) when compared to the remaining analytical models. According to the results of the multi-fracture model, 3 fractures with a major fracture with a flow contribution factor of 0.56 and two secondary fractures with a flow contribution factor of 0.35 and 0.12 yielded the best match. The main fracture has the lowest storativity when compared to the secondary fractures as the mass entering the stream tube is significantly less than the others, and has a Peclet number of 13.24 indicating

that advection slightly dominates the mass transport between the wells alongside the highest flow velocity as 4.1 m^2/day. However, it should be noted that the secondary fracture with a flow contribution factor of 0.353 is also a significant contributor to the system not only because it has a significant flow contribution factor but also because the amount of tracer that enters the stream tube is much higher than the main fracture, has a Peclet number of 5.96 indicating that dispersive transport is the more active mechanism on the mass transport thus, dispersion has an important role on the overall tracer flow between the wells. Lastly, the minor fracture with a flow contribution factor of 0.12 contributes to the peak tracer concentration however, the role of this fracture in terms of the advective front and the tailing section of the breakthrough curve is little since it has a low flow velocity with a high Peclet number alongside its low flow contribution factor. For the single-fracture model, results indicated that the overall storativity between the wells is larger with remarkably lower values of Peclet number and flow velocity as 2.8 and 1.03 m/day respectively resulting in a higher degree of dispersive transport when compared to the multi-fracture model. On the other hand, the 1D homogenous model resulted in between in terms of dispersion coefficient, Peclet number, and the flow velocity of the tracer as 351.9 m^2/day, 5.23, and 2.24 m/day respectively yet again indicating that dispersive transport is a significant mechanism on the mass transport like the results of the single-fracture model. Furthermore, the fracture-matrix model yielded the highest storativity with an early response time of 5.4 days whereas, the tracer flows out of the fracture is a significant mechanism since the w parameter yielded a significantly low value of 0.011. Overall, the analytical results indicated that the storativity between the wells KD-93B and KD-2A has the highest value. Furthermore, although advection is a more dominant mechanism when compared to the flow paths between the remaining wells and KD-93B, dispersive transport remains an active mechanism. For the well KD-23B, the multi-fracture model results yielded a fracture system consisting of 3 fractures one with a low flow contribution factor of 0.048 and the most dominant one is 0.799. The main fracture has a Peclet number of 10.5 and a flow velocity of 3.07 m^2/day with the lowest storativity. In

terms of secondary fractures, the fracture with the lowest flow contribution factor displays a high dispersive transport with a comparatively high flow velocity.

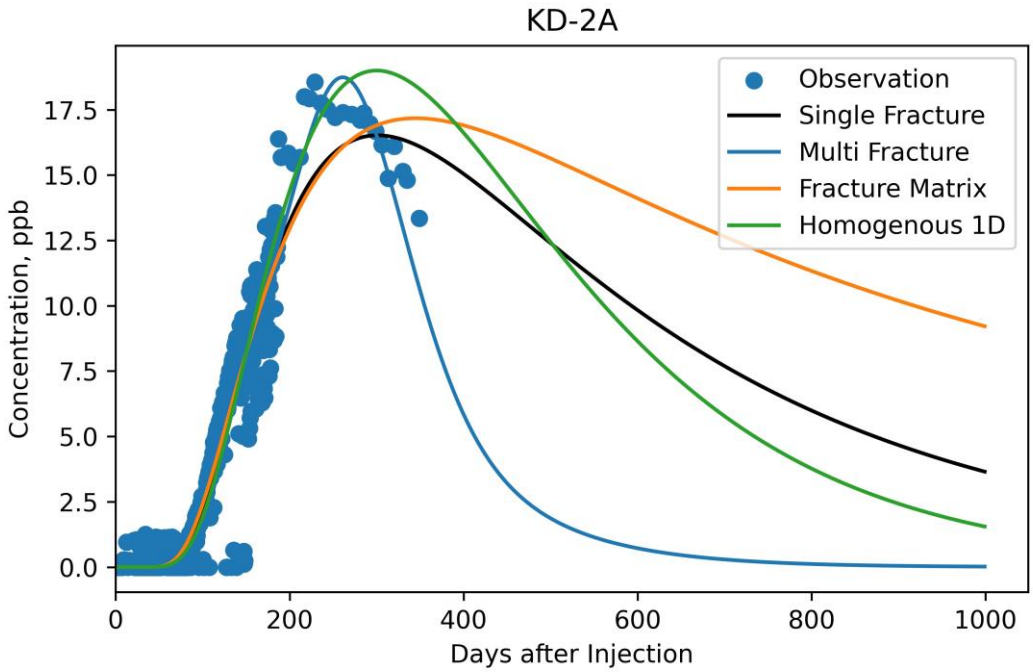

Figure 5-20 Tracer Breakthrough Curves of the Analytical Models for KD-2A.

This fracture contributes to the matching of the fast arrival of the tracer with a long tailing; however, due to its low contribution to the overall system, the effects of this fracture on the total recovery and the peak concentration are insignificant. Moreover, the secondary fracture with a flow contribution factor of 0.15 has a Peclet number of 10 with a slow advective front since the tracer's mean arrival time and the first arrival time along this fracture are significantly later than the others. Having a slightly higher storativity than the main fracture, this fracture is responsible for the tracer recovery at the later time periods. In terms of the modeling results of the single-fracture model, the Peclet number and the flow velocity values are obtained as 4.43 and 2.19 m^2/day for which those values are compatible with the fractures obtained in the multi-fracture model. Similarly, the mass entering the stream tube in the single-fracture model is between the first and the second most dominant fracture yielded in the multi-fracture model. The total storativity is much less than the well

KD-2A however, it is comparable with the wells KD-23D and KD-83. The results obtained in the 1D homogenous model are also compatible with the single-fracture model in terms of the flow velocity of 2.29 m^2/day with a higher dispersion coefficient of 1197 m^2/day which resulted in a lower Peclet number of 2.92. This can be deduced from Figure 5-20 since the 1D homogenous model resulted in significantly longer tails in the breakthrough curves compared to the single-fracture and multi-fracture models. For the fracture-matrix model, like in the case of KD-2A, the tracer transport out of the fracture is a dominant mechanism due to the low value obtained for the w parameter as 0.01.

For the well KD-23D, although the multi-fracture model yielded a fracture system consisting of 3 fractures, one of the secondary fractures has a negligible tracer mass entering the stream tube. Thus, the fracture system can be described by two fractures. The main fracture path has a significantly high Peclet number of 29.5 with a high flow velocity of 4.26 m^2/day displaying an advection-dominated mass transport. On the other hand, the secondary fracture has a much lower Peclet number of 3.60 due to high dispersivity with a dispersion coefficient of 1305 m^2/day and a relatively slow flow velocity of 3.07 m^2/day. On the overall contribution, although the main fracture has 3 times the flow contribution coefficient compared to the secondary fracture, the high storativity of the second fracture is associated with more than 3 times the mass entering the stream tube compared to the main fracture, which contributes to the overall dispersive transport between the wells KD-23D and KD-50A. This behavior is evident by the single-fracture model which yielded a Peclet number of 6.16 and a dispersion coefficient of 655 m^2/day, which indicates that dispersive transport is an active mechanism between the wells. Similar to the multi-fracture model and the analytical modeling results of the well KD-23B, in terms of mass entering the stream tube, an order of magnitude of discrepancy has been obtained when compared to the KD-2A. Furthermore, comparable results have been obtained in the 1D homogenous model compared to the single-fracture model in terms of Peclet number and flow velocity of 5.24 and 2.24 m^2/day respectively.

In terms of the multi-fracture modeling results for the well KD-83, a fracture system formed by a main fracture and a secondary fracture satisfies the observations. The main fracture with a flow contribution coefficient of 0.907 has a Peclet number of 10.37 and a flow velocity of 3.59 m^2/day. On the other hand, the secondary fracture has a much larger Peclet number of 30.17 indicating an advection-dominated mass transport between the wells alongside a small value of dispersion coefficient 117.3 m^2/day. The secondary fracture carries an order of magnitude of more tracer according to the mass entering the stream tube indicating that although this fracture has a low flow contribution coefficient. Due to its high storativity, the impact of this fracture on the overall tracer concentration profile is as high as the main fracture. On the other hand, the single fracture model and the 1D homogenous model yielded different results when compared to the multi-fracture modeling results as they yielded that dispersion plays a much more significant role in the mass transport between the wells since the resulting values for the Peclet numbers are 4.37 and 5.043 and the dispersivity coefficients are 390 m^2/day and 516 m^2/day respectively. Furthermore, the single-fracture model resulted in a higher storativity fracture compared to the wells KD-23B and KD-23D, but still much lower than the well KD-2A. Moreover, the flow out of fracture is an active mechanism compared to the flow along the fracture similar to the other observation wells hence the w parameter in the fracture-matrix model resulted in a low value of 0.08.

Overall, the analytical modeling results indicated that dispersion is an active mechanism in the mass transport between the well KD-93B and the observation wells. Furthermore, it is evident that the fracture storativity along KD-2A and KD-93B is remarkable compared to the other wells whereas, KD-83 has a slightly higher storativity compared to the KD-23B and KD-23D.

5.3.2.1.1.2 Numerical Model

The aim of the numerical model calibration consists of matching the first arrival time of the tracer compounds, the mean arrival times, the peak concentrations, and the

total amount of tracer recovery from each observation well. By doing so, aside from calibrating the model in terms of chloride concentrations presented in Chapter 5.3, individual hydraulic connectivities between the well KD-93B and the observation wells are determined. The constructed flow paths along the direction of Fault-2 between KD-93B and the observation wells are presented in Figure 5-21.

Table 5-8 Assigned geometries, anisotropic permeabilities, and porosities for the flow paths.

Flow Path	*Distance (m)*	K_{xy} *(m^2)*	K_z *(m^2)*	*Porosity (%)*
		$5 * 10^{-13} -$	$2 * 10^{-12} -$	3 - 4
KD-93B/KD-2A	849	$1.3 * 10^{-12}$	$4.5 * 10^{-12}$	
		$2.1 * 10^{-12} -$	$7 * 10^{-13} -$	3
KD-93B/KD-23D	1570	$3 * 10^{-12}$	$1 * 10^{-12}$	
		$2.5 * 10^{-13} -$	$2 * 10^{-12} -$	3 - 4
KD-93B/KD-83	1104	$2.5 * 10^{-12}$	$5 * 10^{-12}$	
		$1.5 * 10^{-12} -$	$1.5 * 10^{-12} -$	2 – 3
KD-23B/KD-23D	285	$2.5 * 10^{-12}$	$2.5 * 10^{-12}$	
		$2.5 * 10^{-13} -$	$5 * 10^{-13} -$	3 - 4
KD-93B/KD-23B	1611	$2.5 * 10^{-12}$	$5 * 10^{-12}$	
		$1.5 * 10^{-12} -$	$5 * 10^{-13} -$	3 – 4
KD-93A/KD-23D	1381	$2.1 * 10^{-12}$	$1 * 10^{-12}$	
External Paths		$5 * 10^{-13} -$	$5 * 10^{-13} -$	3 – 4
		$4 * 10^{-12}$	$2 * 10^{-12}$	
Barriers		$1 * 10^{-16} -$	$5 * 10^{-17} -$	3 - 4
		$5 * 10^{-16}$	$1 * 10^{-15}$	

Note that the calibration procedure majorly concerns the grid blocks along the flow paths, additional grid blocks are subjected to calibration to control the tracer concentration. Furthermore, the assigned anisotropic permeability and porosity values are displayed in Table 5-8.

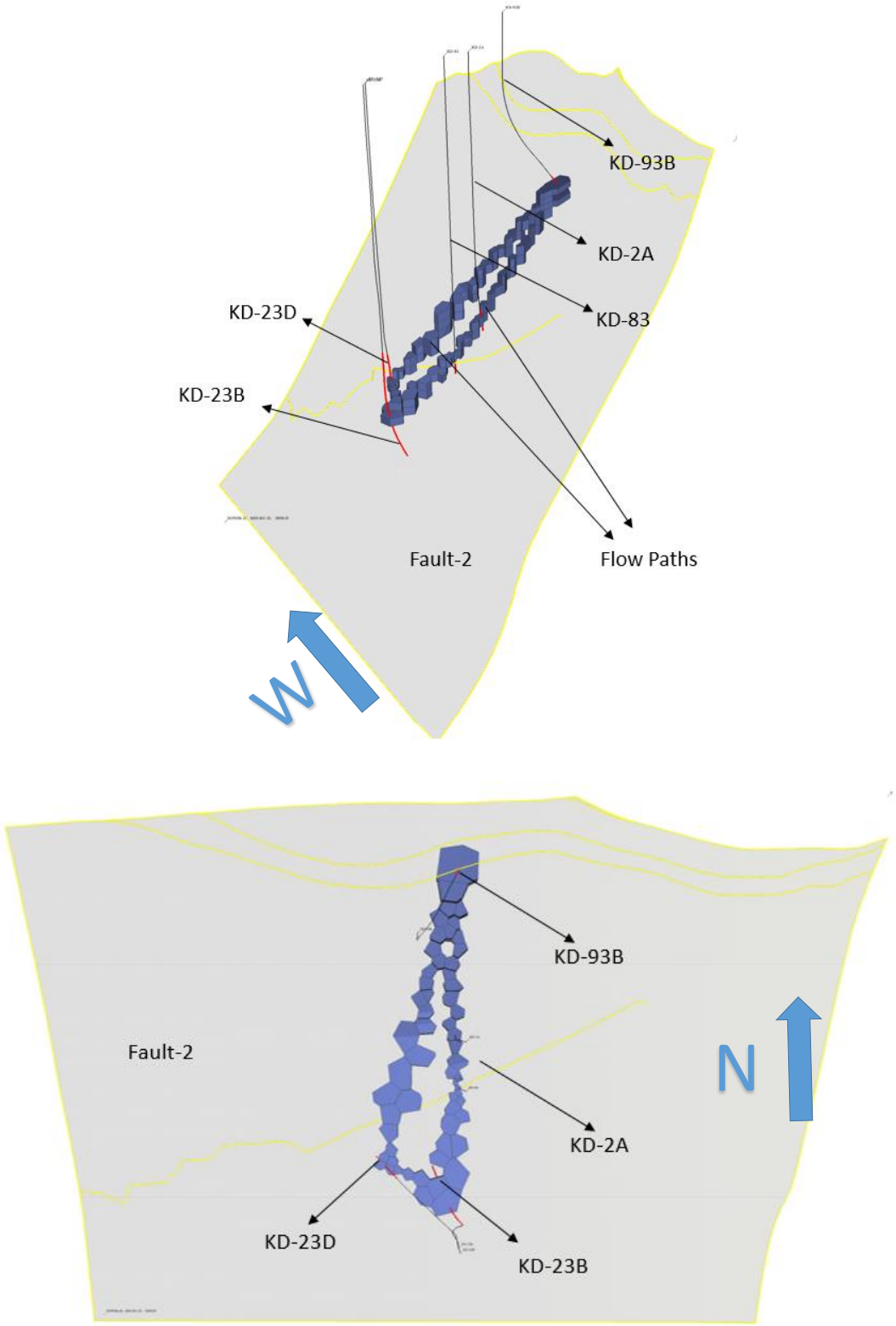

Figure 5-21 Flow paths between KD-93B and Observation Wells.

Prior to simulation results, important considerations must be pointed out. Firstly, simulating tracer transport in TOUGH2 can yield convergence problems due to the arrival of the tracer into grid blocks where zero concentration may exist. To address this issue, an initial mass fraction of tracer, 10^{-14} kg/kg, has been used; however since the tracer test was conducted 5.5 years after the numerical simulation begins, some wells can drain or dilute the initial tracer concentration to 0 in some of the grid blocks, which may arise similar convergence problems. This problem was dealt with by injecting a small amount of tracer (10^{-14} kg/s) from the well KD-93B. Furthermore, the last important consideration is that the test was conducted within half an hour in the field; however, convergence problems were faced during numerical simulation if the injection was performed at such a low time duration due to the numerical solver cutting the time step to capture the time frame of the injection.

This can be solved by using a maximum time step of around half an hour; however, the simulation time increases proportionally. Thus, in the numerical model, the injection is performed within 4 hours alongside 12 hours of the maximum time step for both avoiding the convergence errors and performing the simulation at a reasonable time. Figure 5-22 displays the tracer injection rate as well as the brine injection rate of KD-93B respectively.

The results of the model calibration in terms of tracer breakthrough curves for each observation well are presented in Figure 5-23. Furthermore, first arrival times, breakthrough times, peak concentrations, and recovered amount of tracers are indicated in Table 5-9.

According to the modeling results, the earliest arrival time that the tracer arrives at the well is KD-2A. Due to a relatively shorter distance between the KD-93B, a fast breakthrough occurs alongside the highest peak concentration observed as 18.56 ppb indicating that the flow occurs through a high permeable fracture associated with Fault-2. Furthermore, the high storativity of this fracture distinguishes the well from the others hence nearly 80 % of the recovered tracer was collected from KD-2A. The

numerical model captures the parameters indicated in Table 5-9 as 5 days separation is obtained for the first arrival time of the tracer as well as the breakthrough time.

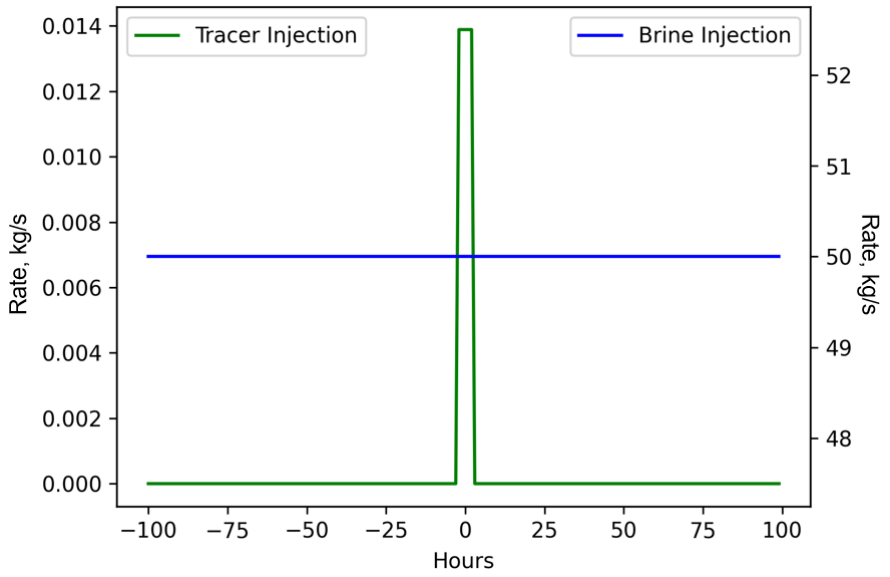

Figure 5-22 Tracer and Brine Injection Rates from KD-93B. 0 hour mark represent the instant of tracer injection.

The peak concentration in the model is with a 0.6 ppb distinction as 17.96 ppb. Thus, the model captures the advective tracer transport behavior between the KD-93B and KD-2A. However, in terms of percent error between the observation and the numerical model, a recognizable difference is obtained in terms of the total recovery of the tracer. The underlying reason is that a shorter concentration tail has been observed in the numerical model indicating that the dispersive transport is not well captured as the advective front of the tracer in which the field data and the analytical models indicate a larger dispersion between the wells.

In the well KD-23B, although the breakthrough time is captured accurately hence only a 5-day difference exists between the observation and the model, a relatively poor match has been obtained for the first arrival time of the tracer. The underlying reason could be two fractures may control the flow between the KD-93B and KD-23B one being relatively high permeable and low storativity and the other one being low permeable and comparatively high storativity than the other.

Table 5-9 Comparison between Simulation and Observation data for the slug tracer test from KD-93B. Model* indicates the total tracer recovery in 1000 days after the slug tracer injection.

		KD-2A	*KD-23B*	*KD-23D*	*KD-83*	
First arrival time	*Observation*	71	114	101	100	
(days)	*Model*	76	128	107	96	
Mean arrival time	*Observation*	229	320	292	285	
(days)	*Model*	225	315	270	253	
Peak Concentration	*Observation*	18.56	1.77	1.92	2.80	*Total*
(ppb)	*Model*	17.96	2.11	1.76	2.18	
	Observation	19.93	0.75	1.15	2.81	24.65
Recovery (kg)	*Model*	17.45	0.78	1.14	2.15	21.52
	*Model**	29.11	1.94	2.27	4.00	37.33

This claim can be supported by the multi-fracture analytical solution hence two fractures are sufficient to model the tracer transport for the well (note that the third fracture has a minor effect with a flow contribution coefficient of 0.048) where one of the fractures has a 1.53 m/day velocity with nearly twice the mass entering the stream tube whereas the other fracture has the higher velocity as 3.07 m/day with half of the mass entering the stream tube. During numerical modeling, similar behavior has been observed where a continuation of a high permeability flow path along N-S and between KD-23B and KD-23D according to Chapter 5.3-1 during modeling the chloride concentrations. During matching the tracer, a similar approach has been adopted where respective flow paths along the direction of Fault-2 and the Gebeler Fault were constructed for which they differ in permeabilities and volumes to capture the low storativity/high velocity and high storativity/low-velocity behavior. However, due to a high degree of uncertainty regarding the geometry of those flow paths, a certain level of match has been achieved. On the other hand, the match in terms of the total recovered tracer between the observation and the model results agrees satisfactorily.

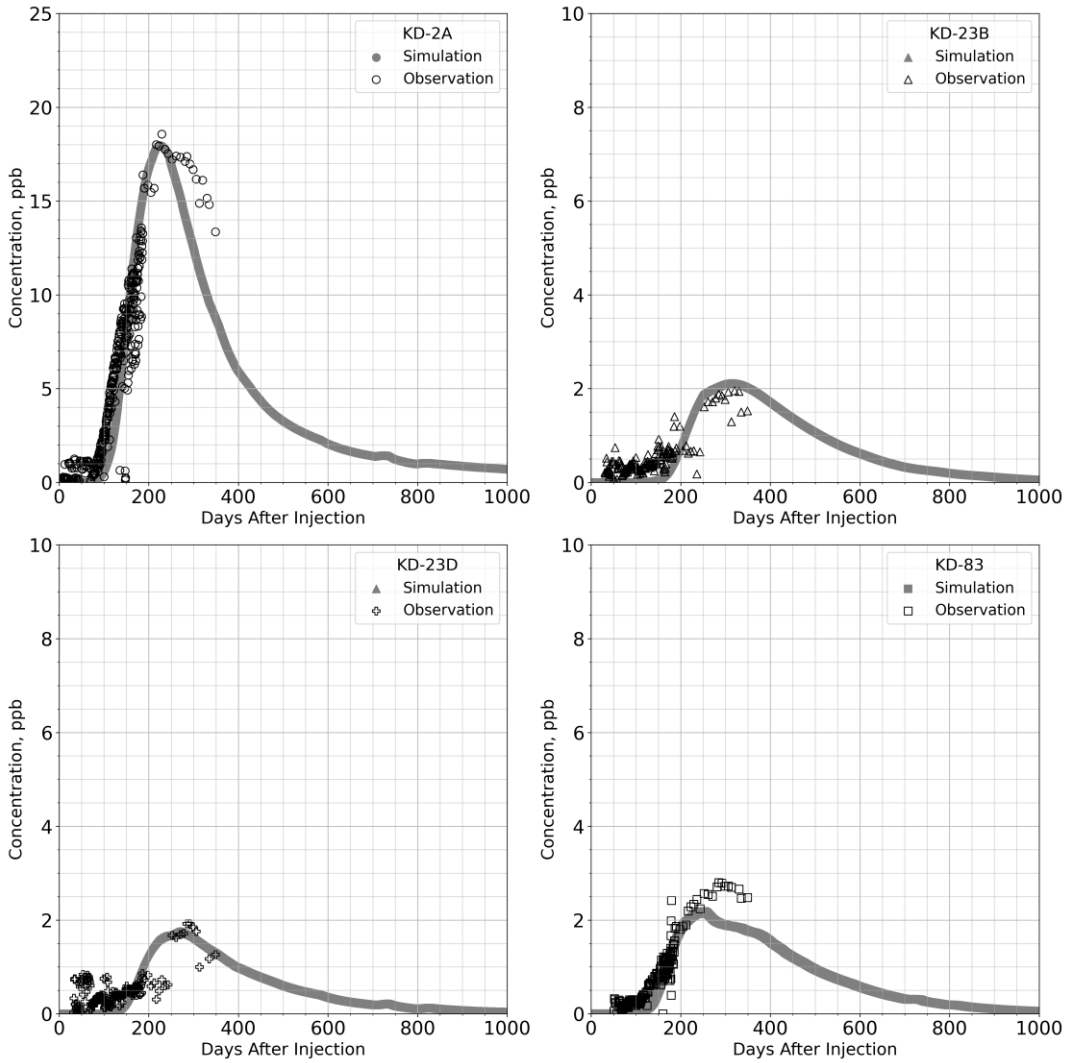

Figure 5-23 Numerical model results - Tracer breakthrough curves for the slug tracer test (1-NS) from KD-93B. The observation values are represented by the white markers and the simulated results by the dark markers.

Furthermore, an opposite modeling result has been reached for the well KD-23D compared to the KD-23B. Although the model captures the first arrival of the tracer accurately, a slight mismatch has been observed for the breakthrough times of the tracer. Yet again, a fracture system consisting of two fractures one having a higher permeability and lower storativity than the other may exist between the wells KD-93B and KD-23D could resolve the mismatch. The numerical model falls short in terms of capturing this behavior. According to the multi-fracture analytical solution, two fractures yielded the lowest SSE which is similar to the case of KD-23B,

coupling of low storativity/high-velocity and high storativity/low-velocity fractures have been observed. The main fracture has one-third of the mass entering the stream tube with a 35% higher velocity compared to the secondary fracture. In the numerical model, the constructed flow path between the well KD-93B and KD-23D along the direction of the Fault-2 behaves well enough to capture the characteristics of those fractures. A potential solution has been observed during the sensitivity analysis for the geometries of the flow paths for which a potential high permeable flow path may exist between the well KD-2A and KD-23D with a longer length. The tracer may arrive along this flow path at a relatively later time which yields a later breakthrough time similar to the observations however, construction of this flow path is not possible without intersecting the grid blocks of the other flow paths without using 3 times the grid for the layers for which the completion interval of the KD-2A passes. Furthermore, this flow path also further harnesses the tracer arriving at the well KD-83 thus, the obtained result for the well is considered the best case.

Similar results are obtained for the well KD-83 compared to the KD-23D such that the model captures the first arrival time of the tracer well enough however, deviation exists for the breakthrough times of the tracer. Aside from other wells, the largest difference has been observed in the peak concentration of the tracer. During numerical modeling, even smaller peak concentration values were observed if a single flow path was used between KD-93B and KD-83. The main reason for that is the wells KD-93B, KD-2A, and KD-83 lie on similar y-coordinates aligning them on a line. Due to KD-2A being the closer well to the injector, the arrival of the tracer is limited to the KD-83. Additional pathways are constructed to overcome this issue between the flow path connecting the wells KD-23D and KD-93B to support the arrival of tracer to the KD-83 however, the calibration of the permeabilities of the grid block in this flow channel is limited to a degree hence it diminishes the tracer which arrives to KD-23D. A possible solution for this behavior may be achieved by arranging higher storativities for the flow path between KD-23D and KD-93B to reach a larger amount of tracer to the mentioned secondary flow path; however, due to KD-2A recovering the most amount of tracer by far (nearly 80%), it is not possible

to increase the tracer mass that enters the flow path between KD-23D and KD-93B without harnessing the amount of tracer that arrives to the well KD-2A.

The following table (Table 5-10) presents the errors between the numerical model and the observation values for the first arrival and breakthrough times of the tracer, the peak concentrations, and the recovered amount of tracer for each well respectively.

Table 5-10 Errors between the numerical model and the observations for the slug tracer injection from KD-93B.

	KD-2A	*KD-23B*	*KD-23D*	*KD-83*
First arrival time	7.04 %	12.28 %	5.94 %	15.66 %
Breakthrough time	1.75 %	1.56 %	7.53 %	11.23 %
Peak concentration	3.26 %	19.02 %	8.59 %	21.91 %
Recovery	12.47 %	3.94 %	0.54 %	23.57 %

Overall, a good agreement has been reached for the tracer breakthrough curves for each well; however, a common issue is that slightly longer tails have been observed in the tracer breakthrough curves compared to the modeling results, especially for the KD-2A, which indicates that the developed model has fallen short in terms of capturing the dispersive transport of the tracer particles which is dominant in the real case. Further sensitivity analyses have been carried out during model calibration in terms of model parameters to tackle this issue. The result of the analysis has shown that higher porosity values result in a smaller pressure gradient and consequently, decrease the flow velocity, which causes the dispersion of the tracer particles from the flow paths to the surrounding grid blocks resulting in a longer tail in the breakthrough curves however at the same time, it plays a dominating factor yielding delays on the first arrival time as well as the mean arrival time of the tracer which cannot be balanced out with permeability values without disturbing the peak concentration of the tracer front. Hence, it is limited to a degree for the goodness of fit for simultaneously capturing the frontal advection of the tracer and the dispersive

fluxes when equivalent porosity models have been performed due to a lack of additional comprehensive parameters present in the dual porosity/permeability models.

5.3.2.2 Slug Tracer Test from KD-50A

A second tracer test was conducted on 11.10.2022 (Figure 5-16) by injecting 200 kg of the 2-6-naphtalene-disulphonate compound from the pilot injection well for CO_2-charged water injection, KD-50A, located in the center of the sector model region at a depth of 2392 meters. In total, sampling has been done up to 176 days from 6 observation wells including KD-2A, KD-23D, KD-83, KD-29, KD-25B, and KD-64. The 2-6-naphtalene-disulphonate compound arrived in all of the observation wells. The observed tracer breakthrough curves and the total amount of tracer recovered during the sampling period for each well are presented in Figure 5-24 respectively. Overall, the well KD-23D shows a good degree of hydraulic connectivity with the well KD-50A whereas, KD-83, KD-29, and KD-25B display a lower amount of tracer recovery respectively.

Major considerations about the tracer sampling are that, as can be observed from Figure 5-24, the sampling has started 25 days posterior to the tracer test, thus it is hard to pinpoint the first arrival time of the tracer for some observation wells including KD-23D, and KD-83. Moreover, the model calibration in previous chapters regarding chloride concentrations and slug tracer test from KD-93B showed that there is an appreciable amount of hydraulic connectivity that exists between the well KD-23B and KD-83/KD-23D; however, due to line congestion issues arose in the power plant, no sampling has been carried out from the well KD-23B.

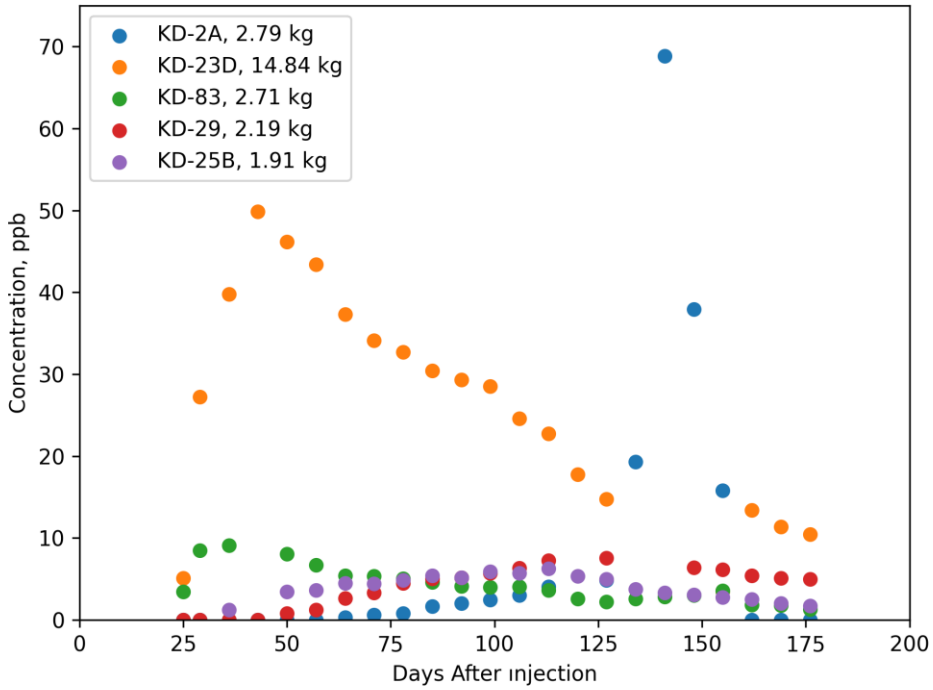

Figure 5-24 Tracer breakthrough curves and the total recovered tracer for each well.

Furthermore, an initial 2-6-naphtalene-disulphonate concentration was detected in the well KD-25B which is around 2-3 ppb. This background concentration was subtracted from the whole concentration history. Moreover, in the well KD-2A, a slow advective tracer front has been observed followed by a sudden peak with little dispersivity as the tailing section of the breakthrough curve goes to zero rapidly. This occurrence will be further discussed in the following sections.

5.3.2.2.1 Modeling Results and Discussions

This section presents the results of the numerical model by calibrating the grid blocks along the flow paths for the two major carrier faults in the sector model namely the Gebeler Fault and Fault-2 (Figure 5-26) between the well KD-50A and the wells KD-2A, KD-23D, KD-29, KD-83, and KD-25B, as well as the results of the analytical models described in Chapter 2.4 are presented and necessary parameters are determined accordingly.

It should be noted that the sampling period depicted in Figure 5-24, spans 176 days, but it does not cover the entire tailing section of the breakthrough curves. This is because there is an appreciable amount of tracer concentration observed in the last measurements from wells KD-23D, KD-29, and KD-83. Consequently, to depict the complete breakthrough curves, the numerical model is extended over a timeframe of 500 days following the tracer injection. Nevertheless, when comparing the models, the observations are limited to the data collected until the latest observation date for each respective well.

5.3.2.2.1.1 Analytical Models

The results of the analytical models for the derived and optimized parameters and the first arrival time of the tracer compound are depicted in Table 5-11 for the well KD-23D whereas, Figure 5-25 displays the tracer breakthrough curves for the well KD-23D determined from the optimized parameters for each analytical model respectively. The remaining observation wells, KD-2A, KD-25B, KD-83, and KD-29, the derived parameters, optimized parameters, and the tracer breakthrough curves are presented in Appendix C. Several conclusions can be derived from the application of analytical models.

Table 5-11 Analytical Model Results for KD-23D.

Model	*Pe*	*L*	t_m	D_{tr}	*u*	*SSE*
Multi Fracture	14.26	210.434	85.11	283.52	6.91	167
Single Fracture	4.41	132.354	96.48	550.57	5.02	428
	w	*L*	t_b			
Fracture Matrix	0.444	29067.1	17.52			185
	Pe	t_r	α	D_l	*u*	
1D Uniform	6.35	61.62	76.20	598.36	7.85	652

Firstly, the results of the well KD-23D, the multi-fracture solution can fit the data by using two fractures with a first arrival time of tracer in 16 days. The characteristics of those fractures differ from one another one being a dominant factor while fitting the advective front of the tracer arrives to the well with a high Peclet number of 27.1 and the secondary fracture displaying a later breakthrough time with lower velocity and a Peclet number of 3.13 indicating a low permeable and more storativity along this fracture as the mass entering the stream tube in this fracture is significantly larger.

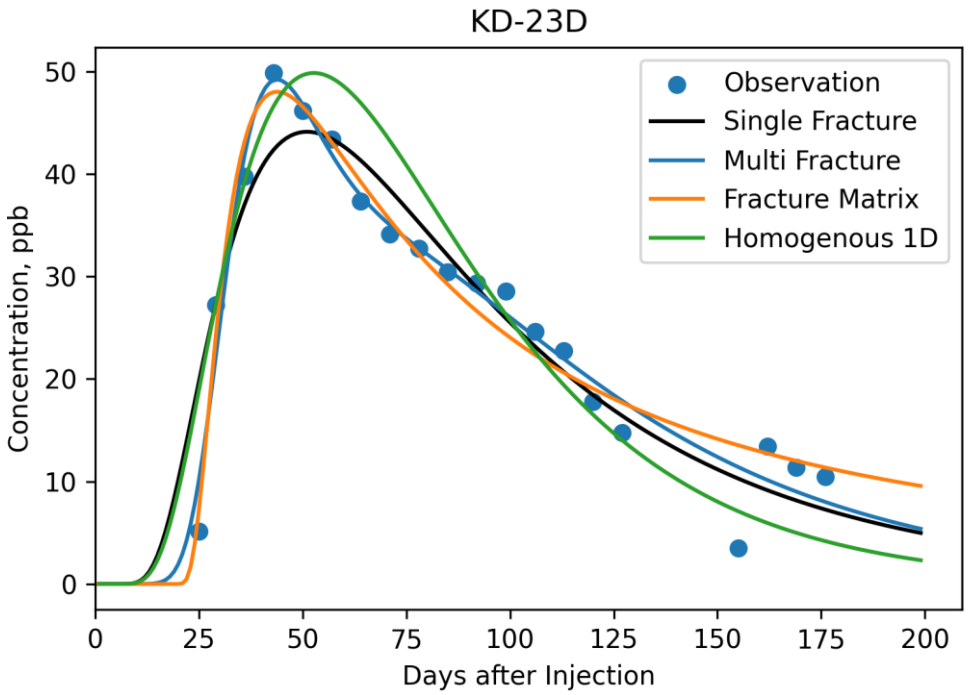

Figure 5-25 Tracer Breakthrough Curves of the Analytical Models for KD-23D.

The single-fracture model displays an earlier first arrival time of the tracer compound with 12 days for which the flow velocity and the Peclet number are smaller than the overall multi-fracture model to match the tailing of the breakthrough curve better. Although the fracture-matrix model displays the latest first arrival time of the tracer with 24 days due to the fracture-matrix model being more sensitive to the observations for the first arrival time of the tracer, the early breakthrough time of the tracer is caught by the model indicating a fast advective

front velocity of the tracer along the fracture as a high value of the w parameter is obtained meaning the transport along the fracture is significant between the wells. Note that as the first arrival time is not certain with observations, the parameter w can be even larger with an earlier response start time. Lastly, the 1D Homogenous model yielded similar results to the single fracture model with a little bit more advection dominating the transport between the wells.

Furthermore, like in the case of KD-23D, 2 fractures are suitable during the multi-fracture solution for the well KD-83 where the first tracer arrives at the well in 18 days according to the model. Although the overall Peclet number is obtained as 19.71, the majority of the tracer that enters the stream tube is transported to the fracture where the fluid velocity is considerably lower than the other which corresponds to a fast advective front and a long tailing section in the breakthrough curve. In the single-fracture model, a slower fluid velocity has been observed along the fracture compared to the multi-fracture model. A more dominant dispersive transport with similar storativities compared to the multi-fracture model resulted since the fast advective front of the tracer with a long tailing section restricts the single-fracture model in terms of capturing both. The fracture-matrix model yielded similar results with KD-23D where it captures the fast advection and long tailing of the breakthrough curve where the w parameter yielded a value of 0.57 meaning that there exists some degree of flow out of the fracture alongside the flow along the fracture. Lastly, the 1D Homogenous model resulted in a Peclet number of 4.78 indicating that dispersive transport is a dominant mechanism along the flow paths between KD-50A and KD-83.

In KD-29, two fractures are enough to fit the observations with the multi-fracture model for which one fracture dominates the system with a 0.921 flow contribution coefficient with a lower Peclet number and flow velocity while the other fracture is more permeable and half the storativity. The first arrival time of the tracer resulted in the multi-fracture model is 40 days whereas, the single-fracture model displayed the earliest first arrival time of the tracer in 35 days. The model resulted in a more active dispersive transport compared to the multi-fracture model for which the

Taylor dispersivity yielded a higher value and the Peclet number yielded a lower value with a slower flow velocity when compared to both fractures obtained from the multi-fracture model. From the analysis of the fracture-matrix model, the flow towards the matrix from the fracture is more dominant when compared to the wells KD-23D and KD-83 while a significantly more tracer mass entering the stream tube has been observed. Furthermore, the results of the 1D Homogenous model showed similar results with the single-fracture and multi-fracture models as the Peclet numbers and the dispersion coefficients are in the range of those models.

In KD-25B, aside from the aforementioned wells, 3 fractures are sufficient to match the data rather than 2. Although the flow velocities are similar in each fracture, substantially low dispersive, high Peclet numbers are obtained in two minor fractures where the dominant fracture has a lower Peclet number and a higher Taylor dispersivity. The multi-fracture model is the only model for the well which accurately matches the first arrival of the tracer within 25 days however, as previously mentioned, a background concentration was detected in the well hence, the uncertainty in the first arrival time of the tracer applies for the well. The single-fracture model is compatible with the multi-fracture model since the flow velocity along the fracture and the mass entering the stream tube are similar to the overall results of the multi-fracture model whereas, a higher Peclet number and a lower Taylor dispersivity have been obtained when compared to the main fracture in the multi-fracture system resulting in a more convection-dominant fluid flow. Furthermore, the results of the 1D Homogenous model resulted in an appreciable amount of Peclet number of 22.53 indicating a convection-dominant flow such as the previous models where the flow velocities are similar as well. Lastly, in terms of the fracture-matrix model, a poor match has been obtained during the optimization.

In KD-2A, different characteristics have been observed aside from the aforementioned wells. From Figure 5-24, it can be observed that a relatively slow advective front reached the well followed by a sudden peak and a rapid decrease in the concentration which went to 0 ppb. According to the multi-fracture model, two fractures with similar flow contribution coefficients (0.4 and 0.6) and velocities

match the observations with comparable flow velocities to the other wells however, they yielded very low Taylor dispersivities resulting in significantly high Peclet numbers (238.72 and 56.17) between the well and KD-50A. The fracture displaying the higher Peclet number also carries more tracer as the mass entering the stream tube is nearly 50% higher than the other fracture, further forcing the concentration to rapidly go to 0 after the mean arrival time. In terms of the single-fracture model, similar results are obtained in terms of the flow velocity, Taylor dispersivity, Peclet number, and the mass entering the stream tube with the main fracture path obtained in the multi-fracture model indicating a convection-dominant transport along the fracture. However, the parameters including the first arrival time, mean arrival time, and the peak tracer concentration are not obtained as well as the multi-fracture model. Furthermore, in the 1D Homogenous model, a slightly higher flow velocity is obtained compared to the single fracture model resulting in a slight increase in the Peclet number of 74.3. When compared to the multi-fracture model, the 1D Homogenous model falls short in terms of capturing the first arrival and mean arrival time of the tracer. Lastly, in terms of the fracture-matrix model, a poor match has been obtained during the optimization. Thus it can be concluded that for the well KD-2A, the multi-fracture model with two fractures represents the model significantly better where convection is the predominant mechanism for the fluid flow.

Further important considerations should be pointed out in terms of the observations and the analytical modeling results regarding the well KD-2A. Although similar results are reached in terms of flow velocities and distances between the remaining observation wells, distinctive results are obtained including low values of dispersivities and high Peclet numbers compared to the other observation wells. Furthermore, those mentioned characteristics have not been observed with the past tracer tests conducted in the sector model region (Erol et al., 2022, Akın et al., 2016) as well as the calibration results in the previous chapters including the tracer test from KD-93B and chloride concentration curves thus, the case of mismeasurement

is present in the well. This issue will also be discussed in the numerical modeling results section accordingly.

5.3.2.2.1.2 Numerical Model

Similar to the slug tracer test conducted from KD-93B, the aim of the numerical model here is yet again the calibration of matching the first arrival time of the tracer, the mean arrival times, the peak concentrations, and the total amount of tracer recovery from each observation well. Subsequently, further calibration of the reservoir model will be achieved on top of the results of the tracer test from KD-93B and the results of the model calibration in terms of chloride concentrations where the model lacks the individual hydraulic connectivities between the observation wells and KD-50A.

Table 5-12 Assigned geometries, anisotropic permeabilities, and porosities for the flow paths.

Flow Path	*Distance (m)*	K_{xy} *(m^2)*	K_z *(m^2)*	*Porosity (%)*
KD-93B/KD-2A	849	$5 * 10^{-13} - 1.3 * 10^{-12}$	$2 * 10^{-12} - 4.5 * 10^{-12}$	3 - 4
KD-93B/KD-23D	1570	$2.1 * 10^{-12} - 3 * 10^{-12}$	$7 * 10^{-13} - 1 * 10^{-12}$	3
KD-93B/KD-83	1104	$2.5 * 10^{-13} - 2.5 * 10^{-12}$	$2 * 10^{-12} - 5 * 10^{-12}$	3 - 4
KD-23B/KD-23D	285	$1.5 * 10^{-12} - 2.5 * 10^{-12}$	$1.5 * 10^{-12} - 2.5 * 10^{-12}$	2 – 3
KD-93B/KD-23B	1611	$2.5 * 10^{-13} - 2.5 * 10^{-12}$	$5 * 10^{-13} - 5 * 10^{-12}$	3 - 4
KD-93A/KD-23D	1381	$1.5 * 10^{-12} - 2.1 * 10^{-12}$	$5 * 10^{-13} - 1 * 10^{-12}$	3 – 4

Table 5-12 (continued)

		$5.8 * 10^{-13} -$	$8.7 * 10^{-13} -$	2.75 – 3
KD-50A/KD-29	714	$2.2 * 10^{-12}$	$3.3 * 10^{-12}$	
		$1.5 * 10^{-12} -$	$7.5 * 10^{-13} -$	3 – 3.25
KD-50A/KD-25B	400	$2 * 10^{-12}$	$1 * 10^{-12}$	
		$1.25 * 10^{-12} -$	$7.5 * 10^{-13} -$	2.25 – 3.25
KD-50A/KD-2A	450	$2 * 10^{-12}$	$1 * 10^{-12}$	
		$2 * 10^{-12} -$	$1 * 10^{-12} -$	2.75 – 3
KD-50A/KD-23D	484	$3 * 10^{-12}$	$1.5 * 10^{-12}$	
	486	$4 * 10^{-13} -$	$2 * 10^{-13} -$	2 – 3
KD-50A/KD-83		$2 * 10^{-12}$	$1 * 10^{-12}$	
External Paths		$5 * 10^{-13} -$	$5 * 10^{-13} -$	3 – 4
		$4 * 10^{-12}$	$2 * 10^{-12}$	
Barriers		$1 * 10^{-16} -$	$5 * 10^{-17} -$	3 - 4
		$5 * 10^{-16}$	$1 * 10^{-15}$	

The constructed flow paths along the direction of the Gebeler Fault and Fault-2 between KD-50A and the observation wells, as well as the concerning flow paths between the well KD-93B (Figure 5-21) and regarding observation wells, are presented in Figure 5-26. The major calibration procedure mostly concerns those grid blocks but is not limited since the surrounding grid blocks around the flow paths also contribute to the mass transport process. The assigned permeability and porosity values as well as the external flow paths are displayed in Table 5-12.

Similar to the numerical simulation for the slug tracer test from KD-93B, convergence problems arise in TOUGH2 due to zero concentration of tracer before the injection from KD-50A. However, in this case, the tracer test was conducted 9.5 years after the numerical simulation begins hence, a higher initial concentration of tracer must be used than 10^{-14} kg/kg since there exists a longer time duration for the

wells drain or dilute the initial tracer concentration to 0. Thus, an initial concentration of 10^{-10} kg/kg has been used.

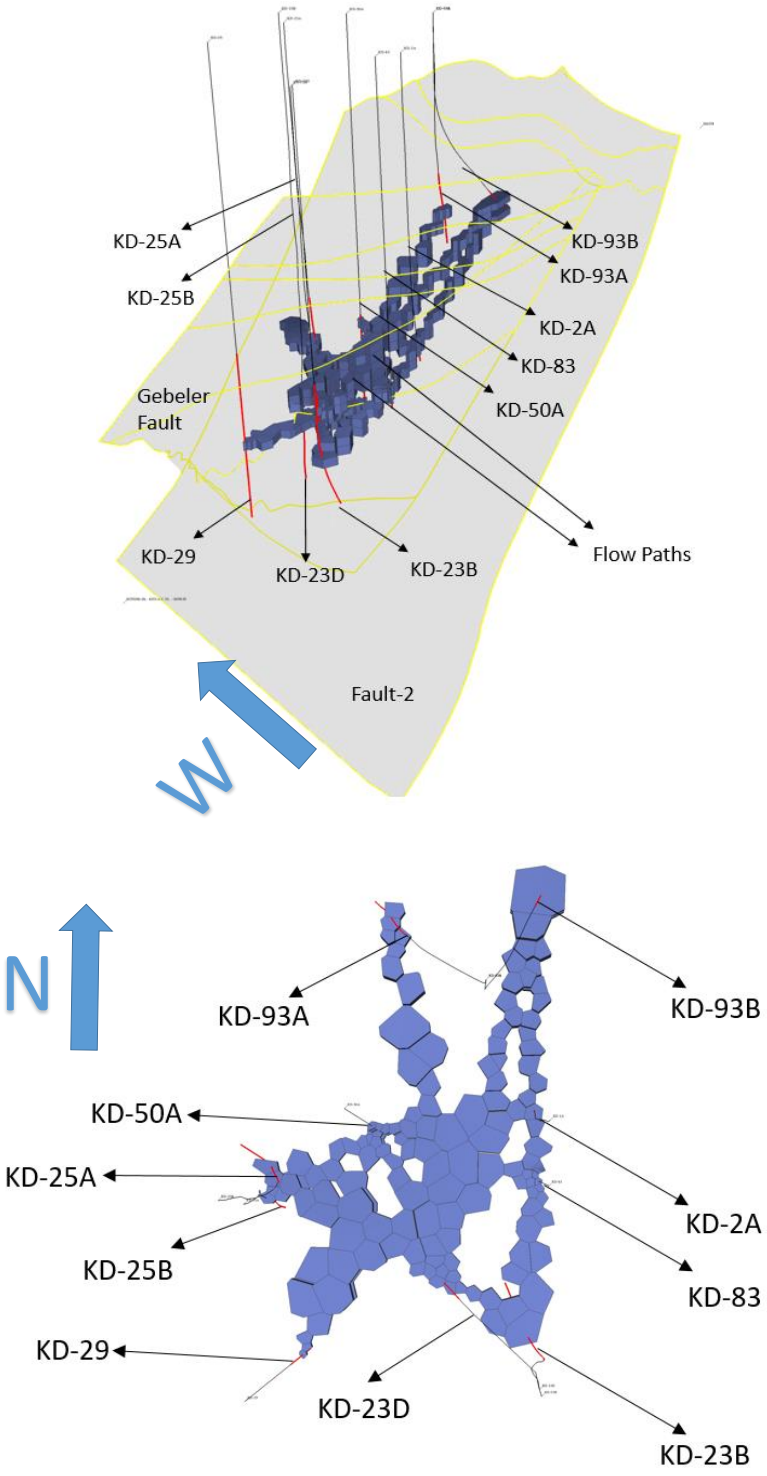

Figure 5-26 Flow paths between KD-93B, KD-50A, and neighbor wells.

If there exists an initial concentration in the modeling results, this concentration has been subtracted accordingly. Furthermore, the tracer injection duration, rate, and maximum time step used in the model are the same as the previous slug injection test from KD-93B.

The results of the model calibration in terms of tracer breakthrough curves for each observation well are presented in Figure 5-27. Furthermore, first arrival times, breakthrough times, peak concentrations, and recovered amount of tracers are indicated in Table 5-13.

Table 5-13 Comparison between Simulation and Observation data for the slug tracer test from KD-50A. Model* indicates the total tracer recovery in 500 days after the tracer injection.

		KD-29	KD-23D	KD-83	KD-25B	KD-2A	KD-2A*
First arrival time (days)	*Obs.*	43-50	<25	<25	36-43	57-64	57-64
	Model	38	12	9	31	58.5	58.5
Mean arrival time (days)	*Obs.*	127	43	36	113	-	141
	Model	121	43.5	42	102	194	194
Peak Concentration (ppb)	*Obs.*	7.56	49.85	9.11	6.25	-	68.83
	Model	7.81	49.8	9.14	6.53	10.1	10.2
Recovery (kg)	*Obs.*	2.19	14.84	2.71	1.91	0.45	2.79
	Model	2.26	13.2	3.05	1.96	0.42	1.25
	*Model**	5.96	17.81	6.94	4.04	4.81	4.81

Overall, a good agreement has been reached between observations and the modeling results for the observation wells except for the well KD-2A.

The modeling results for the well KD-29 yielded a faster advective front of the tracer as both the first arrival time and the mean arrival time of the tracer is nearly 6 days prior to the observations. On the other hand, the tailing of the breakthrough curves yielded a good match indicating that the dispersive transport is accurately captured

by the model. Hence, a small overestimate of the tracer recovery until the last observation value has been obtained. Furthermore, the majority of the tracer has been recovered from the well after the mean arrival time of the tracer which demonstrates that dispersion plays an important role in terms of mass transport between the wells KD-50A and KD-29.

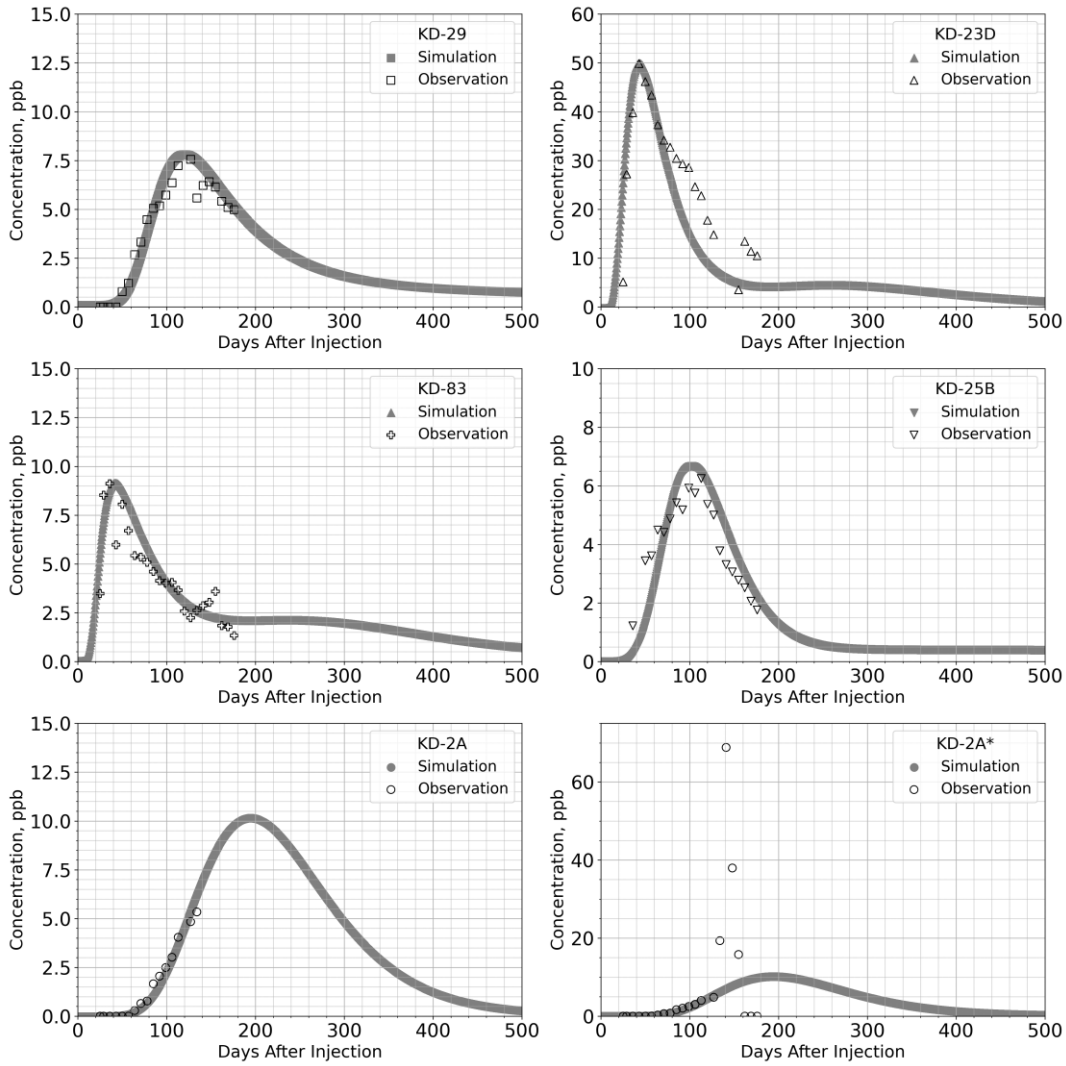

Figure 5-27 Numerical model results - Tracer breakthrough curves for the slug tracer test (2-6-NS) from KD-50A. The observation values are represented by the white markers and the simulated results by the dark markers.

During numerical modeling, this occurrence has been obtained in two distinct ways. Firstly, the flow path between KD-50A and KD-29 is by far the longest distance

among other flow paths hence, the tracer compound has more chance to disperse away from the flow paths to the surrounding grid blocks, yielding the long tailing of the breakthrough curve. On the other hand, the grid blocks along the flow path are designated so that two polygonal grid blocks have the same connection between the third grid block, one being a larger volume than the other. This third grid block receives the tracer compound from the smaller one with a faster velocity whereas, receives the tracer at a slower velocity from the larger grid block, aiding the simultaneous capturing of the advective front and the tailing of the breakthrough curve.

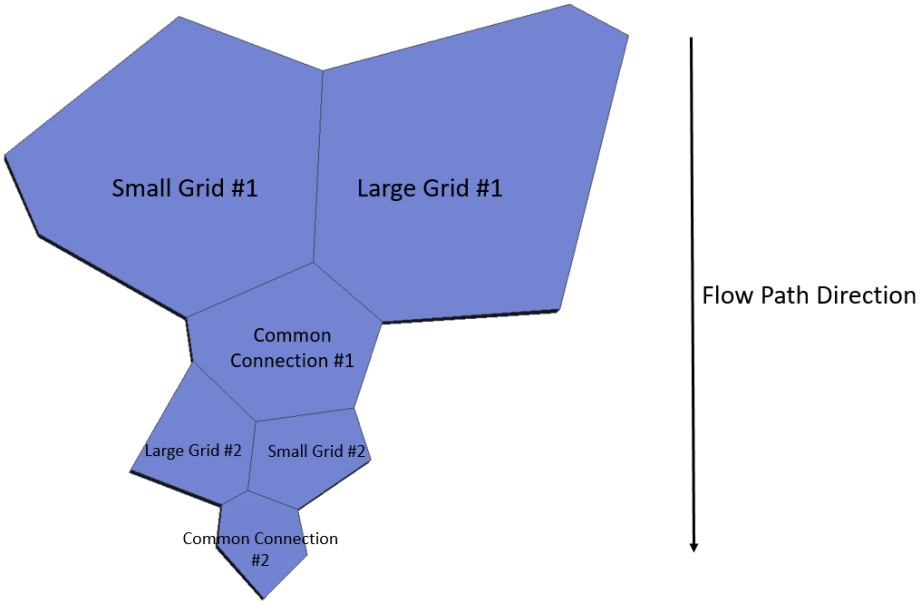

Figure 5-28 Multiple grid connections along the flow paths (KD-29).

Note that this implementation is not limited to the calibration of the flow path between KD-29 and KD-50A hence, a fast advective front with long tailing of the breakthrough curves was observed in some of the wells (Figure 5-24). The illustration of this type of grid connection is presented in Figure 5-28

The modeling results of the well KD-23D show the best match in terms of the first arrival time, the mean arrival time, and the peak concentration of the tracer. Although the first arrival time of the tracer was not obtained through the observations, the single-fracture model and multi-fracture model indicated the first arrival time of the

tracer as 12 and 16 days respectively which are compatible with the modeling results. A noticeable disagreement can be observed in the tailing section of the breakthrough curves between the model and the observations between 92 and 113 days after the tracer injection which yielded an underestimation of the total tracer recovered by 1.6 kilograms. Three considerations regarding this occurrence can be made first of which is that there exists a second fracture having a relatively higher storativity and a lower velocity aside from the flow path between KD-50A and KD-23D. This fracture governs the late arrival of the tracer yielding high concentrations later in the breakthrough curve where the multi-fracture model demonstrated such results discussed in the previous chapter. Secondly, as the most tracer arrives at the well KD-23D with the earliest arrival time second to KD-83, the tracer re-circulation affects the well the most hence, higher concentrations were observed in the tracer breakthrough curve. Finally, high permeability flow paths along the direction of Fault-2 (Table 5-8, Table 5-12), which are modeled in the previous chapter may affect the concentration similar to the first indicated reason, yielding a second later arrival of the tracer. However, this case is irrelevant according to both the observations and the modeling results since not only the first arrival time of the tracer would be later to the well but also the storativity of this channel is not that much to alter the breakthrough curve. On the other hand, this flow path contributes to the overall tracer recovered from the well as can be observed in the breakthrough curve, stagnation occurs after 220 days, increasing the collected amount of tracer from the well.

The modeling results of the KD-83 have a good agreement in terms of the peak tracer concentration and the first arrival of the tracer. Yet again, the first arrival time of the tracer was not exactly detected by the observations, both the single-fracture model and the 1D Homogenous model indicated 10 days of first arrival time after the injection which is 1 day off with the modeling results. A slight mismatch has been obtained in terms of the mean arrival time of the tracer by 6 days which is probably associated with a slight misrepresentation of the velocity of the tracer along the flow path between KD-50A and KD-83. Similar to the case of KD-23D, alterations in the

breakthrough curve were observed between 134 and 155 days after tracer injection for which the aforementioned reasons can also be attributed to the KD-83. Furthermore, the flow paths calibrated in the previous chapter (Table 5-8) contribute to the overall tracer recovery, which doubles the total recovered tracer between the last observation time to 500 days as can be observed in the breakthrough curve, stagnation occurs after 220 days, similar to the KD-23D. Lastly, the total recovery of the tracer matches well enough until the last observation day with a 0.34 kg difference is obtained resulting due to the aforementioned slightly slower velocity of the tracer front.

The modeling results of KD-25B showed a slightly faster advective front has been obtained compared to the observed values since both the first arrival time and the mean arrival time of the tracer are 6-10 days earlier than the observed values. This issue has been optimized through either decreasing the permeability or decreasing the porosity of the grid blocks along the flow path however, extreme adjustments of those parameters yielded a lower peak concentration of the tracer. Perhaps the issue can be tackled by creating a longer flow path with a similar storativity to delay the first and mean arrival times however, this adjustment is limited to the number of grids hence longer flow paths resulted in an interference of the flow paths between the well KD-29 and KD-50A. The dispersive transport has been modeled accurately since the tailing of the breakthrough curve matches the observed concentrations. Subsequently, the model captures the total recovered tracer with a 0.05 kg difference in between. Furthermore, no stagnation has been observed beyond the last observation since unlike the wells KD-23D and KD-83, no flow channels have been observed to externally carry the tracer compound to the well.

The modeling results of KD-2A yielded poor agreement with the observed values. According to the observation values, a slow advection front reaches the well for which the first arrival time of the tracer is between 57-64 days. However, after 134 days of injection, a sudden spike has been observed for which the concentration increases from 4.84 ppb to 68.83 ppb. This occurrence is most probably associated with a secondary fractıre having a low velocity and high storativity as the multi-

fracture model is the only analytical model that captured the slow increase and the sudden spike on the breakthrough curve. Furthermore, a second issue associated with the well is that the high peak tracer concentration quickly went to 0 ppb in under 20 days. This behavior indicates very large Peclet numbers with slow flow velocities indicating that dispersion plays little to no role in the mass transport between the wells KD-50A and KD-2A which are not observed in any of the aforementioned observation wells. This type of behavior cannot be captured with the numerical model shown in Figure 5-27, where the last breakthrough curve labeled as KD-2A** displays the raw observations compared with the numerical modeling results for which the only accurate parameter that has been accurately calibrated is the first arrival time of the tracer. During numerical modeling, the extremely low dispersivity is tried to be mimicked by increasing the permeability and decreasing the porosity along the flow path constructed between the well KD-2A and KD-50A alongside decreasing the permeability and increasing the porosity and volume factors of the grid blocks surrounding the flow path. Although the dispersion is reduced when compared to the final modeling results indicated in Figure 5-27, the fluid velocity increased sharply alongside the peak tracer concentration resulting in high tracer recovery as well as an early breakthrough time from the well. To tackle this issue, the same procedure has been applied by constructing a longer flow path between the wells to delay the first arrival and mean arrival time of the tracer while controlling the dispersivity as explained, similar results have been obtained with the final model. Thus, in light of the analytical results and the modeling results, a consideration of inaccurate measurement is present. If so, the breakthrough curve labeled as KD-2A in Figure 5-27 accurately represents the behavior present in the reservoir by capturing the advective front of the tracer as both the first arrival time and the total tracer recovery to the 134 days.

Overall, the modeling results for the 2-6-naphtalene-disulphonate slug tracer test conducted from KD-50A show a good match except for the well KD-2A. Alongside the 1-naphthalene-sulphonate slug tracer test conducted from KD-93B as well as modeling the chloride concentrations, the numerical model sets a basis for predicting

the CO_2-charged brine injection process from KD-50A. In the next chapter, the impact of the injection process as well as hypothetical scenarios are examined respectively.

CHAPTER 6

CO_2 INJECTION SCENARIOS

In this chapter, the calibrated numerical model is used to demonstrate the impact of CO_2-charged brine injection to observe the long-term storage capabilities of the Kızıldere geothermal reservoir. The section covers the following points accordingly.

- Brief description of the CO_2 injection system.
- The predictive modeling of the real-life scenario which has been implemented as 985 tons in 6 months of injection operation in the Kızıldere geothermal field.
- Hypothetical coupled scenarios to observe the CO_2 storage capabilities of the reservoir with varying injection rates of CO_2, different injection durations, constant production rates, and deliverability models.

An important consideration is that during CO_2-charged brine injection, based on previous modeling studies regarding the field indicated that limited mineral carbonation due to low concentrations of cations such as Ca^{+2}, Fe^{+2}, and Mg^{+2} in the reservoir for which those cations are the most suitable to form carbonate minerals thus, solubility trapping and structural trapping remains the primary trapping mechanism present in the reservoir for the sequestration of the CO_2 (Erol et al. 2022, GECO 2023, Erol et al. 2023). Furthermore, during both studies, authors showed that even though the injection capacity increased 2 times compared to the real-life scenario which corresponds to 4,000 tons a year, which is compatible with the maximum injection rate (5,000 tons/year) of the following scenarios, the partial pressure of CO_2 remains high enough to keep it in the aqueous phase. Assuming those findings are valid in our case, the following predictive models presented in the upcoming sections implement the TOUGH2 v2.0 EOS1 package since, in the absence of two-phase conditions and non-reactivity, the dissolved CO_2 will be

transported with the re-injection water, displaying a similar behavior of a conservative tracer.

6.1 Brief Description of the CO_2 Injection System

One week after the 2-6-naphthalene-disulphonate slug tracer test from the pilot injection well KD-50A, on 18.10.2022 (Figure 5-16), the CO_2-charged brine injection was implemented from the well for a duration of more than 6 months. The detail of the CO_2 injection system can be analyzed in Figure 6-1. In this design, non-condensable gases (NCG) that are released at 85 °C are collected from the exhaust at the power plant's cooling tower and to the compressor inlet system. The pressurized NCG is mixed with bypass pond water at the outlet of the compressor around 12 to 14 bar-g. This CO_2-charged mixture is called Mix_1. A booster pump is used to pressurize the mixture to 34 bar-g to send it to the re-injection wellhead and mix there with the re-injection brine. The final mixture (Mix_2) at the KD-50A wellhead is injected into the reservoir.

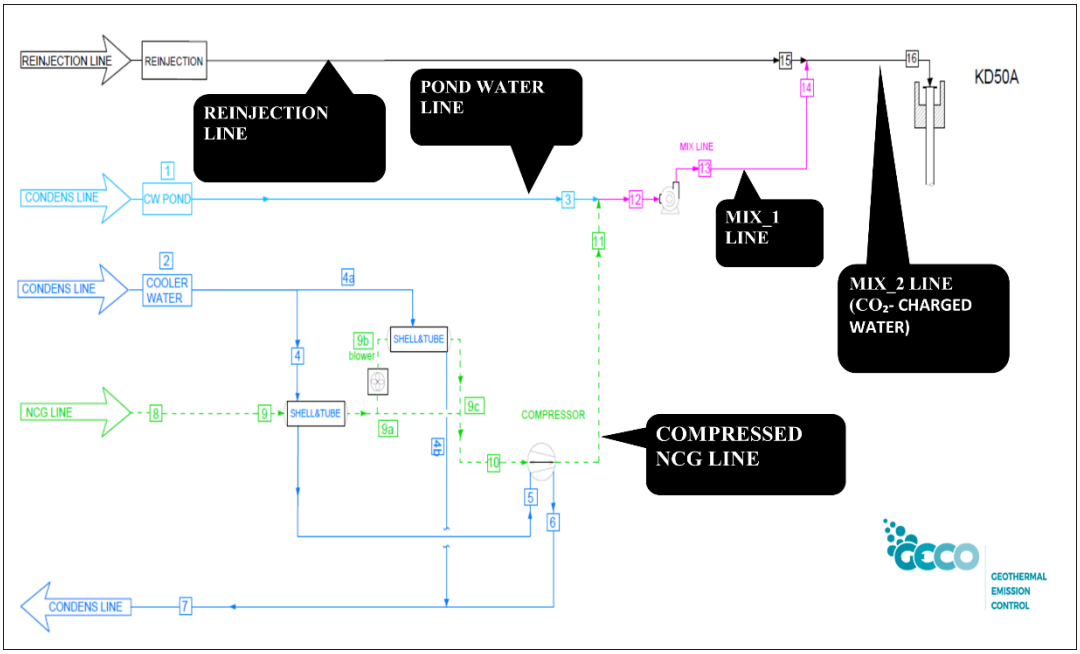

Figure 6-1 Carbon dioxide injection system.

6.2 Real-life CO_2 Injection Scenario

Over the course of 6 month period, the NCG, Mix_2, has been injected into the reservoir from KD-50A at an average temperature of 70 °C with flow rates ranging between 38 kg/s to 52 kg/s corresponding to a total of 985 tons of CO_2 during the operation period. Figure 6-3 indicates the gauge readings during the CO_2 injection duration. As can be observed, a constant flow rate could not be achieved under dynamic conditions, and flow rates have fluctuated in a particular range. For various reasons, the compressor has been shut down three times on different dates, as indicated by red vertical lines in Figure 6-2 and Figure 6-3.

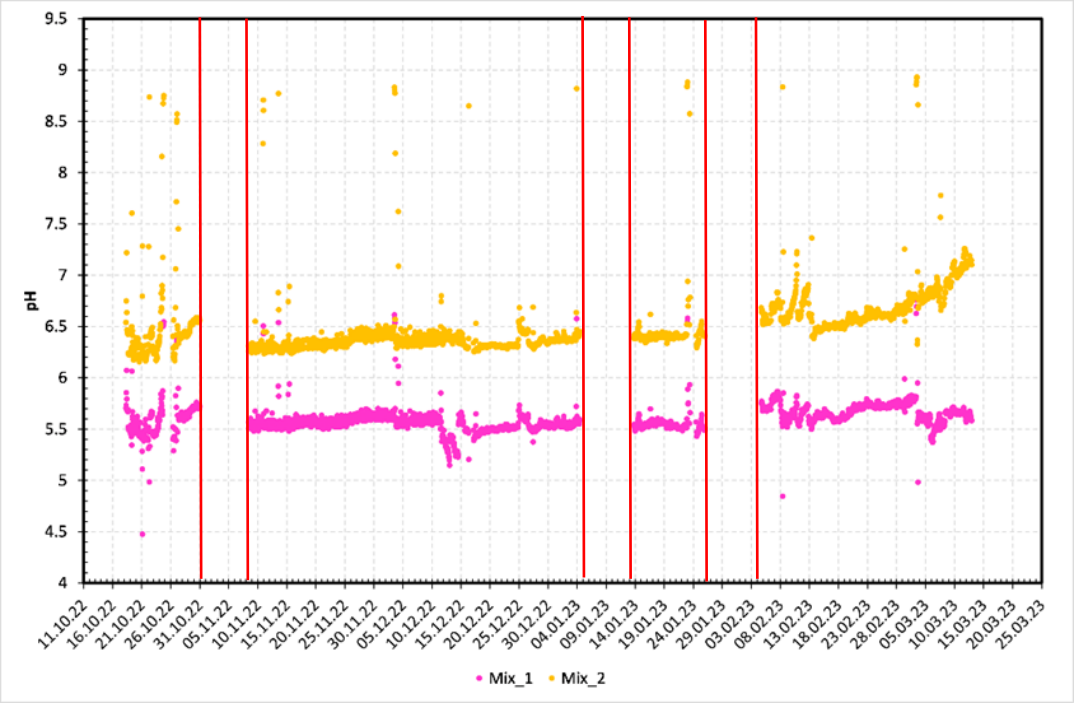

Figure 6-2 pH of CO_2-charged water (GECO, 2023).

After the injection had been started, the wellhead pressure of the well KD-50A was gradually decreased while receiving larger amounts of injection fluid (Figure 6-3) for which under no alterations, the inverse situation may observed indicating that an increase in the well injectivity takes place. This alteration in the injectivity of KD-50A probably occurred due to the fact that the CO_2-charged mixture (Mix_1)

increases the acidity of the re-injection water while forming the CO_2-charged brine injected from the well (Mix_2). The decreased pH (Figure 6-2) compared to the regular re-injection water which is historically around 9.5 enhances the dissolution of carbonates in the vicinity of KD-50A and subsequently increases the permeability around the well thus, an increase in the injectivity has been observed.

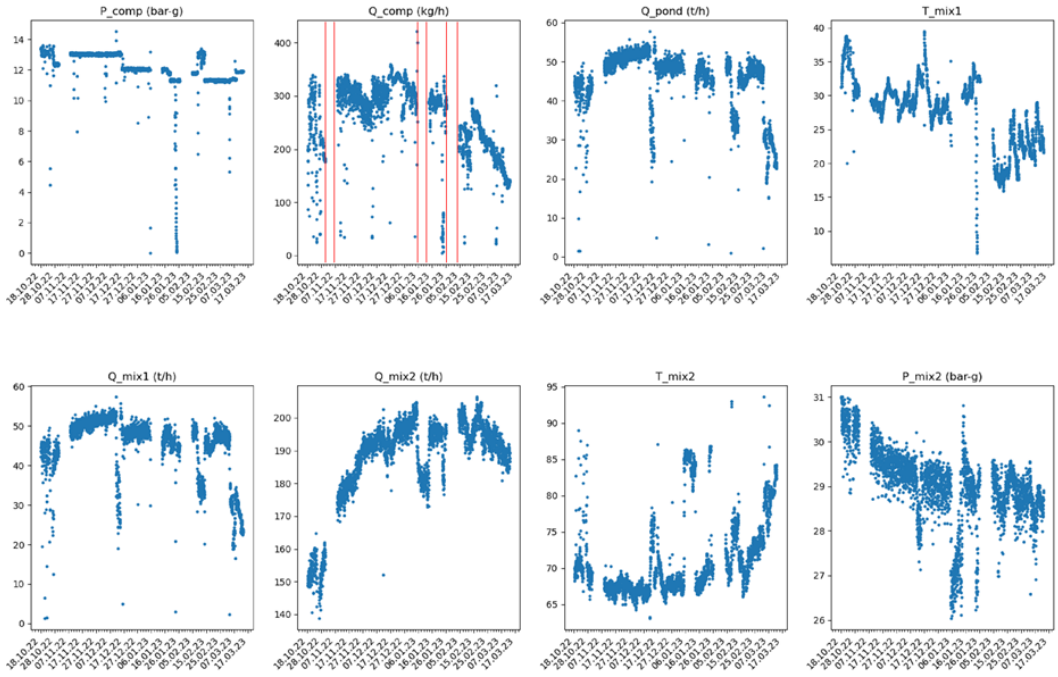

Figure 6-3 Injected Fluid's mixture rates, pressures and temperatures (GECO, 2023).

6.2.1 Numerical Modeling Results and Discussions

The injection results display compatible outcomes in terms of the mean arrival time of CO_2, peak CO_2 concentration, and total CO_2 recovery for each production well (Table 6-1) with the tracer test conducted from the same injection well in Chapter 5.3. The CO_2 breakthrough curves are indicated in Figure 6-4 whereas, the CO_2 distribution along the depth interval of 1700 and 2100 meters after 3 months, 6 months, 2 years, and 4 years after the injection has been illustrated in Figure 6-5. Note that in the figure, the green dots represent the well for which the main feed

zones of the wells lie between the indicated depth interval whereas, for the magenta dots, the main feed zones are not.

According to Figure 6-5, an immediate increase in CO_2 up to 300 ppm has been observed along the flow path between KD-50A and KD-23D whereas, a minor amount of CO_2 has been transported to the wells KD-83 and KD-2A. Furthermore, a significant amount of CO_2 can be observed at the west of the well KD-50A due to the fact that high permeability and storativity fractures associated with the Gebeler Fault exist along that direction (Table 5-12) however, the impact of those fractures do not contribute to the nearby wells KD-25B and KD-29 due to formations with little permeability has been obtained during 2-6-naphthalene-disulphonate tracer test and past tracer tests from other nearby injection wells such as KD-25A (Akın et al. 2016). After 6 months when the injection stops, still a high amount of CO_2 flows through the well KD-23D, and the impact of the minor flow paths between the flow path of KD-23D and KD-93B and KD-83 is visible at that time. Moreover, the amount of CO_2 continuously increases at the west of KD-50A. Two years after the injection begins, the breakthrough curves showed that the CO_2 contents of the wells are all decreasing. An important consideration is that after 2 years, the CO_2 reaches the model boundary for which the boundary effects can be an important consideration from that time for longer injection periods however in the current case, it is not since a low amount of CO_2 concentration reaches to the boundary (<10 ppm). Finally, after 4 years, the majority of the injected CO_2 is either produced from the wells (approximately 20%) or diluted by the injection wells as little amount of CO_2 remains in the model when compared to the concentrations right after the injection stops.

As can be observed from the breakthrough curves, KD-23D is by far the most CO_2 receiving well such that nearly 50 % of the recovered CO_2 is collected through an 8-year time period. An immediate sharp increase in the CO_2 content of the well has been observed due to the high velocity of the fluid through the high-permeable flow path. The sharp decrease in the CO_2 concentration after the peak concentration time is probably underestimated by the model since in Chapter 5.3, the tracer

breakthrough curve of the well showed a slight mismatch in the tailing section. The aforementioned discussion during the 2-6-naphthalene-disulphonate tracer test calibration regarding a secondary arrival of the tracer has contributed to the total recovered tracer from the well as it can be seen that around late 2023 to early 2024, a smaller peak has been observed according to the modeling results. By the end of 2025, no significant trace of injected CO_2 has been observed according to the modeling results (Figure 6-5).

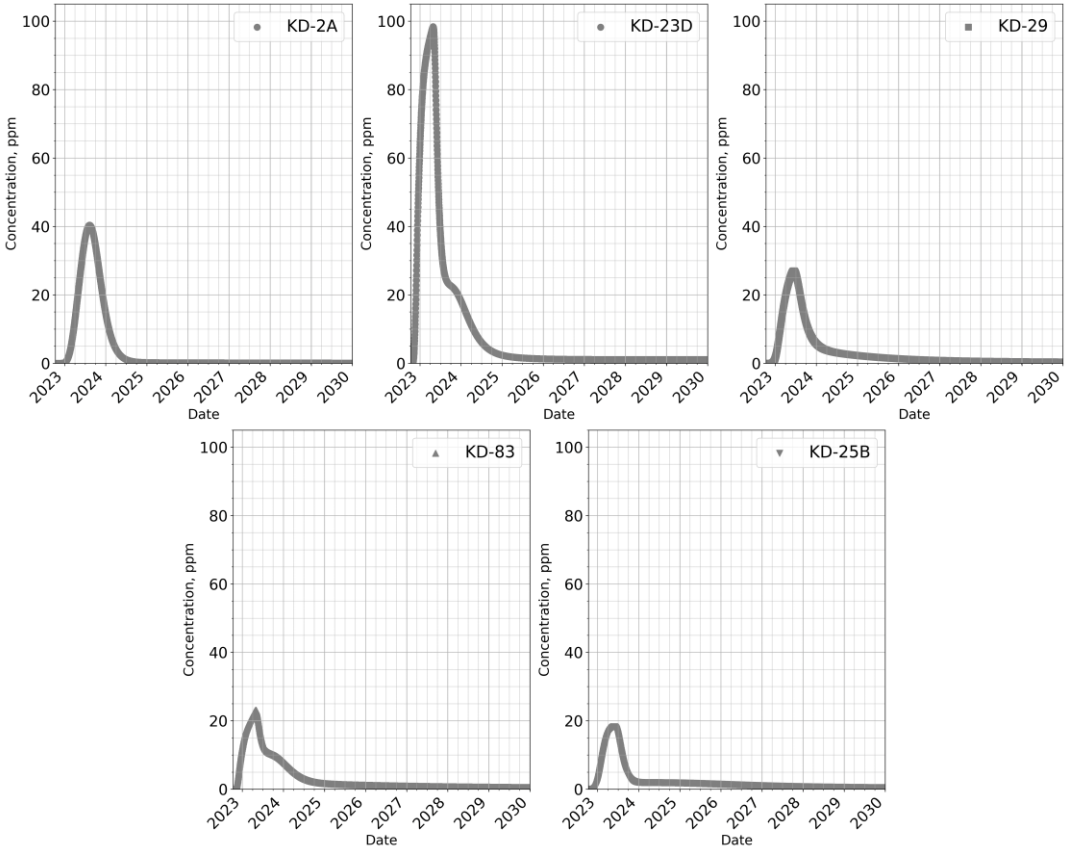

Figure 6-4 CO_2 breakthrough curves, 985 tons 6 months of injection, up to 2030.

For the well KD-83, similar to the KD-23D, a fast advective front of CO_2 has been observed compared to the other production wells due to high-permeable flow channels carrying the CO_2-charged brine faster to the well. Yet again similar to the KD-23D, a secondary arrival of CO_2 has been observed in a similar time period resulting from the high-permeability, N-S trending flow channels subsequently, an

increase in the total CO_2 recovery has been observed. However, in the case of KD-83, the relative contribution of this flow channel is significantly greater than KD-23D as it yielded a significant amount of arrival of the mixture after the peak concentration time when compared to the total recovery of the well.

Table 6-1 Peak concentrations, peak concentration times, and total recoveries of CO_2 for each production well.

	KD-2A	*KD-23D*	*KD-83*	*KD-29*	*KD-25B*
Peak Concentration, ppm	40.35	98.37	23.10	27.00	18.29
Peak Concentration Time, days	296	191	195	240	222
Total Recovery, tons	23.31	103.48	34.75	27.89	20.79
Recovery, %	2.37	10.51	3.53	2.83	2.11
Total Recovery, tons	210.24				

In terms of KD-29, the effects of the injection last longer than any other well due to not only the greatest distance among other production wells exists between the wells KD-50A and KD-29, but also as the modeling results of 2-6-naphthalene-disulphonate tracer test indicated that the dispersive transport is a highly dominant mechanism for the mass transport between those two wells. Thus, up until 2027, the CO_2 contents of KD-29 do not go to 0 ppm.

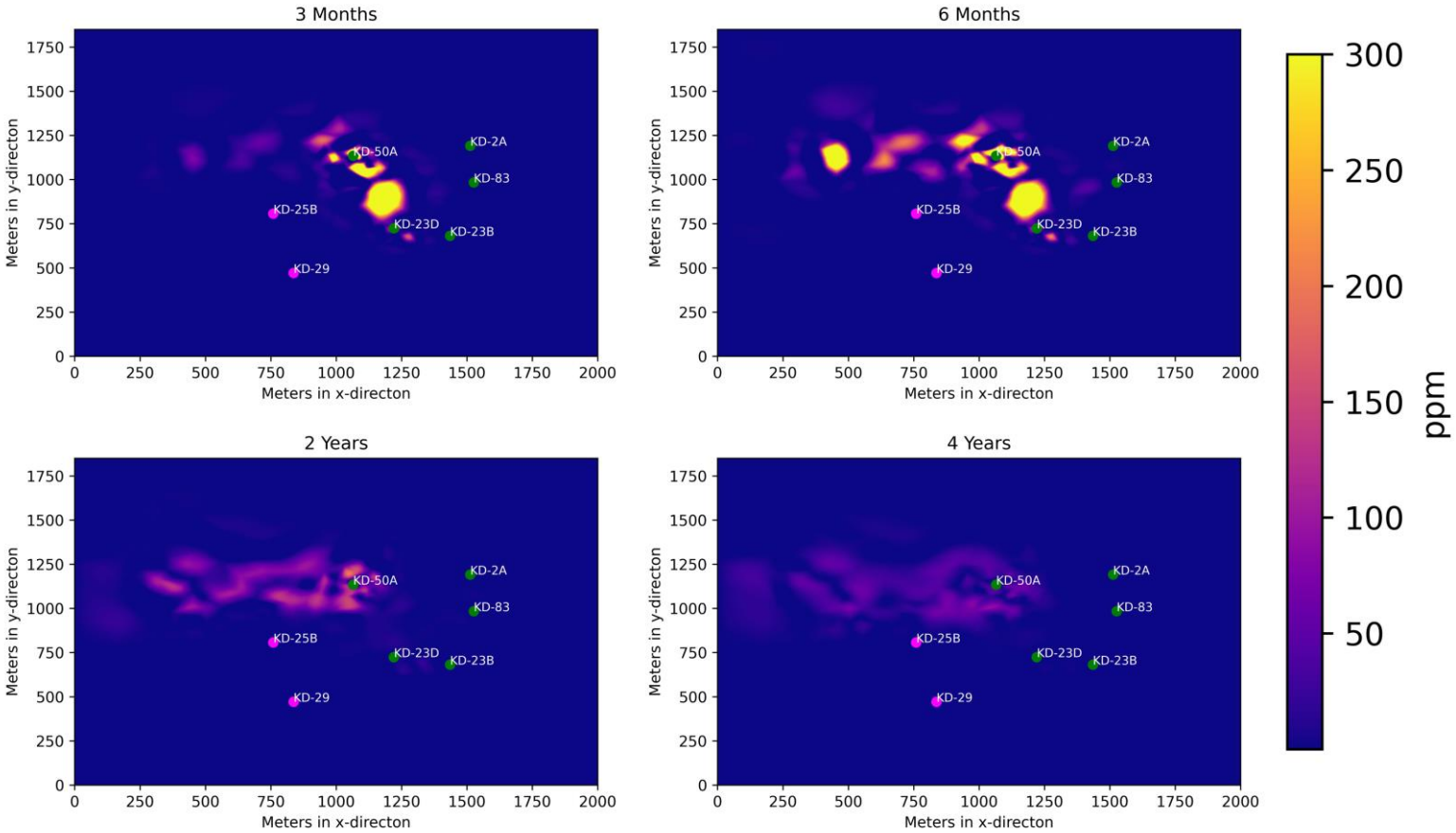

Figure 6-5 The CO_2 distribution of 985 tons of injected CO_2 in 6 months after 3 months, 6 months, 2 years, and 4 years of injection

In terms of KD-2A, a similar amount of total recovery of CO_2 is observed with the well KD-29 with higher and earlier peak concentration values due to shorter distance with KD-50A and lower storativity flow paths however, the dispersive transport is much more active in KD-29 as comparatively higher amounts of CO_2 is collected by the well KD-29 to KD-2A. However, due to the aforementioned modeling shortages in Chapter 5.3, the real scenario may prevail to one-third of CO_2 being recovered from the well when compared to the modeling.

Furthermore, the modeling results of KD-25B displayed the least amount of CO_2 recovery due to a fast advective front associated with low storativity flow paths. A small amount of CO_2 still arrives the well after 2025 due to CO_2 being transported from the high permeable and high storativity flow paths from KD-50A to the western boundary of the model along the Gebeler Fault.

6.3 CO_2 Injection Scenarios

Predicting the impact of the CO_2-brine injection under different production and injection conditions is vital for estimating the capacity of the amount of CO_2 that can be injected into the Kızıldere reservoir. In that manner, the following injection and production scenarios for the wells that lie inside the sector model region have been investigated under two different strategies, three different injection rates, and four different injection durations.

1. Keeping the production rates constant.
    - Injection of CO_2-brine mixture under three different rates and four different injection durations.
        - 1250 tons/year.
        - 2500 tons/year.
        - 5000 tons/year.

      coupled with

        - 6 months of injection.

- 12 months of injection.
- 24 months of injection.
- 8 years of injection.

2. Keeping the pressure decline as low as possible by arranging the brine production rates under different bottom-hole flowing pressure conditions with a fixed injection rate of 2500 tons/year of 12 months injection.
    - The possible cases of changes in bottom-hole flowing pressure.
        - -6 bar.
        - -3 bar.
        - +0 bar.
        - +3 bar.
        - +6 bar.

6.3.1 Keeping the Production Rates Constant

Under constant production rates of the wells as depicted in Figure 5-15, in total, 12 scenarios for the injection of CO_2-brine mixture have been investigated. The following figure illustrates a CO_2 injection rate example for one of the simulated scenarios for KD-50A under 2500 tons/year injection for 24 month time period.

Furthermore, the CO_2 breakthrough curve for the same scenario of 24 months of 2500 tons/year injection is illustrated in Figure 6-7.

According to the modeling results for the depicted twelve scenarios (Table 6-2) with constant production rates and varying injection rates with varying durations, the percent recovery of the injected CO_2 does not change significantly. Overall, the recoveries ranged between 21 % to 22 % which is compatible with the results of the real-life CO_2 injection strategy and the tracer test results in Chapter 5.3. In Table 6-2, the blue highlighted lines represent the 1250 tons/year of injection, the red highlighted lines represent the 2500 tons/year of injection and the black highlighted lines represent the 5000 tons/year of injection respectively.

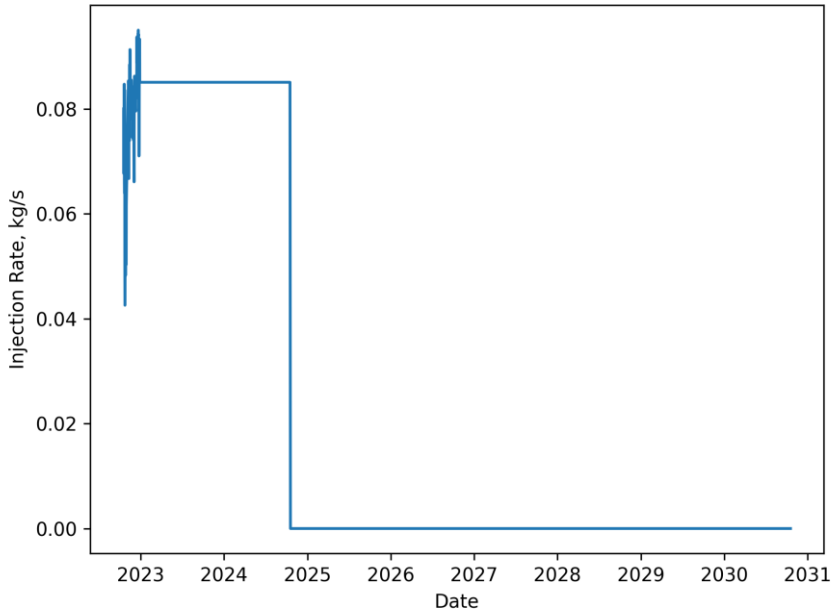

Figure 6-6 CO_2 injection rate for 2500 tons/year and 24 months.

According to the modeling results, although the injection rate has little impact on the recovery percent of the injected CO_2, it can be observed that for 6 months of CO_2 injection, the recovery percent is always the same as 21.34% for each injection rate respectively.

Table 6-2 Results of the constant rate CO_2 injection scenarios.

Total Injected, tons	*Total Recovered*	*Recovery %*	*KD-2A %*	*KD-23D %*	*KD-83 %*	*KD-25B %*	*KD-29 %*
625	133.36	21.34%	2.37%	10.50%	3.53%	2.11%	2.83%
1250	272.17	21.77%	2.41%	10.71%	3.60%	2.15%	2.91%
2500	547.066	21.86%	2.41%	10.76%	3.60%	2.15%	2.95%
10000	1937.67	19.38%	2.13%	9.89%	3.07%	1.74%	2.55%
1250	266.80	21.34%	2.37%	10.51%	3.53%	2.11%	2.83%
2500	544.41	21.78%	2.41%	10.71%	3.60%	2.15%	2.91%
5000	1093.04	21.86%	2.41%	10.75%	3.60%	2.15%	2.95%
20000	3875.54	19.38%	2.13%	9.89%	3.07%	1.74%	2.55%

Table 6-2 (continued)

2500	533.62	21.34%	2.37%	10.51%	3.53%	2.11%	2.83%
5000	1088.84	21.78%	2.41%	10.71%	3.60%	2.15%	2.91%
10000	2186.12	21.86%	2.41%	10.75%	3.60%	2.15%	2.95%
40000	7751.55	19.38%	2.13%	9.89%	3.07%	1.74%	2.55%

The impact of injection duration for the same injection rate has a little bit more impact on the total recovery such that as the injection duration increases, around 0.3 % of more CO_2 is recovered from all of the wells respectively for which this variation is associated with a minor incremental pressure difference occurs between the flow paths and the surrounding grid blocks.

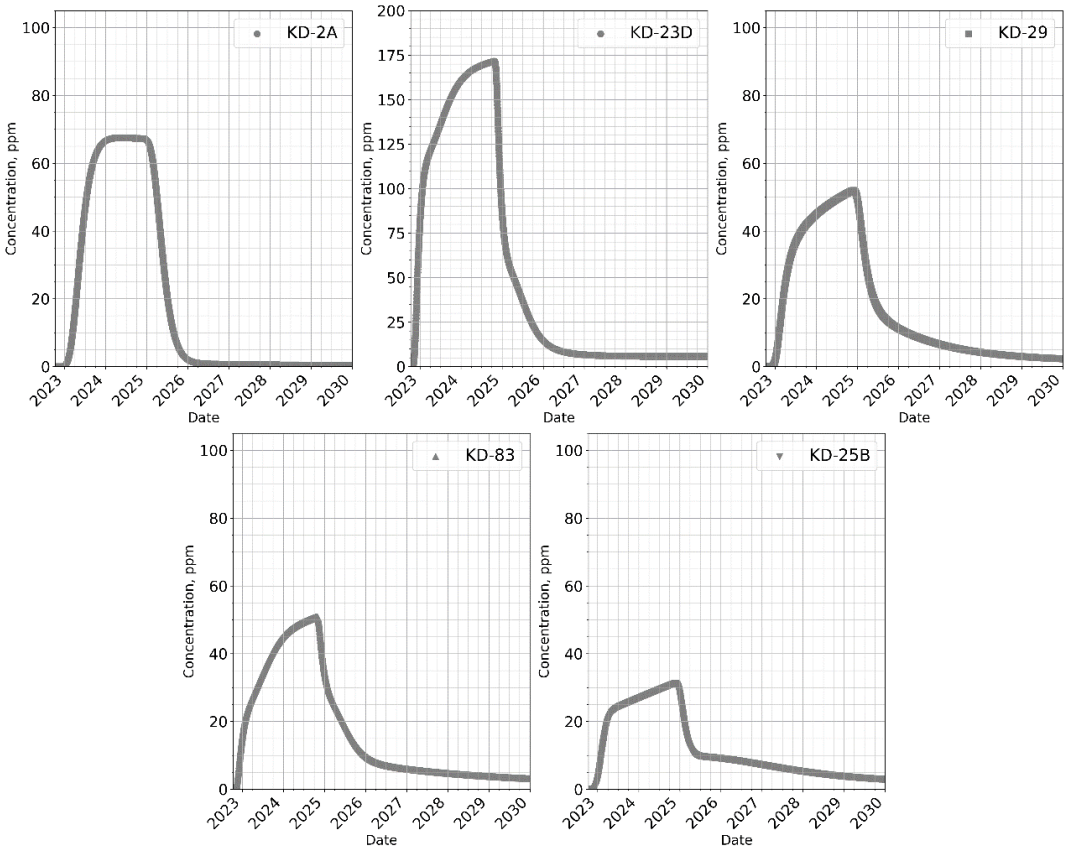

Figure 6-7 CO_2 breakthrough curves for 24 months of 2500 tons/year injection.

As the injection continues, more time is available for the CO_2 to disperse and accumulate in the vicinity of the KD-50A, which creates a small pressure support in the low permeable regions. Simultaneously, the pressure drop occurs along the high permeable flow paths thus, the resulting pressure difference allows the concentration shift from the grid blocks with a high concentration near KD-50A back into the flow paths which resulted in slightly higher recovery factors.

Furthermore, it can be observed that for the maximum time duration of 8 years, the recovery factors seem to be the lowest, however, this is not the case for this injection duration since the numerical model simulates the injection process until 2030 for which the 8 years injection duration continuously injects CO_2 from the well KD-50A without ending the injection. The CO_2 breakthrough curve for this injection duration and all the other scenarios are illustrated in Appendix D.

6.3.2 CO_2 Injection under Constant Pressure Varying Bottom-hole Pressures

The second strategy to observe the impact of CO_2-water injection from the well KD-50A is to approach all of the production wells under constant pressure conditions with various bottom-hole pressure values against declining brine production rates over time using deliverability models. In TOUGH2 v2.0, the mass production rates are calculated by the following formulation of Coats, 1977.

$$q_\beta = \frac{k_{r\beta}}{\mu_\beta}\rho_\beta * PI * (P_\beta - P_{wb}) \qquad (41)$$

where, q_β is the mass flow rate of the flowing phase ß, $k_{r\beta}, \mu_\beta, \rho_\beta$, are the relative permeability, viscosity, and density of the flowing phase and P_β and P_{wb} are the phase pressure and bottom-hole pressure of the flowing phase respectively. In our numerical model, the reservoir fluid and the CO_2-brine mixture always remain under single-phase conditions.

The productivity indexes of the production wells retrieved from the existing well tests are provided in the following table (Table 6-3). Note that the deliverability option is enabled in the numerical model simultaneously with the start of CO_2-brine injection from KD-50A.

Thus, according to the above equation, the $k_{r\beta}, \mu_\beta, \rho_\beta$ of the flowing phase is going to be constant (i.e. for the single-phase CO_2-charged reservoir brine) throughout simulations alongside productivity indexes of the wells. For different configurations of bottom-hole pressures, P_{wb}, the flowing phase pressure are arranged to be constants with declining mass flow rates in the production wells accordingly. In other words, the pressure difference on the right-hand side of the above equation is going to be compensated by the gradual decline of the mass flow rate on the left-hand side of the equation accordingly.

Table 6-3 Productivity Indexes of the wells.

Well ID	*PI (m²)*
KD-2A	$7.954 * 10^{-12}$
KD-23B	$1.978 * 10^{-12}$
KD-23D	$2.926 * 10^{-12}$
KD-29	$2.349 * 10^{-12}$
KD-83	$8.242 * 10^{-12}$
KD-25B	$8.078 * 10^{-12}$

An important consideration is that enabling the deliverability option in the numerical simulation right after the production rate history creates numerical difficulties in the model due to the fact that as the constant production rates go to 0 prior to the calculation of the mass flow rates, a sudden pressure increase has been observed in each of the production well. To resolve this issue, for each scenario in the model, a deliverability model and a constant production flow rate model have been incorporated and the declining flow rates of the wells on deliverability are iteratively calculated. After those flow rates were inputted as flow rate histories to a constant

production flow rate model, the corresponding results were analyzed accordingly. The following figure (Figure 6-8) indicates the constant flow rate history as well as the calculated flow rates after the start of the CO_2-brine injection according to the deliverability model for the 12 months of 2500 tons/year of CO_2-brine injection with +3 bar of bottom-hole pressure case for each production well accordingly.

Distinctive results have been obtained in terms of the CO_2 breakthrough curves of the production wells which are depicted in Figure 6-9 respectively however, although there are variations in terms of total CO_2 recovered from the wells have been obtained, no drastic changes have been observed across the injection scenarios (Table 6-4, Figure 6-11).

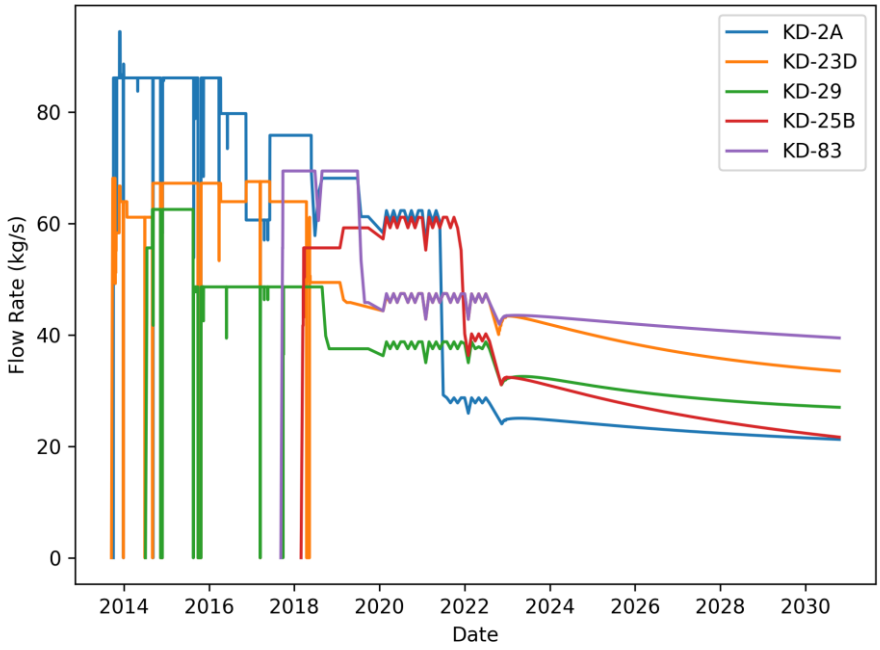

Figure 6-8 Production rates of the wells on deliverability, +3 bar bottom-hole pressure scenario.

At first glance according to the results, a considerable amount of peak CO_2 concentration has arrived at the wells when compared to the 12 months of 2500 tons/year CO_2-brine injection with a constant brine production rate as depicted in Appendix D alongside shorter tailing sections for nearly all of the production wells respectively. Consequently, even though the production rates decline over time, a

slight increase in the total recovered CO_2 amount has been observed. The underlying reason for this occurrence is evident according to the numerical model. In the constant rate scenarios, pressure drop occurs along the flow paths between the injection well, KD-50A, and the surrounding production wells as the majority of the fluid flows through those flow paths.

Table 6-4 Results of the constant pressure CO_2 injection scenarios.

Scenario	*Total Recovered, tons*	*Recovery %*	*KD-2A %*	*KD-23D %*	*KD-83 %*	*KD-25B %*	*KD-29 %*
+6 bar	552.61	22.10%	1.96%	10.75%	4.22%	1.72%	3.45%
+3 bar	546.31	21.85%	2.14%	10.69%	3.86%	1.83%	3.34%
0 bar	536.75	21.47%	2.32%	10.40%	3.64%	1.94%	3.17%
-3 bar	540.04	21.60%	2.46%	10.56%	3.57%	2.07%	2.94%
-6 bar	539.53	21.58%	2.62%	10.54%	3.53%	2.19%	2.70%
Constant Rate	544.41	21.78%	2.41%	10.71%	3.60%	2.15%	2.91%

On the contrary, since the permeability of the surrounding grid blocks is significantly less than the grid blocks along those flow paths, the pressure drop on the surrounding grid blocks is remarkably less which creates a pressure gradient between those surrounding grid blocks and the flow paths. This pressure drop creates a fluid flow from the surrounding grid blocks through the flow paths for which the transported fluid dilutes the CO_2 concentration in the flow paths that in turn, lower concentrations in the breakthrough curves that are observed for the constant rate production scenarios. On the other hand, notably less pressure difference occurs in the constant pressure scenarios, especially for the positive bottom-hole pressure cases for which the effect of dilution is significantly less, however, as the production rates decline over time, the total amount of CO_2 production decreases simultaneously.

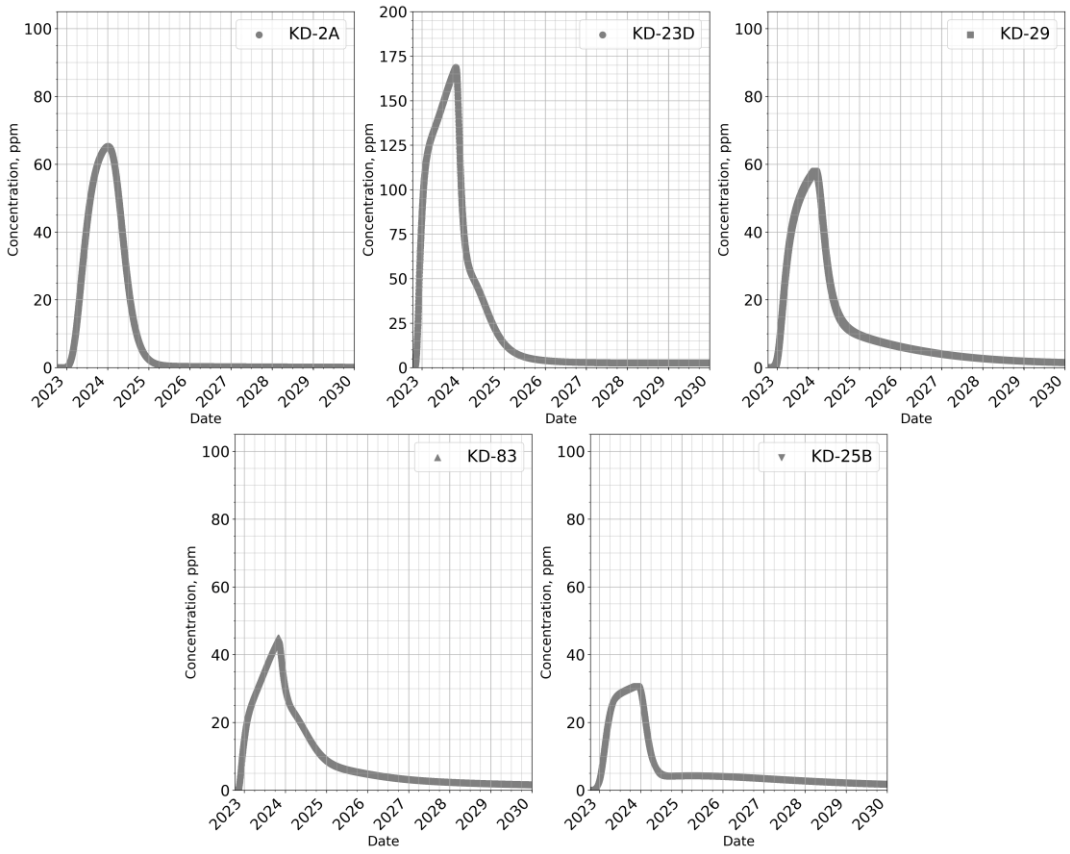

Figure 6-9 CO_2 Breakthrough curves for +3 bar 2500 tons/year of 12 months of injection.

The comparison of the pressure gradients across the flow paths between the wells KD-50A and KD-83 for constant rate injection scenario and +3 bar injection as well as the 12 months of 2500 tons/year with constant production rates scenario for three different instances after the CO_2-brine injection is indicated on Figure 6-10. The combination of those two effects compensates for each other hence, a similar amount of CO_2 production has been observed where a more notable difference has been observed for the +6 bar production scenario (0.3% increase). This relationship exists as the flowing pressure increases, with slight increments in the total beside the +0 bar scenario. Due to the fact that as the pressure decreases, the aforementioned effect of CO_2 arrival concentration diminishes and the peak concentrations in the breakthrough curves are less than the scenarios with the increased bottom-hole pressures (Appendix E). Alongside the effect of decreasing brine production rates,

slightly less amount of CO_2 recoveries is obtained when compared to the constant rate scenario.

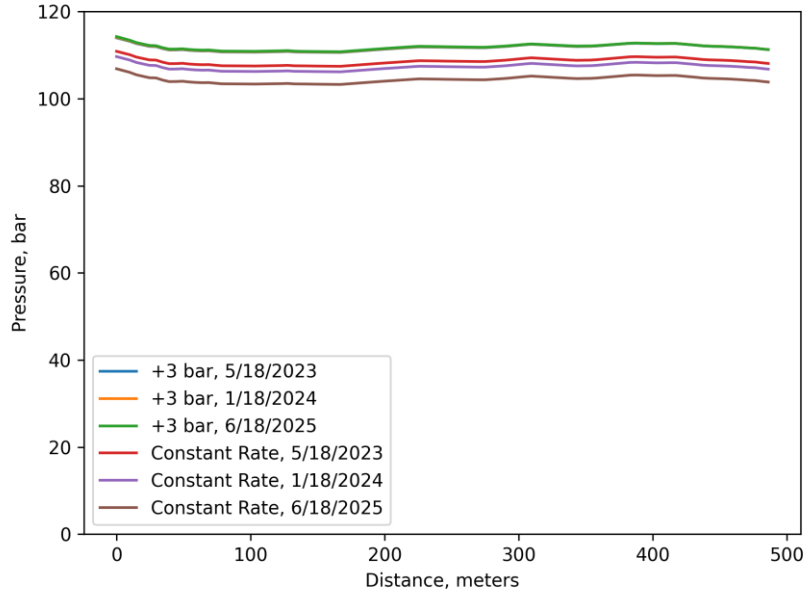

Figure 6-10 Comparison of pressure gradients along the flow path KD-83 and KD-50A for the +3 bar bottom-hole pressure scenario and constant rate scenario.

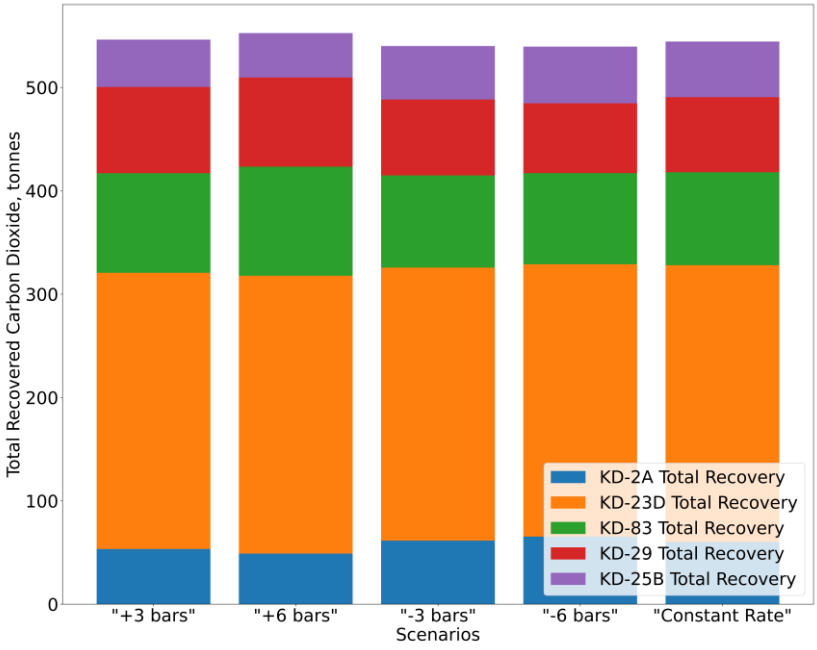

Figure 6-11 Comparison of constant bottom-hole pressure scenarios in terms of total CO_2 recoveries.

6.4 Theoretical Injection Amount of the CO_2 Storage in the Kızıldere Geothermal Field

According to the obtained modeling results of CO_2-brine injection throughout all of the 16 aforementioned scenarios alongside the 2-6-naphthalene-disulphonate slug tracer injection test from the well KD-50A, estimates of CO_2 storage capacity in the Kızıldere Geothermal field can be set through the following expression.

$$M_{CO_2} = SF * RF * \bar{q} * t_i \quad (42)$$

where on the right-hand side of the above expression, M_{CO_2} is the total amount of CO_2 that can be stored whereas, on the right-hand side, RF represents the recovery factor, $\bar{q}$, and t_i are the average injection mass flow rate and duration of CO_2 respectively and SF describes a value between 0 and 1 as a safety factor.

According to the aforementioned scenarios, the deployed strategy in the Kızıldere field has been successful by injecting 2000 tons/year of CO_2 from the well KD-50A for which the results of the numerical model showed that nearly 21.35 % of the injected CO_2 is recovered from the production wells up until 2030. On the other hand, in the Kızıldere field, more than ten wells have been used for the re-injection of the effluent fluid. It is theoretically possible that the CO_2 can be mixed with the effluent fluid like in the case of KD-50A, 2000 tons/year for each injection well. Under these considerations, Table 6-5 represents the total amount of CO_2 that can be stored in the Kızıldere Geothermal field with a range of recovery factors obtained in the injection scenarios as well as with a range of safety factors accordingly alongside the possible minimum and maximum injection capacities by using the existing re-injection wells for a 10-year time span. According to Table 6-5, in 10 years of injection, up to 40 Mt of CO_2 can be stored in the Kızıldere geothermal reservoir even by only injecting a CO_2-brine mixture from the well KD-50A. For this particular case, 40 Mt of CO_2 can be confidently stored in the reservoir for which the safety factor can be taken as 1 since this estimation is proven by the numerical modeling results. Conversely, it is advisable to reduce the safety factor in proportion to the number of wells taken into

CO_2-brine injection, due to the inherent uncertainty surrounding the individual hydraulic conductivities of these wells.

Table 6-5 CO_2 storage potential of the field.

	Capacity	*Injection, 1 y*	*Injection, 5 y*	*Injection, 10 y*
1250 tons/year	x 1	0.97-1.01	4.87-5.04	9.74-10.08
	x 2	1.95-2.02	9.74-10.08	19.48-20.16
	x 4	3.90-4.03	19.48-20.16	38.95-40.31
	x 8	7.79-8.06	38.95-40.31	77.90-80.62
	x 10	9.74-10.08	48.69-50.39	97.38-10.08
2500 tons/year	x 1	1.95-2.02	9.74-10.08	19.48-20.16
	x 2	3.90-4.03	19.48-20.16	38.95-40.31
	x 4	7.79-8.06	38.95-40.31	77.90-80.62
	x 8	15.58-16.13	77.90-80.62	155.80-16.12
	x 10	19.48-20.16	97.38-100.78	194.75-201.55
5000 tons/year	x 1	3.90-4.03	19.48-20.16	38.95-40.31
	x 2	7.80-8.06	38.95-40.31	77.90-80.62
	x 4	15.58-16.12	77.90-80.62	155.80-161.24
	x 8	31.16-32.25	155.80-161.24	311.60-322.48
	x 10	38.95-40.31	194.75-201.55	389.50-403.10

Furthermore, as the number of wells increases, there is a greater likelihood of the injected CO_2-brine mixture migrating to similar locations, resulting in an elevated concentration of CO_2 in specific locations in the reservoir. This, in turn, heightens the risk of the formation of a CO_2 gas plume which could harness the CO_2 storage capacity. However, even with a safety factor as low as 0.5, it could be possible to safely store up to 200 Mt of CO_2 in the Kızıldere reservoir in 10 years of continuous CO_2-brine mixture injection. According to the International Energy Agency (IEA), the average carbon footprint of a person is roughly equal to 4.7 tons/year subsequently, in a 10-year injection operation, over 4250 individuals' carbon footprint can be potentially neutralized.

CHAPTER 7

CONCLUSION AND FUTURE REMARKS

In this study, a predictive reservoir model has been developed for the CO_2-brine mixture injection in one of the pilot demonstration sites for the GECO project, the Kızıldere geothermal field. The simulation procedure has been carried out in a non-isothermal fashion by using TOUGH2 v2.0 assuming no carbonization process takes place in the reservoir according to the existing literature. The developed reservoir model covers a localized boundary centered across the pilot injection well consisting of 10 wells. For model calibration, various data sources have been populated into the model including static PT measurements, chloride contents of the wells, and slug tracer tests conducted from two separate injection wells including the pilot injection well. Firstly, a natural state model has been calibrated to determine the initial conditions of the reservoir model by successfully matching the PT measurements along the completion intervals of the observation wells in a 10% confidence interval. Afterward, to capture the overall hydraulic conductivity between the injectors and the producers in the Kızıldere reservoir, chloride contents have been treated as conservative species in the reservoir and the enrichment of the chloride in the observation wells has been calibrated. It has been concluded that wells KD-2A and KD-23B have a greater degree of connectivity between the injectors compared to wells KD-83, KD-29, and KD-25B. Furthermore, to invert the individual hydraulic parameters of the flow paths in the reservoir, two slug tracer tests conducted from the well KD-93B and the pilot injection well KD-50A have been calibrated to match the first arrival time, mean arrival time, peak tracer concentration and tracer recovery for the injected compounds, alongside, comparison between the numerical model and different analytical models have been incorporated. For the 1-naphthalene-sulphonate tracer test conducted from KD-93B, the model accurately captures the overall flow behavior of the injected tracer with some shortages in the dispersive

transport for the well KD-2A and the tracer recovery of the flow paths for the well KD-83. For the 2-6-naphthalene-disulphonate tracer test conducted from KD-50A, the results display a good representation of the actual flow behavior of the tracer compound except for the well KD-2A. For this particular well, the model cannot capture the low-dispersive and high-velocity of the tracer compound. Lastly, to predict the impact of the CO_2-brine mixture, different injection rates and injection durations are coupled with constant production rates and constant pressure models. The modeling results showed no significant distinctions in terms of total CO_2 recovery which is around 21 %. According to the obtained parameters, potentially, 200 Mt of CO_2 can be stored in the Kızıldere reservoir in 10 years by commencing all of the re-injection wells with 5000 tons/year of CO_2 injection even if a 50 % success rate depending on the uncertain hydraulic connectivities of the re-injection wells.

Furthermore, the developed reservoir model can be used for more comprehensive studies with additional physics involved. As it has been previously indicated in Chapter 6, it has been observed that the injectivity of the pilot injection well has increased significantly. This increase in the injectivity was associated with the dissolution of minerals due to decreased pH of the reinjection fluid. To examine this phenomenon, a transient wellbore simulator can be coupled with the TOUGHREACT sequentially such as T2WELL (Pan et al., 2014). However, the computational burden of simulating the thermo-hydro-chemical coupling is already high with commercial CPUs, coupling those physics with a wellbore simulator would further increase the execution time. Thus, a doublet reservoir model can be a better option by assigning proper flux boundary conditions.

REFERENCES

Akın, S., Şentürk, E., Şengün, R., & Kılınçarslan, S. (2016). Tracer Testing at Kizildere Geothermal Field Turkey Using Naphthalene Sulfonates. https://hdl.handle.net/11511/84774.

Aksu, B. (2019). Structural controls on Kızıldere geothermal field, Denizli-Turkey. (Master's thesis, Middle East Technical University).

Aradóttir ESP, Sonnethal EL, Björnsson G, Johnsson H (2012). Multidimensional reactive transport modeling of CO_2 mineral sequestration in basalts at the Hellisheidi geothermal field, Iceland. International Journal of Greenhouse Gas Control 9: 24-40. https://doi.org/10.1016/j.ijggc.2012.02.006

Aradóttir, E. S. P., Sigurdardóttir, H., Sigfússon, B., & Gunnlaugsson, E. (2011). Carbfix: A CCS pilot project imitating and accelerating natural CO_2 sequestration. Greenhouse Gases: Science and Technology, 1(2), 105–118. https://doi.org/10.1002/ghg.18

Aradóttir, E. S., Sigurdardóttir, H., Sigfússon, B., & Gunnlaugsson, E. (2011). CarbFix: a CCS pilot project imitating and accelerating natural CO_2 sequestration. Greenhouse Gases: Science and Technology, 1(2), 105-118.

Aradóttir, E., Sonnenthal, E., Björnsson, G., Gunnlaugsson, E., Jónsson, H., (2009). Development of a coupled reactive fluid flow model for mineral CO_2 capture in Hellisheidi, Iceland. Proceedings, TOUGH Symposium 2009, Lawrence Berkeley National Laboratory, Berkeley, CA, September 14–16.

Aradóttir, E.S.P., (2010) Carbfix Reservoir Model – Hydrological Parameters and Pumping Schemes for Experimental CO_2 Injection. Report 2010-03. Reykjavík.

Bachu, S., Gunter, W. D., & Perkins, E. H. (1994). Aquifer disposal of CO_2: Hydrodynamic and mineral trapping. Energy Conversion and Management, 35(4), 269–279. https://doi.org/10.1016/0196-8904(94)90060-4

Bertani, R., and Thain, I. (2002). Geothermal power generating plant CO_2 emission survey. IGA News, 49, 1-3.

Bozkurt, E., & Oberhänsli, R. (2001). Menderes Massif (western turkey): Structural, metamorphic and magmatic evolution - A synthesis. International Journal of Earth Sciences, 89(4), 679–708. https://doi.org/10.1007/s005310000173

Bullivant, D.P., O'Sullivan, M.J., 1989. Matching a field tracer test with some simple models. Water Resources Research 25 (8), 1879–1891.

Bundschuh, Jochen & Suárez-Arriaga, Mario-César. (2010). Introduction to the Numerical Modeling of Groundwater and Geothermal Systems: Fundamentals of Mass, Energy and Solute Transport in Poroelastic Rocks. 10.1201/b10499.

Caesar, L., McCarthy, G. D., Thornalley, D. J. R., and Rahmstorf, S. (2021). Current Atlantic Meridional Overturning Circulation weakest in last millennium. Nat. Geosci. 14, 118–120. doi: 10.1038/s41561-021-00699-z

Ciavarella, A., Cotterill, D., Stott, P., Kew, S., Philip, S., van Oldenborgh, G. J., Skålevåg, A., Lorenz, P., Robin, Y., Otto, F., Hauser, M., Seneviratne, S. I., Lehner, F., & Zolina, O. (2021). Prolonged siberian heat of 2020 almost impossible without human influence. Climatic Change, 166(1–2). https://doi.org/10.1007/s10584-021-03052-w

Cihan, A., & Tyner, J. S. (2011). 2-D radial analytical solutions for solute transport in a dual-porosity medium. Water Resources Research, 47(4). https://doi.org/10.1029/2009wr008969

Clark, D. E., Oelkers, E. H., Gunnarsson, I., Sigfússon, B., Snæbjörnsdóttir, S. Ó., Aradóttir, E. S., & Gíslason, S. R. (2020). Carbfix2: CO_2 and H2s mineralization during 3.5 years of continuous injection into basaltic rocks at more than 250 °C. Geochimica Et Cosmochimica Acta, 279, 45–66. https://doi.org/10.1016/j.gca.2020.03.039

Coats, K.H. (1977) Geothermal Reservoir Modeling, presented at the 52nd Annual Fall Technical Conference and Exhibition of the SPE, Denver, Colorado, paper SPE-6892.

Computer Modeling Group (2007): CMG STARS User's Guide. Computer Modeling Group LTD.

Dickson, M.H. and Fanelli, M.,1995, Geothermal Energy, Unesco Energy Engineering Series, John Wiley & Sons, New York.

Diersch, H.-J. G. (2014). FEFLOW. https://doi.org/10.1007/978-3-642-38739-5

Edlefsen, N. E., & Anderson, B. C. (1943). Thermodynamics of Soil Moisture. HILGARDIA, 15(2).

Ellsworth, T. R., & Butters, G. L. (1993). Three-dimensional analytical solutions to the advection-dispersion equation in arbitrary Cartesian coordinates. Water Resources Research, 29(9), 3215–3225. https://doi.org/10.1029/93wr01293

Ennis-King, J., & Paterson, L. (2005). Role of convective mixing in the long-term storage of carbon dioxide in deep saline formations. SPE Journal, 10(03), 349–356. https://doi.org/10.2118/84344-pa

Ercan, T. (1979) Bati Anadolu, Trakya ve Ege adalarmdaki Senozoyik volkanizmas). Jeolojii Müh. Odası. Yayini, sayi 9, Ankara.

Ercan, T. (1981) Kula yöresinin jeoloji ve volkanitlerinin petrolojisi, (PhD Thesis), I.U. Earth Sciences Faculty, 165 pp

Erol, S., Akın, T., & Akın, S. (2023). Update for reactive transport modeling of the Kızıldere geothermal field to reduce uncertainties in the early inspections. Turkish Journal of Earth Sciences, 32(4), 541–554. https://doi.org/10.55730/1300-0985.1860

Erol, S., Akın, T., Başer, A., Saraçoğlu, Ö. & Akın, S. (2022). Fluid-CO_2 Injection Impact in a geothermal reservoir: Evaluation with 3- D reactive transport modeling. Geothermics, 98, 102271. https://doi.org/10.1016/j.geothermics.2021.102271

Erol, S., Bayer, P., Akın, T., & Akın, S. (2022). Advanced workflow for multi-well Tracer test analysis in a Geothermal Reservoir. Geothermics, 101, 102375. https://doi.org/10.1016/j.geothermics.2022.102375

Falta, R. W., Pruess, K., Finsterle, S., & Battistelli, A. (1995). T2VOC User's Guide.

Flett, M., Gurton, R., and Ian T. (2004). The Function of Gas-Water Relative Permeability Hysteresis in the Sequestration of Carbon Dioxide in Saline Formations. Paper presented at the SPE Asia Pacific Oil and Gas Conference and Exhibition, Perth, Australia. doi: https://doi.org/10.2118/88485-MS

Fossum, M.P., Horne, R.N., 1982. Interpretation of tracer return profiles at Wairakei geothermal field using fracture analysis. Geothermal Resources Council, Transactions 6, 261–264.

Franzson, H. (2000). Hydrothermal evolution of the Nesjavellir high-temperature system, Iceland. In Proceedings of the World Geothermal Congress 2000, Kyushu-Tohoku, Japan (pp. 2075-2080).

GECO (2020). Report: Deliverable 2.9 Report on Integrated Geological and Reservoir Models and Injection Modelling. https://geco-h2020.eu/deliverables/

GECO (2023). Report: Deliverable 7.4 Report on Models updated and processes optimized in the light of the first results (in the preparation process). https://geco-h2020.eu/deliverables/

Gislason, S. R., Wolff-Boenisch, D., Stefansson, A., Oelkers, E. H., Gunnlaugsson, E., Sigurdardottir, H., Sigfusson, B., Broecker, W. S., Matter, J. M., & Stute, M. (2010). Mineral sequestration of carbon dioxide in basalt: A pre-injection overview of the CarbFix Project. International Journal of Greenhouse Gas Control, 4(3), 537–545. https://doi.org/10.1016/j.ijggc.2009.11.013

Gíslason, S. R., Sigurdardóttir, H., Aradóttir, E. S., & Oelkers, E. H. (2018). A brief history of carbfix: Challenges and victories of the project's pilot phase. Energy Procedia, 146, 103–114. https://doi.org/10.1016/j.egypro.2018.07.014

Gunnarsson I, Aradóttir ES, Oelkers EH, Clark DE, Arnarson MÞ et al. (2018). The rapid and cost-effective capture and subsurface mineral storage of carbon and sulfur at the

CarbFix2 site. International Journal of Greenhouse Gas Control 79: 117-126. https://doi.org/10.1016/j.ijggc.2018.08.014

Gunter, W. D., Perkins, E. H., & McCann, T. J. (1993). Aquifer disposal of CO_2-rich gases: Reaction design for added capacity. Energy Conversion and Management, 34(9–11), 941–948. https://doi.org/10.1016/0196-8904(93)90040-h

Haizlip, J.R., Haklidir, F.T., Garg, S.K., (2013). Comparison of reservoir conditions in high noncondensible gas geothermal systems. PROCEEDINGS, 38th Workshop on Geothermal Reservoir Engineering Stanford University, Stanford, California, February 11-13, 2013 SGP-TR-198

Herrera Martinez, A., Groenenberg, H., Noothout, P., Koornneef J., Baloğlu, T., Rencberoğlu, G., Ozbulak, O., and Akın, S. (2016). Assessing the use of CO_2 from natural sources for commercial purposes in Turkey, EBRD Report.

Holtz, M. H. (2002). Residual gas saturation to aquifer influx: A calculation method for 3-D Computer Reservoir Model Construction. All Days. https://doi.org/10.2118/75502-ms

Houseworth, J. E., Asahina, D., & Birkholzer, J. T. (2013). An analytical model for solute transport through a water-saturated single fracture and Permeable Rock Matrix. Water Resources Research, 49(10), 6317–6338. https://doi.org/10.1002/wrcr.20497

How it works. Carbfix. (n.d.). https://www.carbfix.com/how-it-works/

IPCC, 2014: Climate Change 2014: Synthesis Report. Contribution of Working Groups I, II and III to the Fifth Assessment Report of the Intergovernmental Panel on Climate Change [Core Writing Team, R.K. Pachauri and L.A. Meyer (eds.)]. IPCC, Geneva, Switzerland, 151 pp.

IPCC, 2021: Climate Change 2021: The Physical Science Basis. Contribution of Working Group I to the Sixth Assessment Report of the Intergovernmental Panel on Climate Change[Masson-Delmotte, V., P. Zhai, A. Pirani, S.L. Connors, C. Péan, S. Berger, N. Caud, Y. Chen, L. Goldfarb, M.I. Gomis, M. Huang, K. Leitzell, E. Lonnoy,

J.B.R. Matthews, T.K. Maycock, T. Waterfield, O. Yelekçi, R. Yu, and B. Zhou (eds.)]. Cambridge University Press, Cambridge, United Kingdom and New York, NY, USA, In press, doi:10.1017/9781009157896.

IRENA and IGA (2023), Global geothermal market and technology assessment, International Renewable Energy Agency, Abu Dhabi; International Geothermal Association, The Hague.

Juanes, R., Spiteri, E. J., Orr, F. M., & Blunt, M. J. (2006). Impact of relative permeability hysteresis on geological CO_2 storage. Water Resources Research, 42(12). https://doi.org/10.1029/2005wr004806

Karamanderesi, İ. (2013). Characteristics of Geothermal Reservoirs in Turkey. In IGA Academy Report 0102-2013.

Kelemen, P., Benson, S. M., Pilorgé, H., Psarras, P., & Wilcox, J. (2019). An overview of the status and challenges of CO_2 Storage in Minerals and Geological Formations. Frontiers in Climate, 1. https://doi.org/10.3389/fclim.2019.00009

Kissling, W. M., Brown, K. L., O'Sullivan, M. J., White, S. P., & Bullivant, D. P. (1996). Modelling chloride and CO_2 Chemistry in the Wairakei Geothermal Reservoir. Geothermics, 25(3), 285–305. https://doi.org/10.1016/0375-6505 (96)00009-0

Krevor, S., Blunt, M. J., Benson, S. M., Pentland, C. H., Reynolds, C., Al-Menhali, A., & Niu, B. (2015). Capillary trapping for geologic carbon dioxide storage – from pore scale physics to field scale implications. International Journal of Greenhouse Gas Control, 40, 221–237. https://doi.org/10.1016/j.ijggc.2015.04.006

Kristjánsson B.R., G. Axelsson, G. Gunnarsson, I. Gunnarsson, and F. Óskarsson.: Comprehensive Tracer Testing in the Hellisheiði Geothermal Field in SW-Iceland, Proceedings, 41st Workshop on Geothermal Reservoir Engineering, Stanford, California (2016).

Küçük, S. (2018). Simulation of geothermal reservoirs with high amount of carbon dioxide (Master's thesis, Middle East Technical University).

MacFarling Meure, C., Etheridge, D., Trudinger, C., Steele, P., Langenfelds, R., van Ommen, T., Smith, A., & Elkins, J. (2006). Law Dome CO_2, CH_4, and N_2O ice core records extended to 2000 years BP. Geophysical Research Letters, 33(14). https://doi.org/10.1029/2006gl026152

Matter, J. M., Stute, M., Snæbjörnsdottir, S., Oelkers, E. H., Gislason, S. R., Aradottir, E. S., Sigfusson, B., Gunnarsson, I., Sigurdardottir, H., Gunnlaugsson, E., Axelsson, G., Alfredsson, H. A., Wolff-Boenisch, D., Mesfin, K., Taya, D. F., Hall, J., Dideriksen, K., & Broecker, W. S. (2016). Rapid carbon mineralization for permanent disposal of anthropogenic carbon dioxide emissions. Science, 352(6291), 1312–1314. https://doi.org/10.1126/science.aad8132

Narasimhan, T. N., & Witherspoon, P. A. (1976). An integrated finite difference method for analyzing fluid flow in porous media. Water Resour. Res., 12(1), 57–64. https://doi.org/10.1029/WR012i001p00057

Nelder, J. A., & Mead, R. (1965). A simplex method for function minimization. The Computer Journal, 7(4), 308–313. https://doi.org/10.1093/comjnl/7.4.308

O'Sullivan, M. J., Bodvarsson, G. S., Pruess, K., & Blakeley, M. R. (1985). Fluid and Heat Flow In Gas-Rich Geothermal Reservoirs. Society of Petroleum Engineers Journal (Vol. 25).

Oelkers, E. H., Gislason, S. R., & Matter, J. (2008). Mineral carbonation of CO_2. Elements, 4(5), 333–337. https://doi.org/10.2113/gselements.4.5.333

Pan, L., & Oldenburg, C. M. (2014). T2well—an integrated wellbore–reservoir simulator. *Computers & Geosciences*, *65*, 46–55. https://doi.org/10.1016/j.cageo.2013.06.005

Pogge von Strandmann, P. A., Burton, K. W., Snæbjörnsdóttir, S. O., Sigfússon, B., Aradóttir, E. S., Gunnarsson, I., Alfredsson, H. A., Mesfin, K. G., Oelkers, E. H., & Gislason, S. R. (2019). Rapid CO_2 mineralisation into calcite at the CarbFix storage site quantified using calcium isotopes. Nature Communications, 10(1). https://doi.org/10.1038/s41467-019-10003-8

Pruess, K. (1987). TOUGH User's Guide.

Pruess, K. (2003). The TOUGH Codes—A Family of Simulation Tools for Multiphase Flow and Transport Processes in Permeable Media. Vadose Zone Journal, 3(3), 738– 746. https://doi.org/10.2136/vzj2004.0738

Pruess, K., Oldenburg, C., & Moridis, G. (1999). TOUGH2 User's Guide, Version 2.0

Ratouis, T. M. P., Snæbjörnsdóttir, S. Ó., Voigt, M. J., Sigfússon, B., Gunnarsson, G., Aradóttir, E. S., & Hjörleifsdóttir, V. (2022). Carbfix 2: A transport model of long-term CO_2 and H_2S injection into basaltic rocks at Hellisheidi, SW-Iceland. International Journal of Greenhouse Gas Control, 114, 103586. https://doi.org/10.1016/j.ijggc.2022.103586

Ratouis, T.M.P., Snæbjörnsdóttir, S.O., Gunnarsson, G., Gunnarsson, I., Kristjánsson, B.R., Aradóttir, E.S.P., (2019). Modelling the Complex Structural Features Controlling Fluid Flow at the CarbFix2 Reinjection Site, Hellisheiði Geothermal Power Plant, SW-Iceland. PROCEEDINGS, 44th Workshop on Geothermal Reservoir Engineering Stanford University, Stanford, California, February 11-13, 2019 SGP-TR-214

Rezvani Khalilabad, M., Axelsson, G., & Gislason, S. R. (2008). Aquifer characterization with Tracer Test Technique; permanent CO_2 Sequestration into basalt, SW Iceland. Mineralogical Magazine, 72(1), 121–125. https://doi.org/10.1180/minmag.2008.072.1.121

Rose, P.E., Benoit, W.R., and Kilbourn, P.M., (2001), The application of the polyaromatic sulfonates as tracers in geothermal reservoirs: Geothermics, 30(6), pp. 617-640.

Rose, P.E. and Clausen, S. (2017) "The Use of Amino-Substituted Naphthalene Sulfonates as Tracers in Geothermal Reservoirs" Proceedings, 42nd Workshop on Geothermal Reservoir Engineering Stanford University, Stanford, California, February 13-15, SGP-TR-212

Rose, P.E., Johnson, S.D., Kilbourn, P.M., and Kasteler, C. (2002) Tracer Testing at Dixie Valley, Nevada Using 1-Naphthalene Sulfonate and 2,6-Naphthalene Disulfonate: Proc. Twenty-Seventh Workshop on Geothermal Reservoir Engineering, Stanford University, SGP-TR-171.

Sauty, J.P., 1980. An analysis of hydrodispersive transfer in aquifers. Water Resources Research 16 (1), 145–158.

Şengör, A. C., & Yilmaz, Y. (1981). Tethyan evolution of Turkey: a plate tectonic approach. Tectonophysics, 75(3-4), 181-241.

Sevindik, D.B., Erol, S., Akın, T., Akın, S., (2023). Modeling of Chloride and Carbon Dioxide Injection at Kızıldere Geothermal Field. PROCEEDINGS, 48th Workshop on Geothermal Reservoir Engineering Stanford University, Stanford, California, February 6-8, 2023 SGP-TR-224.

Şimsek, Ş. (1984). Denizli, Kizildere -Tekkehamam -Tosunlar - Buldan - Yenice Alanının Jeolojisi Ve Jeotermal Enerji Olanakları. Maden Tetkik ve Arama Genel Müdürlüğü Raporu No:7846, 85s. Ankara

Şimşek, Ş. (1985a). Geothermal model of Denizli - Sarayköy - Buldan area. Geothermics, 14(2–3), 393–417.

Şimşek, Ş. (1985b). Present Status and Future Developments of the Denizli-Kizildere Geothermal Field of Turkey. In International Symposium on Geothermal Energy. International volume. pp.203-215 Hawaii.

Simsek, S., (2003) Hydrogeological and isotopic survey of geothermal fields in the Buyuk Menderes graben, Turkey. Geothermics 32, 669-678.

Şimşek, Ş., Parlaktuna, M., & Akin, S. (2009). Data Gathering and Evaluation of Kızıldere Geothermal Field.

Şimşek, Ş., Yıldırım, N., & Gülgör, A. (2005). Developmental and environmental effects of the Kızıldere Geothermal Power Project, Turkey. Geothermics, 34(2), 234–251. https://doi.org/10.1016/j.geothermics.2004.12.005

Snæbjörnsdóttir SÓ, Gislason SR, Galeczka IM, Oelkers EH (2018). Reaction path modeling of in-situ mineralization of CO_2 at the CarbFix site at Hellisheidi, SW-Iceland. Geochimica et Cosmochimica Acta 220: 348–366. https://doi.org/10.1016/j.gca.2017.09.053

Snæbjörnsdóttir, S., Oelkers, E. H., Mesfin, K., Aradóttir, E. S., Dideriksen, K., Gunnarsson, I., Gunnlaugsson, E., Matter, J. M., Stute, M., & Gislason, S. R. (2017). The chemistry and saturation states of subsurface fluids during the in situ mineralization of CO_2 and H_2S at the CarbFix site in SW-Iceland. International Journal of Greenhouse Gas Control, 58, 87–102. https://doi.org/10.1016/j.ijggc.2017.01.007

Snæbjörnsdóttir, S., Sigfússon, B., Marieni, C., Goldberg, D., Gislason, S. R., & Oelkers, E. H. (2020). Carbon dioxide storage through mineral carbonation. Nature Reviews Earth &Environment, 1(2), 90–102. https://doi.org/10.1038/s43017-019-0011-8

Tezcan, A. K. (1979) Geothermal Studies, Their Present Status and Contribution to Heat Flow Contouring in Turkey. Springer, Berlin.

Tómasdóttir S. (2018) "Flow Paths in the Húsmúli Reinjection Zone, Iceland" MSc thesis, Uppsala University.

Torp, T.A. and Gale, J. (2004) Demonstrating Storage of CO_2 in Geological Reservoirs: The Sleipner and SACS Projects. Energy, 29, 1361-1369. http://dx.doi.org/10.1016/j.energy.2004.03.104

Tut Haklıdır, F. S., Şengün, R., & Aydın, H. (2021). Characterization and comparison of geothermal fluids geochemistry within the KIZILDERE geothermal field in Turkey: New findings with power capacity expanding studies. Geothermics, 94, 102110. https://doi.org/10.1016/j.geothermics.2021.102110

Van Genuchten, M. T. (1982). Analytical solutions of the one-dimensional convective-dispersive solute transport equation (No. 1661). US Department of Agriculture, Agricultural Research Service.

WMO, Greenhouse Gas Bulletin No. 17, (2021). ISSN 2078-0796.

A. Appendix A – Python Code for the Analytical Models

```
import numpy as np
import pandas as pd
from scipy.optimize import minimize
import math
def single_fracture(data_file, sheet_name, params_initial, bounds, delta_range, delta_step,q,R):
    # Load experimental data
    data = pd.read_excel(data_file, sheet_name=sheet_name)
    x_data = data.iloc[:, 3].values
    y_data = data.iloc[:, 1].values
    # Define the analytical model function
    def model(t, params):
        w, L, tm = params
        return L/np.sqrt(t)*2*tm/t*np.exp(-w/4*(t-tm)**2/(t*tm))
    # Define the objective function to be minimized
    def objective(params, x, y, delta=1):
        y_model = model(x, params)
        residual = y - y_model
        return np.mean(np.log(1 + (residual / delta) ** 2))
```

```
# Define the initial guess for the parameters
params_initial = params_initial
# Define the order in which to optimize the parameters
params_order = [i for i in range(len(params_initial))]
# Perform the optimization for each delta value
results = []
sses = []
for delta in delta_range:
    params_optimized = params_initial.copy()
    for i in params_order:
        result = minimize(objective, params_optimized, args=(x_data, y_data, delta),
                          bounds=bounds, method="Nelder-Mead")
        params_optimized = result.x
    # Record the optimized parameters and SSE for this delta value
    results.append(result.x)
    y_model = model(x_data, result.x)
    sse = np.sum((y_data - y_model) ** 2)
    sses.append(sse)
# Find the index of the delta value with the lowest SSE
best_delta_index = np.argmin(sses)
# Generate model predictions using the optimized parameters
best_params = results[best_delta_index]
```

```
    y_model = model(x_data, best_params)
    sse = sses[best_delta_index]
    # Generate an extended model for plotting
    x_ext = np.arange(0, 200, 1)
    extended_model = model(x_ext, best_params)
    m = 4*best_params[1]*q*(math.pi*best_params[2]/best_params[0])**0.5
    taylor_dispersivity = R**2/(best_params[0]*best_params[2])
    u = R/best_params[2]
    parameter_dictionary = {"w":best_params[0], "L":best_params[1], "tm":
        best_params[2]}
    derived_parameters = {"m" : m, "Taylor Dispersivity": taylor_dispersivity, "u": u }
    return best_params, sse, x_ext, extended_model, parameter_dictionary,
        derived_parameters
def multi_fracture(data_file, sheet_name, params_initial, bounds, delta_range, delta_step,q,
        R):
    # Load experimental data
    data = pd.read_excel(data_file, sheet_name=sheet_name)
    x_data = data.iloc[:, 3].values
    y_data = data.iloc[:, 1].values
    # Define the analytical model function
    def model(t, params):
        w1, L1, tm1, w2, L2, tm2, w3, L3, tm3, e1, e2, e3 = params
        return (L1 / np.sqrt(t) * 2 * tm1 / t * np.exp(-w1 / 4 * (t - tm1) ** 2 / (t * tm1))) * e1 \
```

```
        + (L2 / np.sqrt(t) * 2 * tm2 / t * np.exp(-w2 / 4 * (t - tm2) ** 2 / (t * tm2))) * e2 \
        + (L3 / np.sqrt(t) * 2 * tm3 / t * np.exp(-w3 / 4 * (t - tm3) ** 2 / (t * tm3))) * e3
# Define the objective function to be minimized
# Define the objective function to be minimized
def objective(params, x, y, delta=1):
    y_model = model(x, params)
    residual = y - y_model
    return np.mean(np.log(1 + (residual / delta) ** 2))
# Define the constraint function
def constraint(params):
    return np.sum(params[-1] + params[-2] + params[-3]) - 1
# Define the constraint object
cons = {'type': 'eq', 'fun': constraint}
# Define the initial guess for the parameters
params_initial = params_initial
# Define the initial guess for the parameters
params_initial = params_initial
# Define the order in which to optimize the parameters
params_order = [i for i in range(len(params_initial))]
# Perform the optimization for each delta value
results = []
sses = []
```

```
for delta in delta_range:
    params_optimized = params_initial.copy()
    for i in params_order:
        result = minimize(objective, params_optimized, args=(x_data, y_data, delta),
                          bounds=bounds, method="SLSQP", constraints=cons)
        params_optimized = result.x
    # Record the optimized parameters and SSE for this delta value
    results.append(result.x)
    y_model = model(x_data, result.x)
    sse = np.sum((y_data - y_model) ** 2)
    sses.append(sse)
# Find the index of the delta value with the lowest SSE
best_delta_index = np.argmin(sses)
# Generate model predictions using the optimized parameters
best_params = results[best_delta_index]
y_model = model(x_data, best_params)
sse = sses[best_delta_index]
# Generate an extended model for plotting
x_ext = np.arange(0, 200, 1)
extended_model = model(x_ext, best_params)
m1 = 4*best_params[1]*q*(math.pi*best_params[2]/best_params[0])**0.5
m2 = 4*best_params[4]*q*(math.pi*best_params[5]/best_params[3])**0.5
```

```
    m3 = 4*best_params[7]*q*(math.pi*best_params[8]/best_params[6])**0.5
    d1 = R**2/(best_params[0]*best_params[2])
    d2 = R**2/(best_params[3]*best_params[5])
    d3 = R**2/(best_params[6]*best_params[8])
    u1 = R/best_params[2]
    u2 = R/best_params[5]
    u3 = R/best_params[8]
    parameter_dictionary = {"w1":
        best_params[0],"L1":best_params[1],"tm1":best_params[2],"w2":best_params[3],"
        L2":best_params[4],"tm2":best_params[5],"w3":best_params[6],"L3":best_params
        [7],"tm3":best_params[8],"e1":best_params[9],"e2":best_params[10],"e3":best_par
        ams[11]}
    derived_parameters =
        {"m1":m1,"m2":m2,"m3":m3,"d1":d1,"d2":d2,"d3":d3,"u1":u1,"u2":u2,"u3":u3}
    return best_params, sse, x_ext, extended_model, parameter_dictionary,
        derived_parameters
def fracture_matrix(data_file, sheet_name, params_initial, bounds, delta_range,
        delta_step,q):
    # Load experimental data
    data = pd.read_excel(data_file, sheet_name=sheet_name)
    x_data = data.iloc[:, 3].values
    y_data = data.iloc[:, 1].values
    # Define the analytical model function
    def model(t, params):
```

```
    w, tb, L = params
    return np. where(t>tb,L/(t-tb)**1.5*np.exp(-tb/(w*(t-tb))),0)
# Define the objective function to be minimized
def objective(params, x, y, delta=1):
    y_model = model(x, params)
    residual = y - y_model
    return np.mean(np.log(1 + (residual / delta) ** 2))
# Define the initial guess for the parameters
params_initial = params_initial
# Define the order in which to optimize the parameters
params_order = [i for i in range(len(params_initial))]
# Perform the optimization for each delta value
results = []
sses = []
for delta in delta_range:
    params_optimized = params_initial.copy()
    for i in params_order:
        result = minimize(objective, params_optimized, args=(x_data, y_data, delta),
                          bounds=bounds, method="Powell")
        params_optimized = result.x
    # Record the optimized parameters and SSE for this delta value
    results.append(result.x)
```

```
        y_model = model(x_data, result.x)
        sse = np.sum((y_data - y_model) ** 2)
        sses.append(sse)
    # Find the index of the delta value with the lowest SSE
    best_delta_index = np.argmin(sses)
    # Generate model predictions using the optimized parameters
    best_params = results[best_delta_index]
    y_model = model(x_data, best_params)
    sse = sses[best_delta_index]
    # Generate an extended model for plotting
    x_ext = np.arange(0, 200, 1)
    extended_model = model(x_ext, best_params)
    m = best_params[2]*q*np.sqrt(math.pi*best_params[0]/best_params[1])
    parameter_dictionary = {"w": best_params[0],"tb": best_params[1],"L": best_params[2]}
    derived_parameters = {"m":m}
    return best_params, sse, x_ext,
        extended_model,parameter_dictionary,derived_parameters
def homogenous_1D(max_conc,data_file, sheet_name, params_initial, bounds, delta_range,
        delta_step,R):
    # Load experimental data
    data = pd.read_excel(data_file, sheet_name=sheet_name)
    x_data = data.iloc[:, 3].values
    y_data = data.iloc[:, 1].values
```

```
# Define the analytical model function
def model(t, params):
    peclet,residence = params
    trm = np.sqrt(1+(1/peclet)**2)-1/peclet
    k = np.sqrt(trm)*np.exp(peclet/(4*trm)*(1-trm)**2)
    tr = t/residence
    conc = k/np.sqrt(tr)*np.exp(-peclet/(4*tr)*(1-tr)**2)*max_conc
    return conc
# Define the objective function to be minimized
def objective(params, x, y, delta=1):
    y_model = model(x, params)
    residual = y - y_model
    return np.mean(np.log(1 + (residual / delta) ** 2))
# Define the initial guess for the parameters
params_initial = params_initial
# Define the order in which to optimize the parameters
params_order = [i for i in range(len(params_initial))]
# Perform the optimization for each delta value
results = []
sses = []
for delta in delta_range:
    params_optimized = params_initial.copy()
```

```
    for i in params_order:
        result = minimize(objective, params_optimized, args=(x_data, y_data, delta),
                          bounds=bounds, method="SLSQP")
        params_optimized = result.x
    # Record the optimized parameters and SSE for this delta value
    results.append(result.x)
    y_model = model(x_data, result.x)
    sse = np.sum((y_data - y_model) ** 2)
    sses.append(sse)
# Find the index of the delta value with the lowest SSE
best_delta_index = np.argmin(sses)
# Generate model predictions using the optimized parameters
best_params = results[best_delta_index]
y_model = model(x_data, best_params)
sse = sses[best_delta_index]
# Generate an extended model for plotting
x_ext = np.arange(0, 200, 1)
extended_model = model(x_ext, best_params)
alpha = R/best_params[0]
Vb = R/best_params[1]
Dl = alpha*Vb
```

```
    parameter_dictionary = {"Pe":best_params[0], "Residence Time": best_params[1]}
    derived_parameters = {"alpha": alpha, "Vb": Vb,"Dl": Dl}
    return best_params, sse, x_ext, extended_model, parameter_dictionary,
        derived_parameters
def homogenous_2D(max_conc,data_file, sheet_name, params_initial, bounds, delta_range,
        delta_step, R):
    # Load experimental data
    data = pd.read_excel(data_file, sheet_name=sheet_name)
    x_data = data.iloc[:, 3].values
    y_data = data.iloc[:, 1].values
    # Define the analytical model function
    def model(t, params):
        peclet, residence = params
        trm = np.sqrt(1+4*(1/peclet)**2)-2/peclet
        k = trm*np.exp(peclet/(4*peclet)*(1-peclet)**2)
        tr = t/residence
        conc = k/tr*np.exp(-peclet/(4*tr)*(1-tr)**2)*max_conc
        return conc
    # Define the objective function to be minimized
    def objective(params, x, y, delta=1):
        y_model = model(x, params)
        residual = y - y_model
        return np.mean(np.log(1 + (residual / delta) ** 2))
```

```
# Define the initial guess for the parameters
params_initial = params_initial
# Define the order in which to optimize the parameters
params_order = [i for i in range(len(params_initial))]
# Perform the optimization for each delta value
results = []
sses = []
for delta in delta_range:
    params_optimized = params_initial.copy()
    for i in params_order:
        result = minimize(objective, params_optimized, args=(x_data, y_data, delta),
                          bounds=bounds, method="Nelder-Mead")
        params_optimized = result.x
    # Record the optimized parameters and SSE for this delta value
    results.append(result.x)
    y_model = model(x_data, result.x)
    sse = np.sum((y_data - y_model) ** 2)
    sses.append(sse)
# Find the index of the delta value with the lowest SSE
best_delta_index = np.argmin(sses)
# Generate model predictions using the optimized parameters
best_params = results[best_delta_index]
```

```
y_model = model(x_data, best_params)

sse = sses[best_delta_index]

# Generate an extended model for plotting

x_ext = np.arange(0, 200, 1)

extended_model = model(x_ext, best_params)

alpha = R/best_params[0]

Vb = R/best_params[1]

Dl = alpha*Vb

parameter_dictionary = {"Pe":best_params[0], "Residence Time": best_params[1]}

derived_parameters = {"alpha": alpha, "Vb": Vb,"Dl": Dl}

return best_params, sse, x_ext, extended_model, parameter_dictionary,
    derived_parameters
```

B. Appendix B – Results of the Analytical Models for the well KD-93B

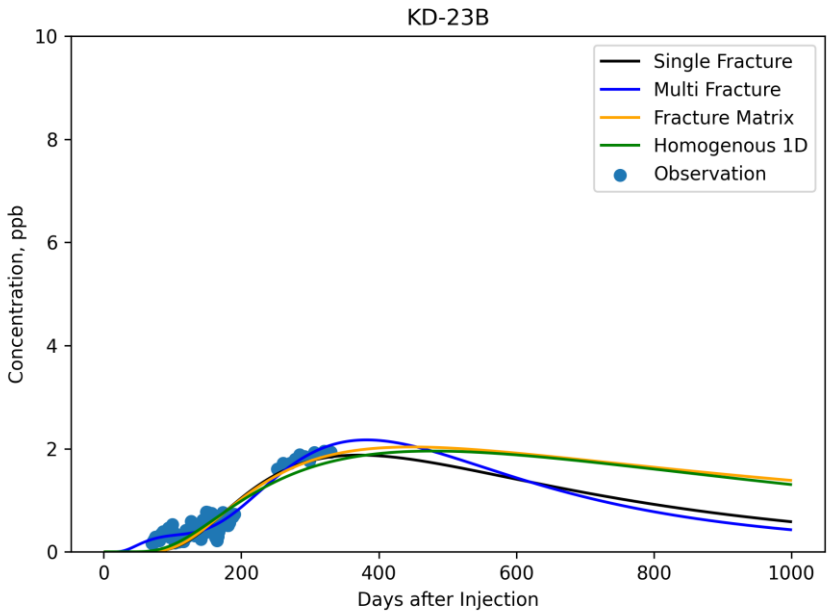

B. 1 Tracer Breakthrough Curves of the Analytical Models for KD-23B

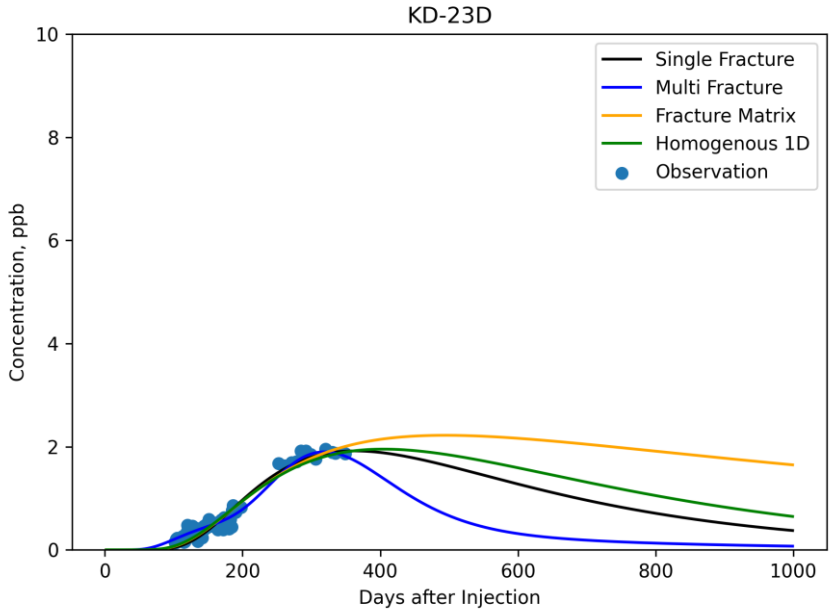

B. 2 Tracer Breakthrough Curves of the Analytical Models for KD-23D

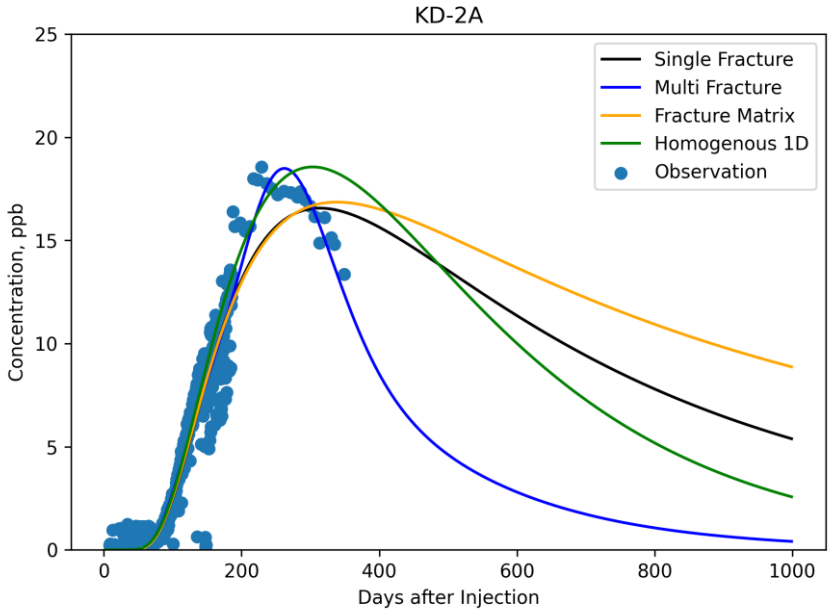

B. 3 Tracer Breakthrough Curves of the Analytical Models for KD-2A

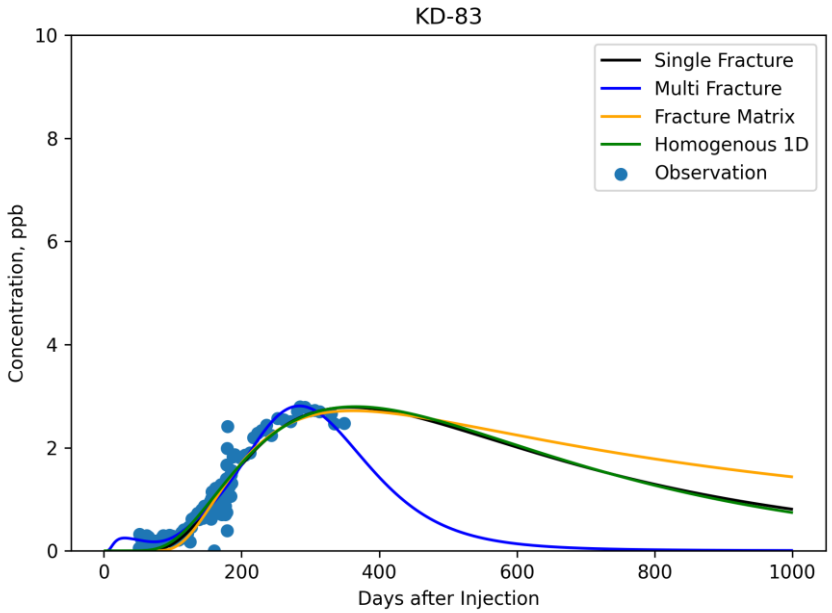

B. 4 Tracer Breakthrough Curves of the Analytical Models for KD-83

Table 8-1 Results of the analytical models for KD-2A.

Model	*Pe*	*L*	t_m	D_{tr}	*u*	*SSE*
Multi Fracture	13.97	139.74	276.75	244.76	3.25	776
Single Fracture	2.80	110.99	794.75	303.12	1.0342	87
	w	*L*	t_b			
Fracture Matrix	0.011	459293	5.39			876
	Pe	t_r	α	D_l	*u*	
1D Uniform	5.23	366.67	157	351.96	2.24	1076

Table 8-2 Results of the analytical models for KD-23B.

Model	*Pe*	*L*	t_m	D_{tr}	*u*	*SSE*
Multi Fracture	9.96	22.17	584.98	542.11	2.79	1.44
Single Fracture	4.42	15.18	699.9	756.99	2.19	5.32
	w	*L*	t_b			
Fracture Matrix	0.01	84368	6.61			5.16
	Pe	t_r	α	D_l	*u*	
1D Uniform	2.92	669.47	523.66	1197.54	2.29	4.59

Table 8-3 Results of the analytical models for KD-23D.

Model	*Pe*	*L*	t_m	D_{tr}	*u*	*SSE*
Multi Fracture	19.49	15.72	470.74	502.64	3.56	0.645
Single Fracture	6.16	16.15	581.14	654.77	2.63	1.936
	w	*L*	t_b			
Fracture Matrix	0.001	109073	0.767			1.642
	Pe	t_r	α	D_l	*u*	
1D Uniform	5.25	488.943	291.34	912.28	3.13	1.659

Table 8-4 Results of the analytical models for KD-83.

Model	*Pe*	*L*	t_m	D_{tr}	*u*	*SSE*
Multi Fracture	12.12	23.45	302.74	368.30	3.56	12.12
Single Fracture	4.374	22.08	680.45	389.66	1.58	9.33
	w	*L*	t_b			
Fracture Matrix	0.079	70799.71	38.71			10.62
	Pe	t_r	α	D_l	*u*	
1D Uniform	5.04	445.13	213.53	516.65	2.42	9.78

C. Appendix C - Results of the Analytical Models for the well KD-50A

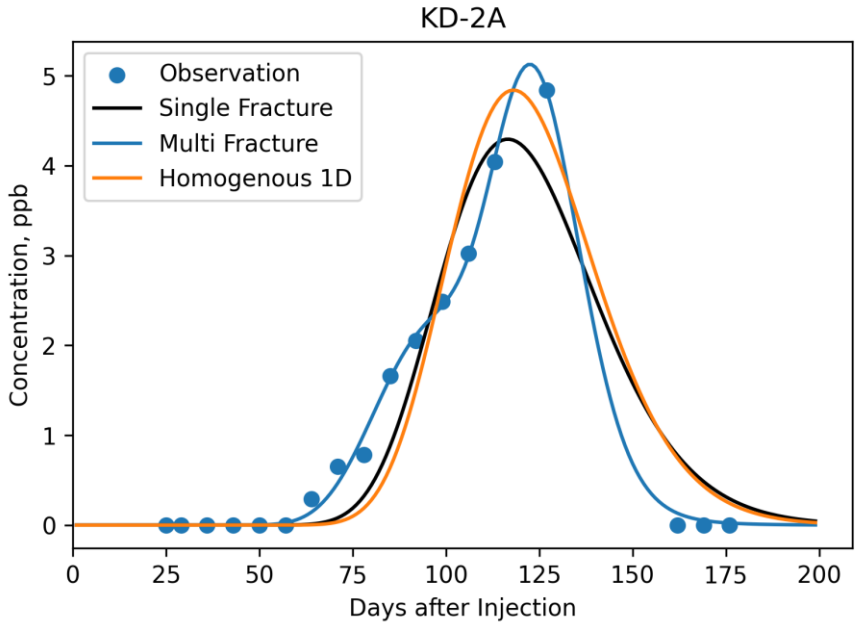

C. 1 Results of the analytical models for KD-2A

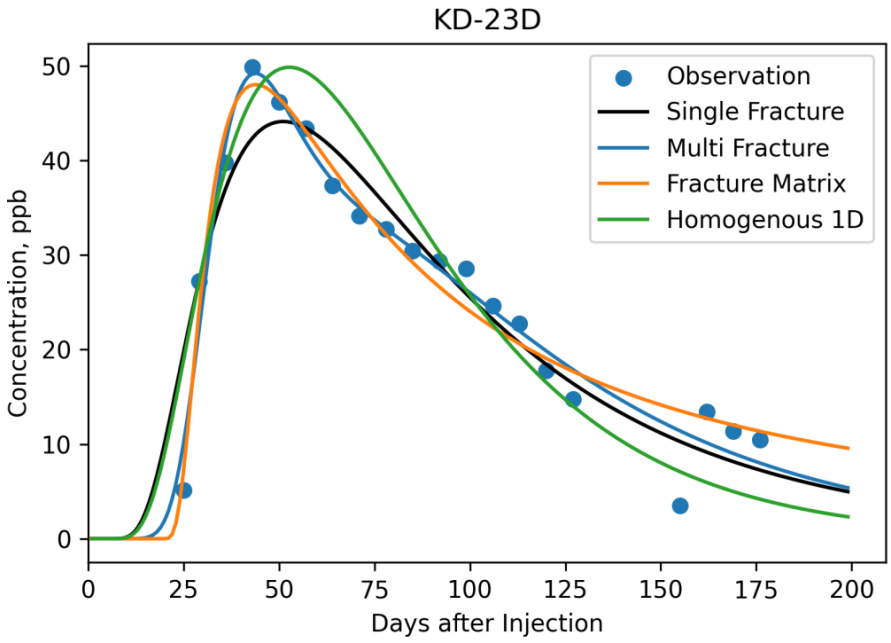

C. 2 Results of the analytical models for KD-23D

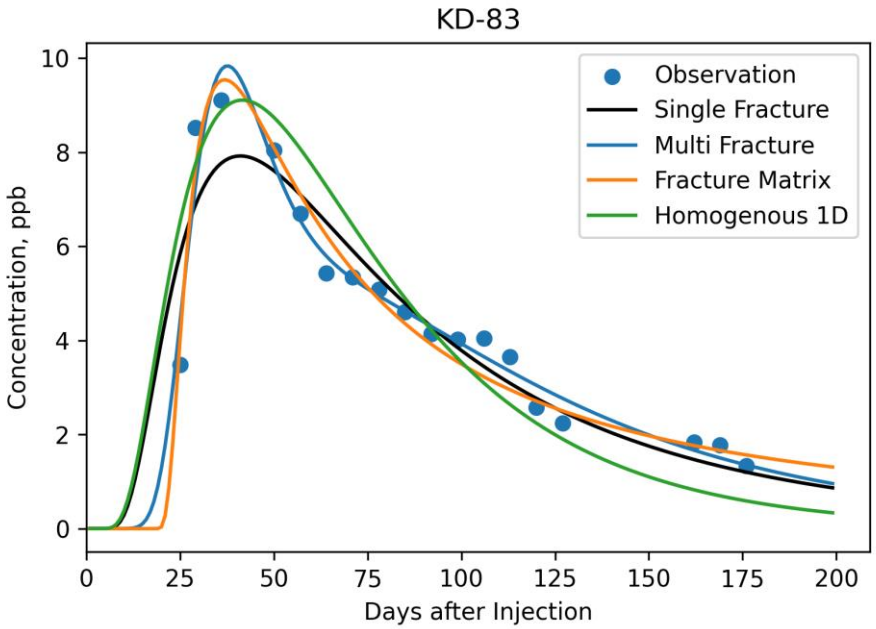

C. 3 Results of the analytical models for KD-83

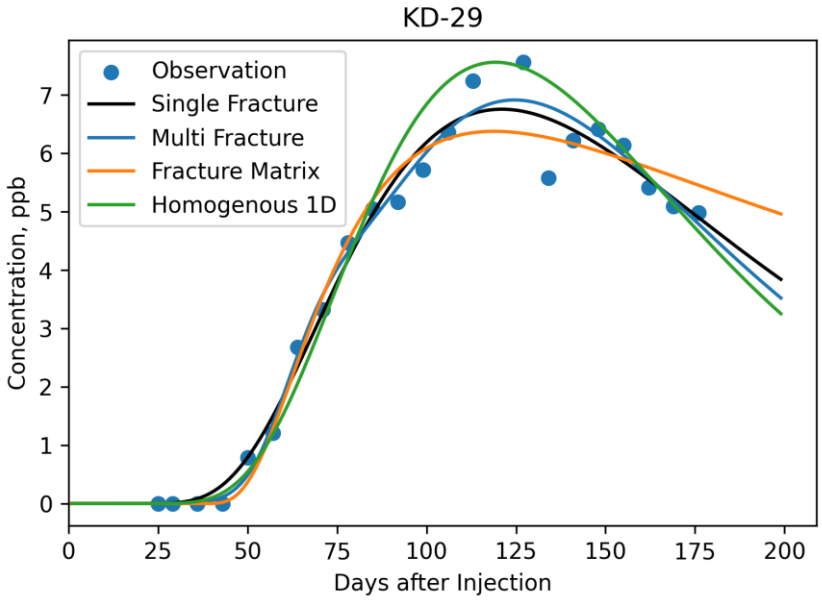

C. 4 Results of the analytical models for KD-29

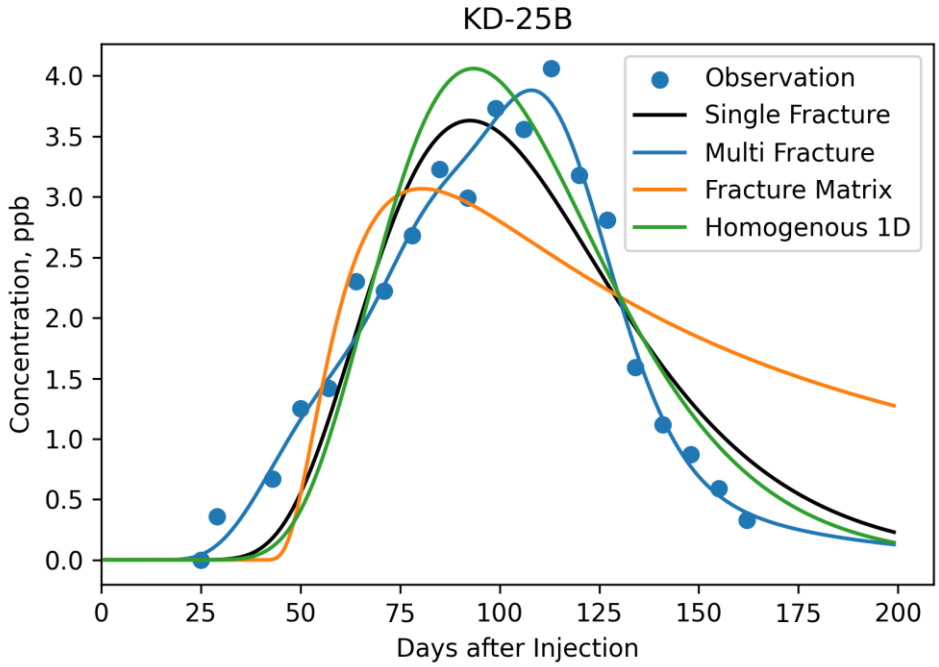

C. 5 Results of the analytical models for KD-25B

Table 8-5 Results of the analytical models for KD-2A.

Model	*Pe*	*L*	t_m	D_{tr}	*u*	*SSE*
Multi Fracture	49.24	33.26	113.00	23.47	4.02	0.14
Single Fracture	62.81	22.91	122.28	26.36	3.68	3.90
	w	*L*	t_b			
Fracture Matrix	1.95	1860.30	75.33			15.28
	Pe	t_r	α	D_l	*u*	
1D Uniform	74.30	119.69	6.06	22.77	3.76	4.37

Table 8-6 Results of the analytical models for KD-23D.

Model	*Pe*	*L*	t_m	D_{tr}	*u*	*SSE*
Multi Fracture	14.26	210.43	85.11	283.52	6.91	167.32
Single Fracture	4.41	132.35	96.48	550.57	5.02	428.18
	w	*L*	t_b			
Fracture Matrix	0.44	29067.08	17.52			185.04
	Pe	t_r	α	D_l	*u*	
1D Uniform	6.35	61.62	76.20	598.51	7.85	652.79

Table 8-7 Results of the analytical models for KD-25B.

Model	*Pe*	*L*	t_m	D_{tr}	*u*	*SSE*
Multi Fracture	44.98	24.87	101.93	103.85	3.88	0.78
Single Fracture	18.46	16.76	108.81	76.90	3.60	4.69
	w	*L*	t_b			
Fracture Matrix	0.57	3918.48	37.19			12.01
	Pe	t_r	α	D_l	*u*	
1D Uniform	22.53	97.68	17.45	70.01	4.01	5.43

Table 8-8 Results of the analytical models for KD-83.

Model	*Pe*	*L*	t_m	D_{tr}	*u*	*SSE*
Multi Fracture	19.72	37.79	56.35	283.22	10.47	4.10
Single Fracture	3.16	19.84	95.61	781.70	5.08	13.24
	w	*L*	t_b			
Fracture Matrix	0.57	3786.62	17.01			3.86
	Pe	t_r	α	D_l	*u*	
1D Uniform	4.78	51.17	101.57	964.80	9.50	22.43

Table 8-9 Results of the analytical models for KD-29.

Model	*Pe*	*L*	t_m	D_{tr}	*u*	*SSE*
Multi Fracture	17.03	41.33	152.24	251.58	4.93	2.84
Single Fracture	8.95	34.15	168.21	342.50	4.27	3.06
	w	*L*	t_b			
Fracture Matrix	0.22	24116.16	29.63			4.30
	Pe	t_r	α	D_l	*u*	
1D Uniform	12.74	129.02	56.37	313.70	5.56	6.77

D. Appendix D – BTCs for the CO_2 Constant Rate Injection Scenarios

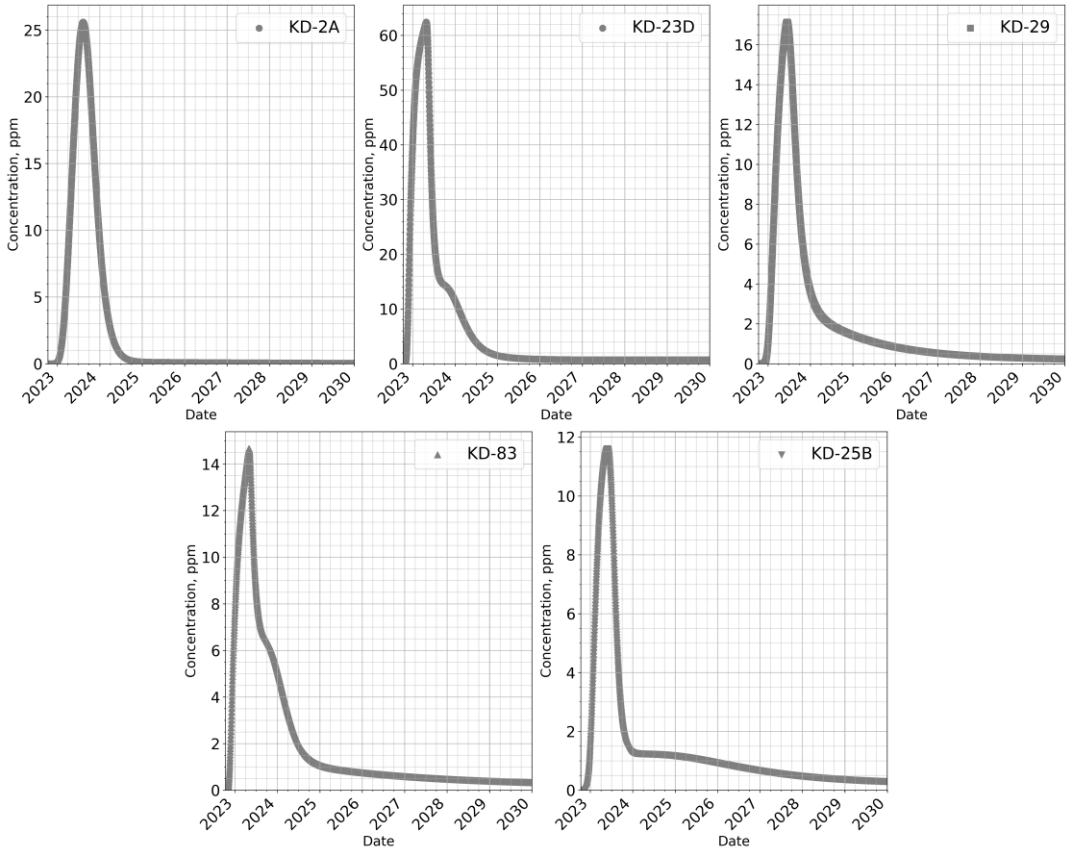

D. 1 CO_2 breakthrough curves for 6 months of 1250 tons/year CO_2-brine injection.

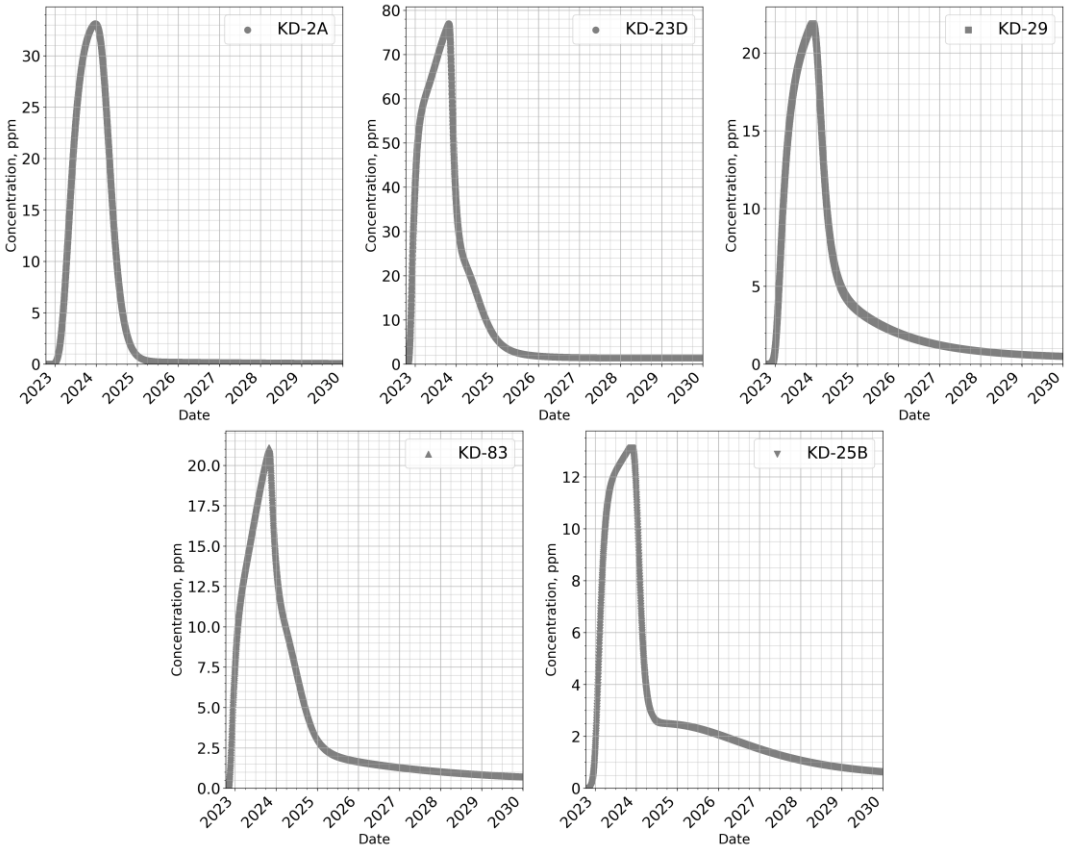

D. 2 CO_2 Breakthrough curves for 12 months of 1250 tons/year CO_2-brine injection

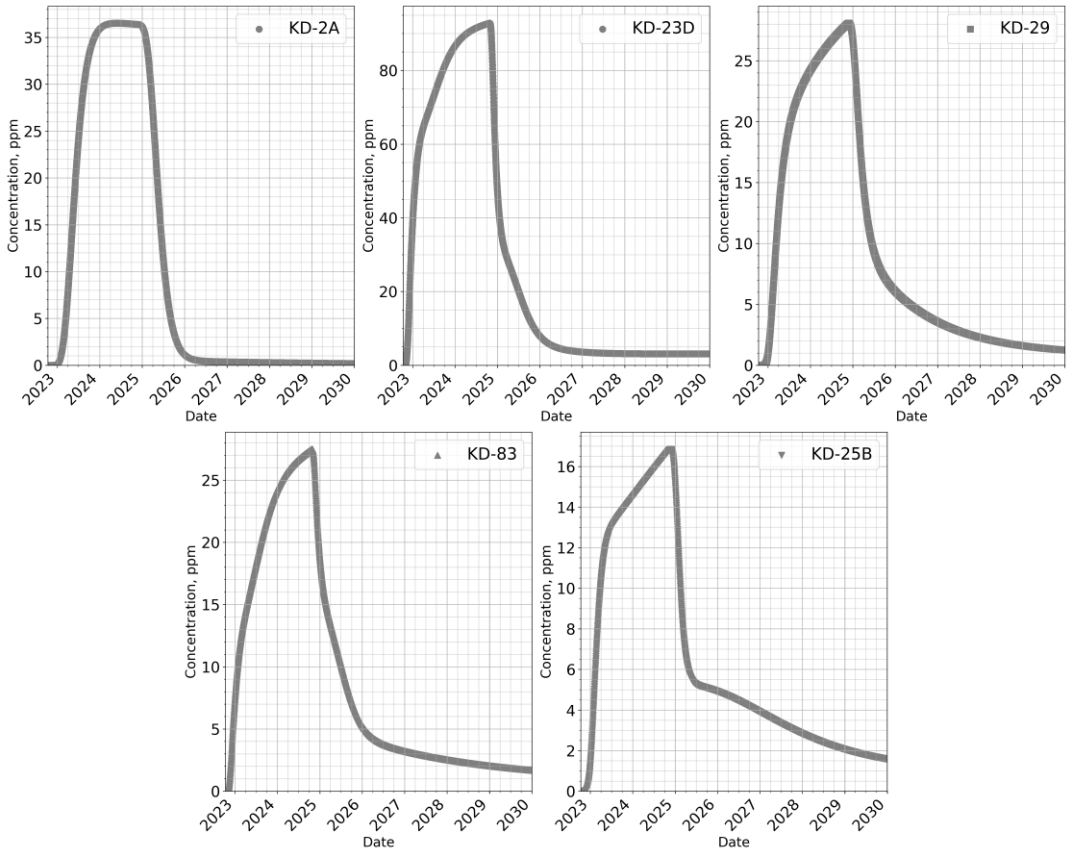

D. 3 CO_2 Breakthrough curves for 24 months of 1250 tons/year CO_2-brine injection

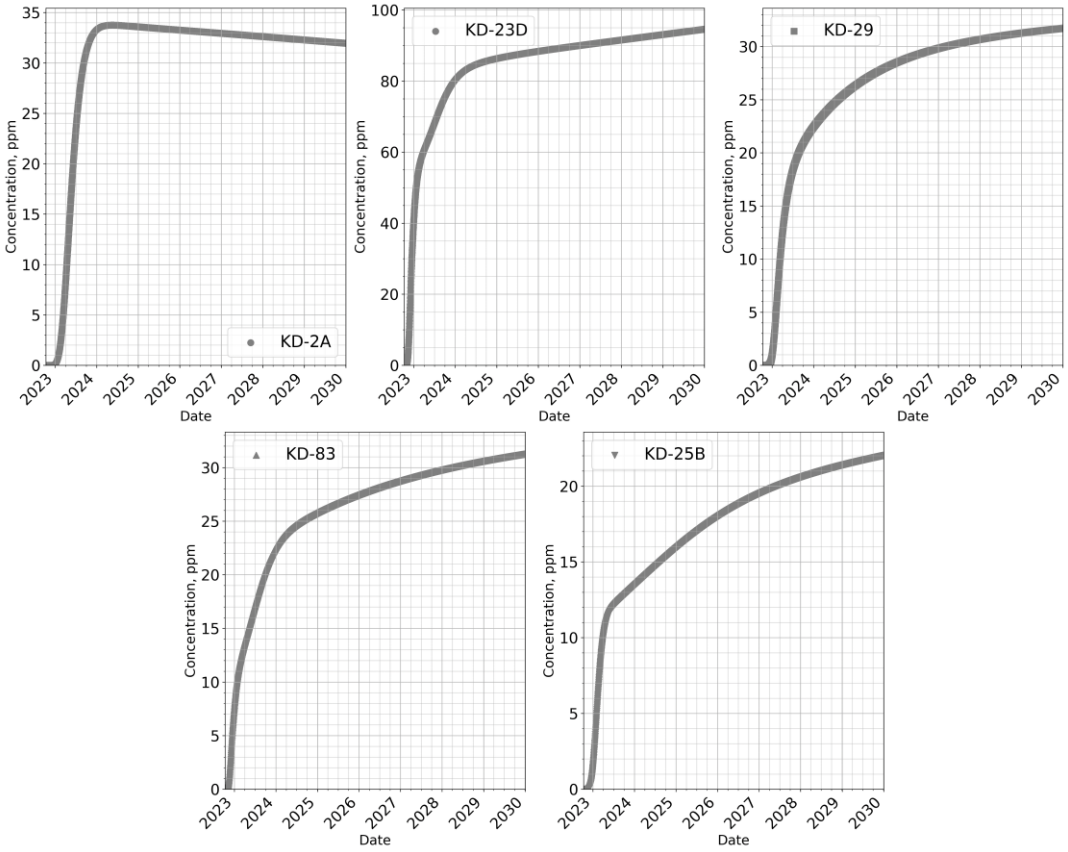

D. 4 CO_2 Breakthrough curves for 8 years of 1250 tons/year CO_2-brine injection

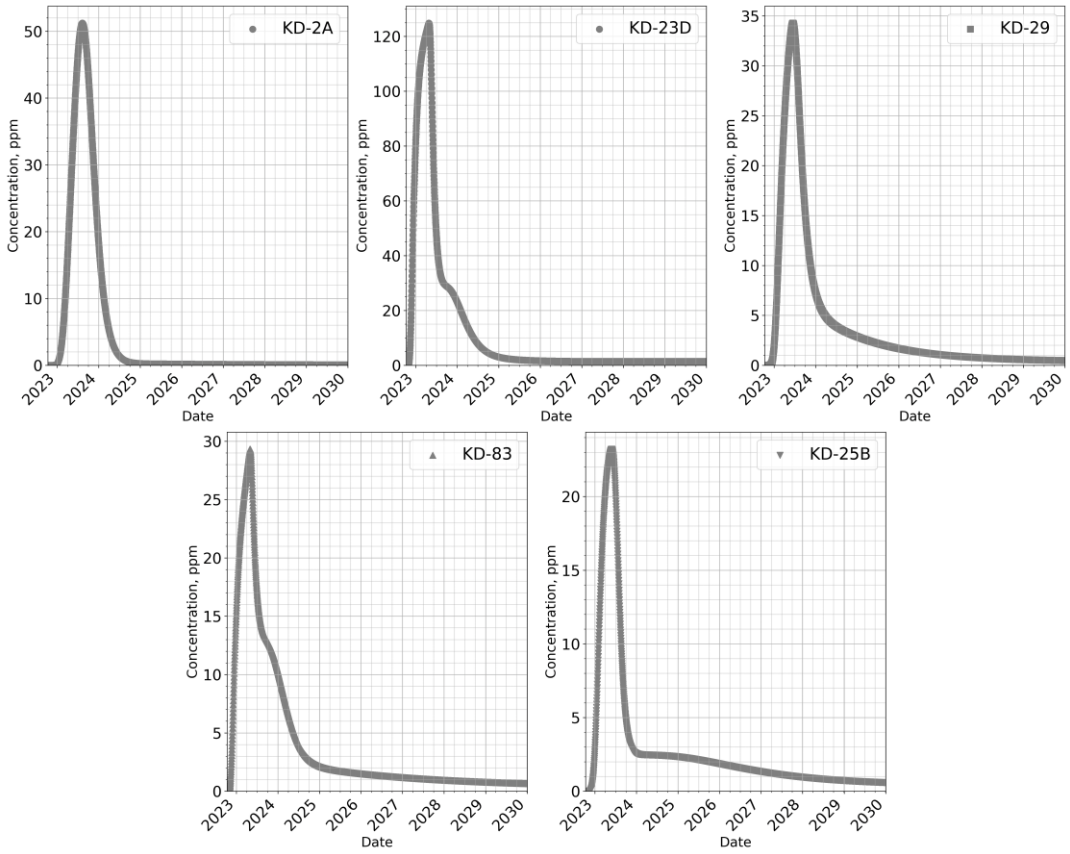

D. 5 CO_2 breakthrough curves for 6 months of 2500 tons/year CO_2-brine injection.

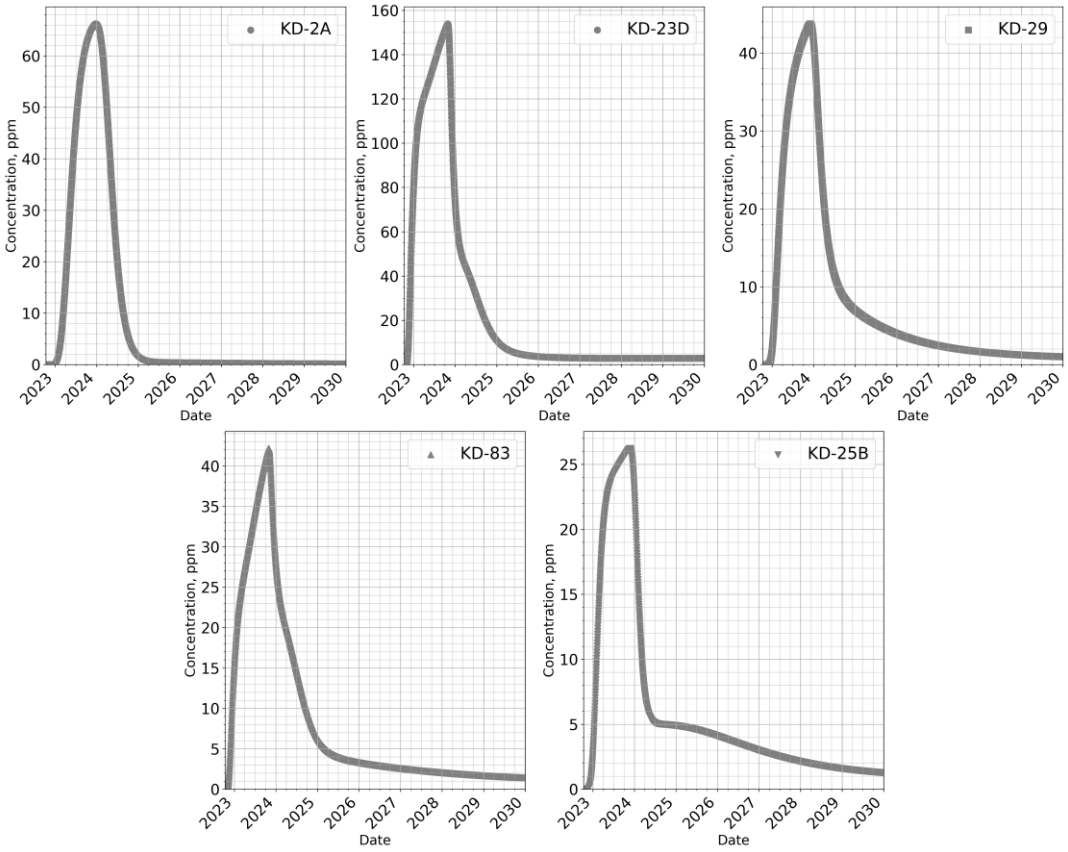

D. 6 CO_2 breakthrough curves for 12 months of 2500 tons/year CO_2-brine injection.

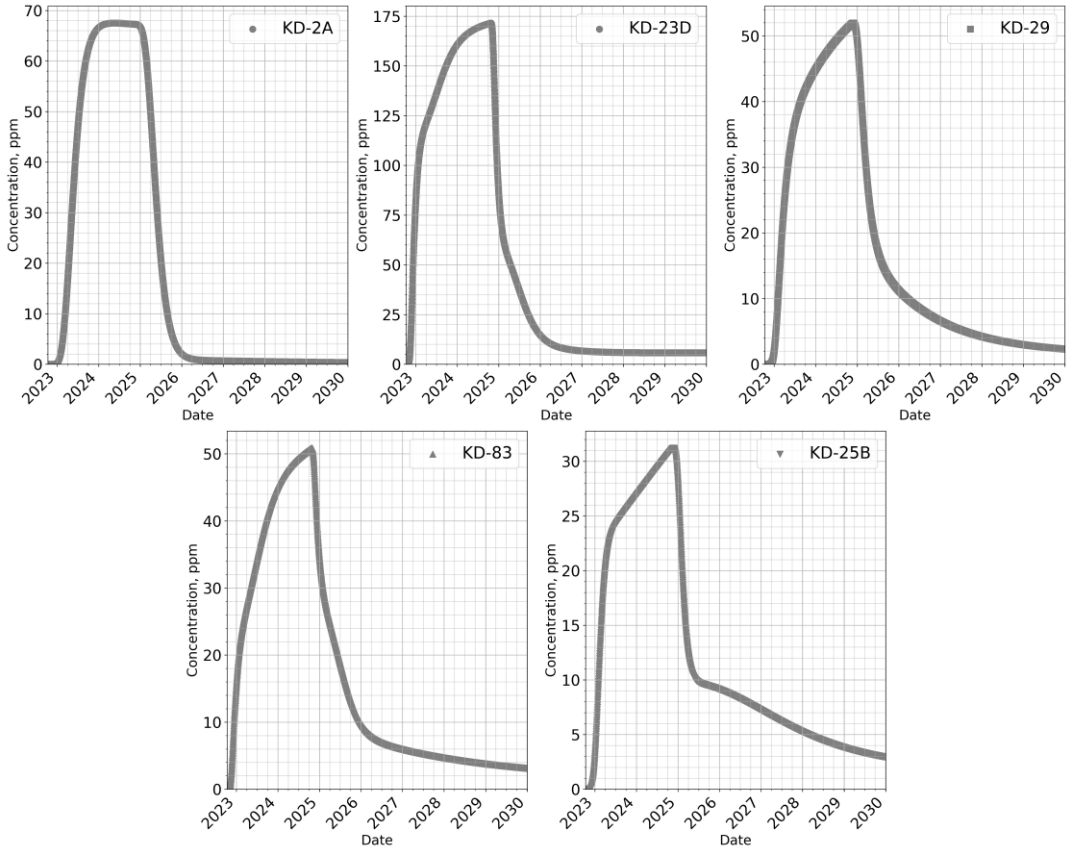

D. 7 CO_2 breakthrough curves for 24 months of 2500 tons/year CO_2-brine injection.

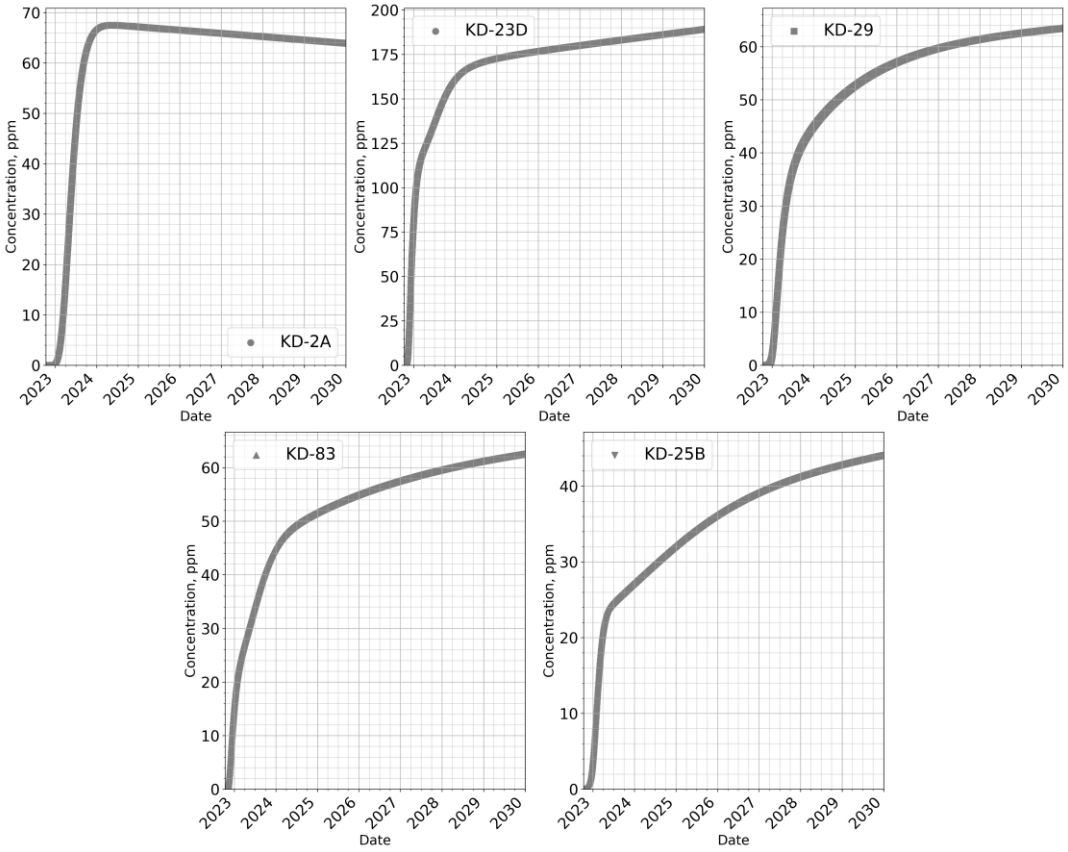

D. 8 CO_2 breakthrough curves for 8 years of 2500 tons/year CO_2-brine injection.

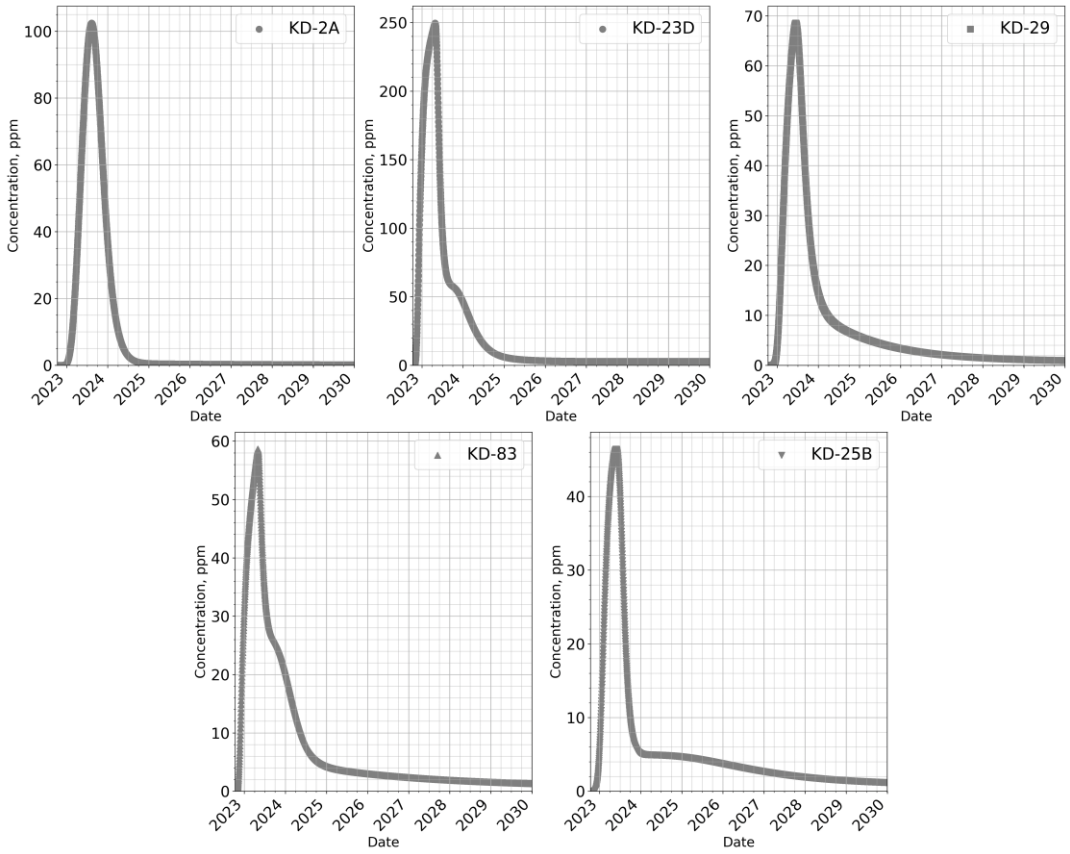

D. 9 CO_2 breakthrough curves for 6 months of 5000 tons/year CO_2-brine injection.

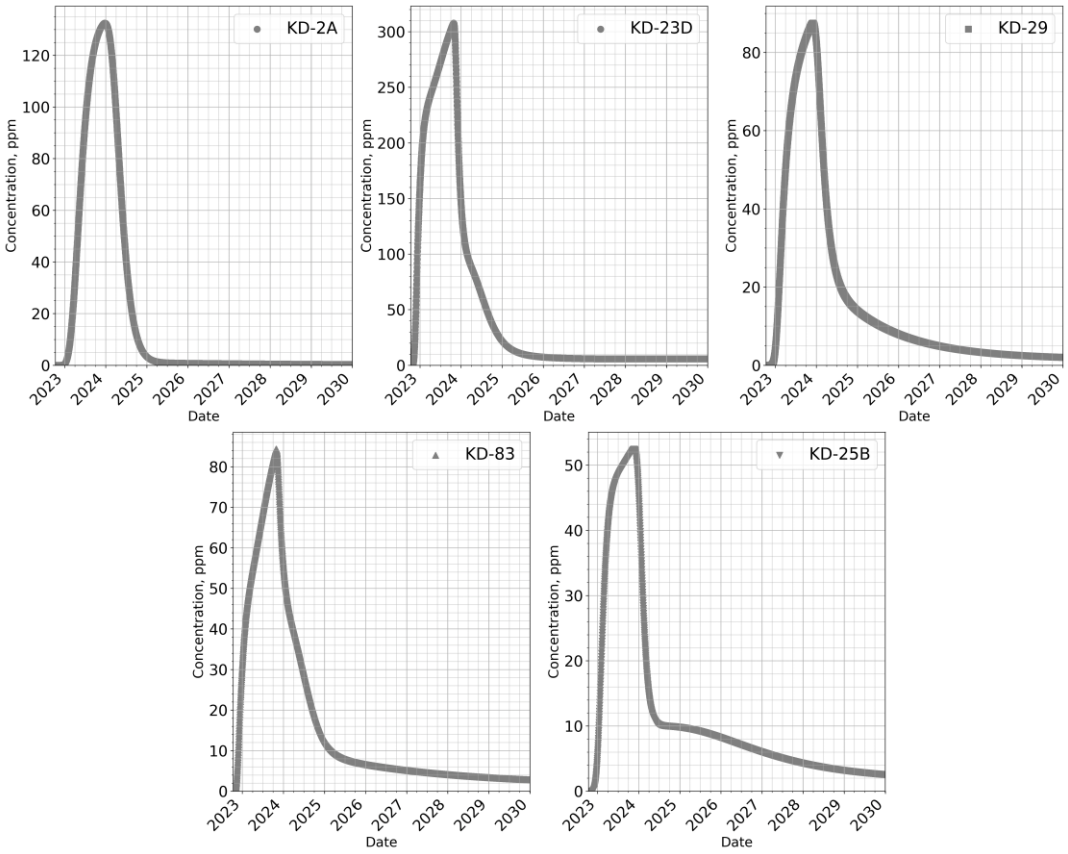

D. 10 CO_2 breakthrough curves for 12 months of 5000 tons/year CO_2-brine injection.

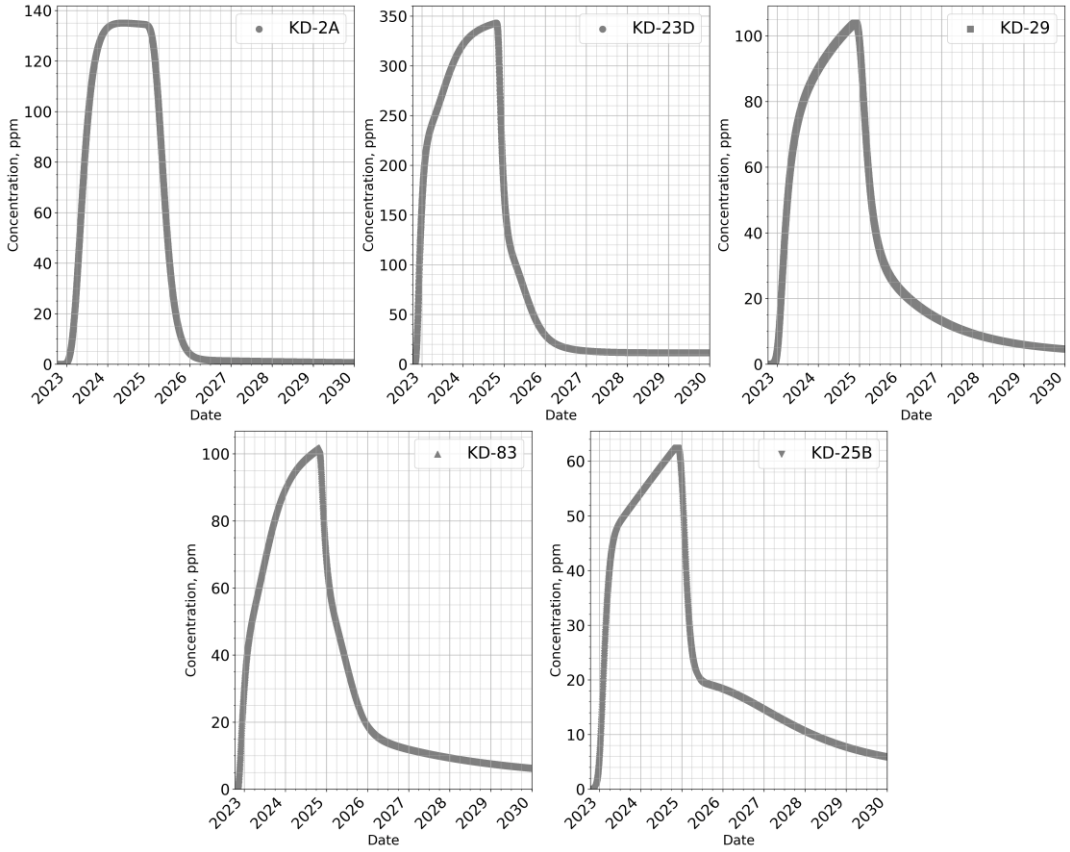

D. 11 CO_2 breakthrough curves for 24 months of 5000 tons/year CO_2-brine injection.

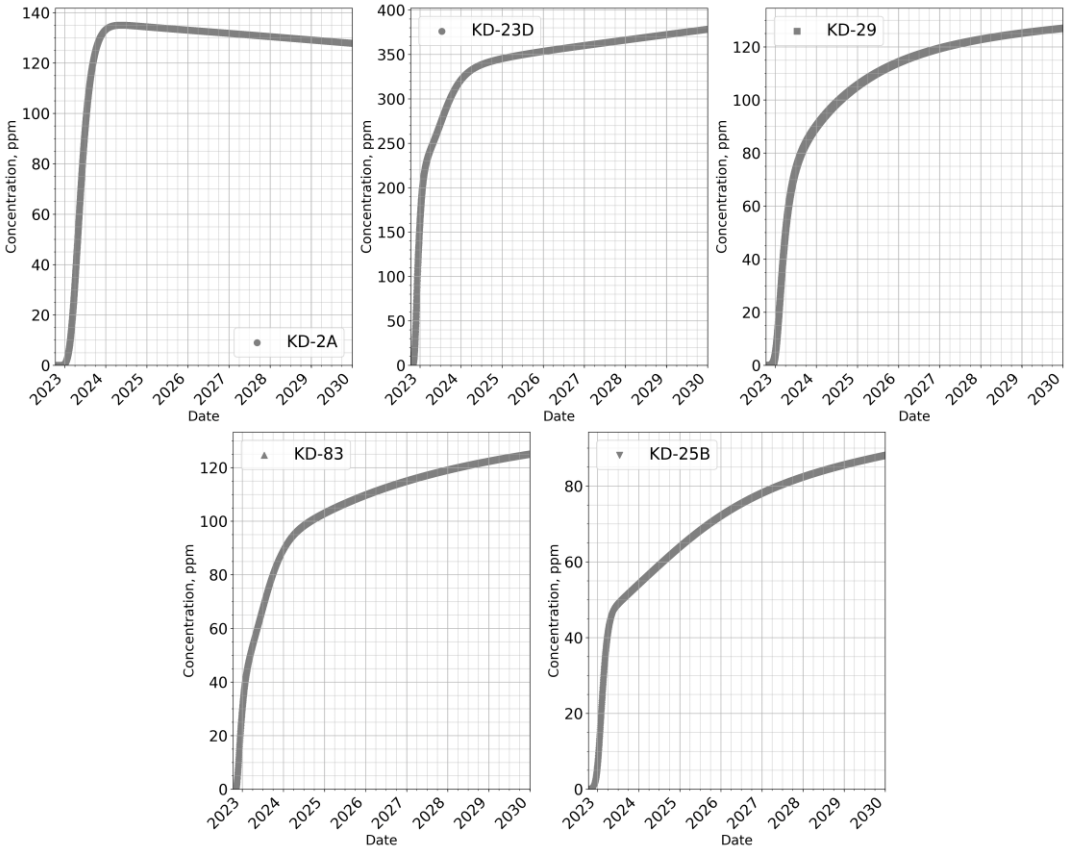

D. 12 CO_2 breakthrough curves for 8 years of 5000 tons/year CO_2-brine injection.

E. Appendix E - BTCs for the CO_2 Constant BHP Injection Scenarios

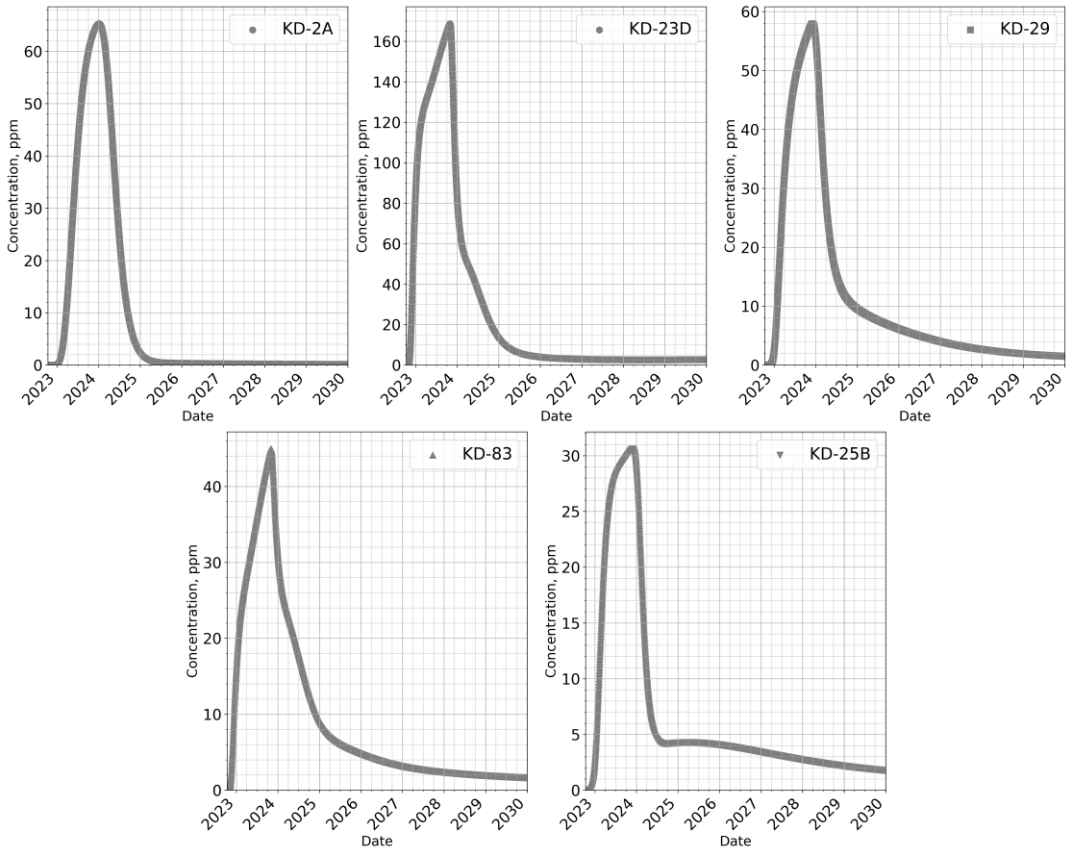

E. 1 CO_2 breakthrough curves for 12 months of 2500 tons/year CO_2-brine injection (+3 bar constant bottom-hole pressure).

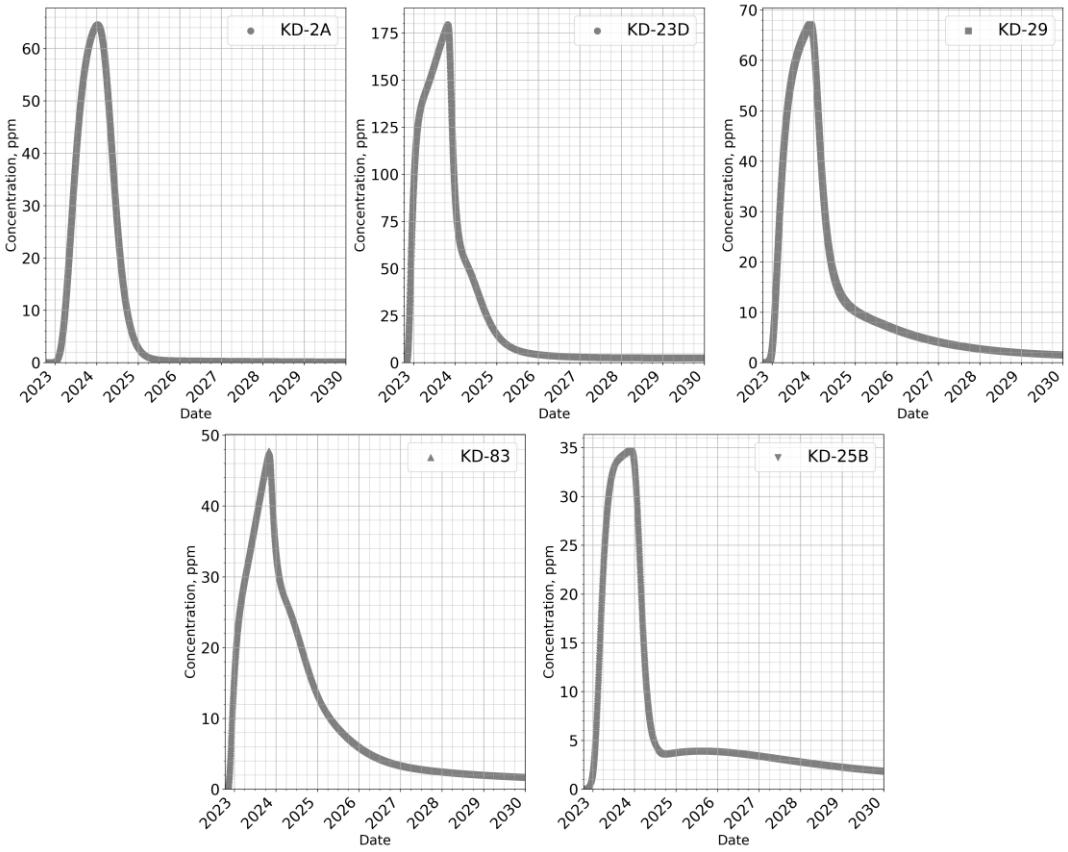

E. 2 CO_2 breakthrough curves for 12 months of 2500 tons/year CO_2-brine injection (+6 bar constant bottom-hole pressure).

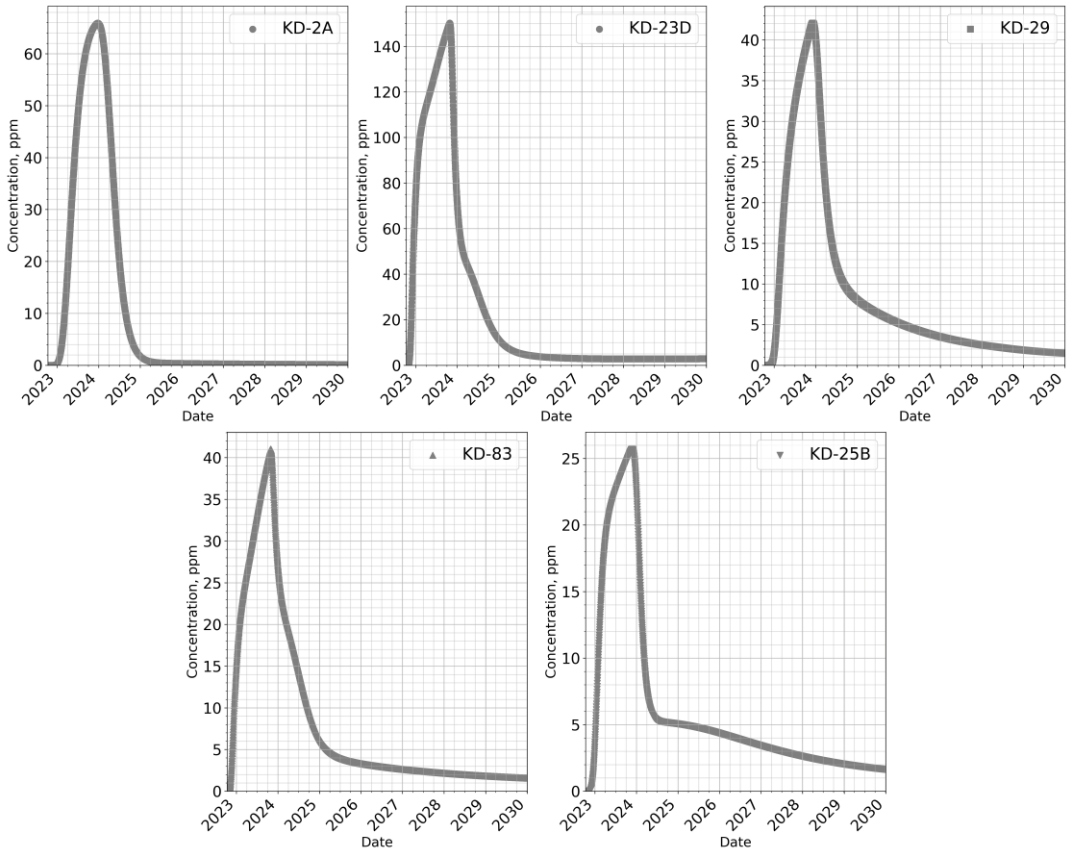

E. 3 CO_2 Breakthrough curves for 12 months of 2500 tons/year CO_2-brine injection (-3 bar constant bottom-hole pressure).

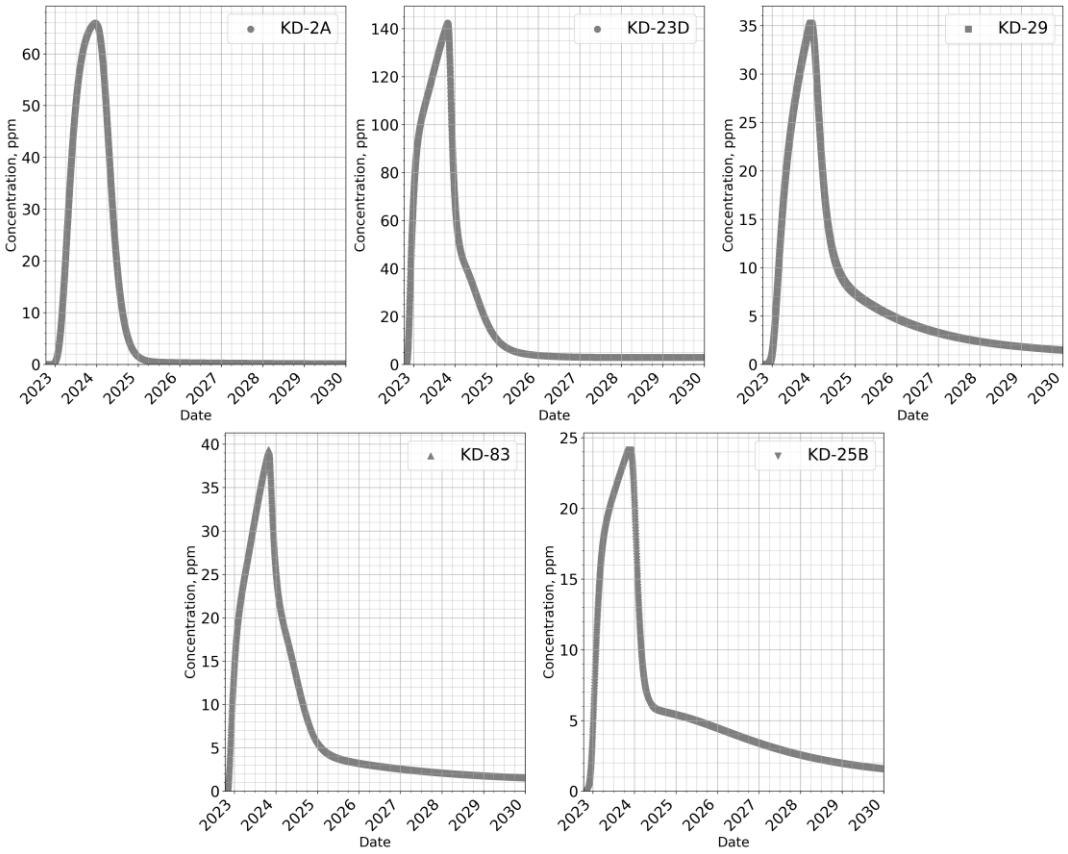

E. 4 CO_2 breakthrough curves for 12 months of 2500 tons/year CO_2-brine injection (-6 bar constant bottom-hole pressure).